

**Neutron density distributions of  $^{204,206,208}\text{Pb}$   
deduced via proton elastic scattering  
at  $E_p = 295 \text{ MeV}$**

ZENIHIRO, Juzo



Doctoral Dissertation

Department of Physics

Faculty of Science

Kyoto University

2011



## Abstract

Cross sections and analyzing powers for polarized proton elastic scattering from  $^{58}\text{Ni}$ , and  $^{204,206,208}\text{Pb}$  have been measured at intermediate energy  $E_p = 295$  MeV. An effective relativistic Love-Franey interaction is tuned to reproduce  $^{58}\text{Ni}$  scattering data within the framework of the relativistic impulse approximation.

The neutron densities of the lead isotopes are deduced using model independent sum-of-Gaussian distributions. Their error-envelopes are estimated by a new  $\chi^2$  criterion including uncertainties associated with the reaction model as well as the experimental uncertainties.

The systematic behaviors of extracted error-envelopes of the neutron density distributions in  $^{204,206,208}\text{Pb}$  are presented. The extracted neutron and proton density distributions of  $^{204,206,208}\text{Pb}$  give neutron skin thicknesses of  $\Delta r_{np} = 0.178^{+0.047}_{-0.059}$  fm,  $0.180^{+0.048}_{-0.064}$  fm, and  $0.211^{+0.054}_{-0.063}$  fm, respectively. Even including the model uncertainties, the errors of the extracted  $\Delta r_{np}$  are at the level of 1 % of the neutron rms radius and still comparable to the previous results which reflect the experimental errors only.

It is found that the neutron skin thicknesses are strongly correlated with the symmetry energy at saturation  $\mathcal{S}(\rho_{\text{sat}})$  and the slope coefficient of the symmetry energy  $L$  according to predictions by various relativistic and non-relativistic mean-field models. By using the linear correlations our results of the neutron skins for  $^{204,206,208}\text{Pb}$  lead to the weighted mean of  $\mathcal{S}(\rho_{\text{sat}}) = 33.0 \pm 1.1$  MeV and  $L = 67.0 \pm 12.1$  MeV. The extracted ranges of  $\mathcal{S}(\rho_{\text{sat}})$  and  $L$  include the experimental uncertainties only, but they are consistent with and smaller than the previous results.



# Contents

<b>1</b>	<b>INTRODUCTION</b>	<b>1</b>
1.1	Equation of state of asymmetric nuclear matter . . . . .	1
1.2	Symmetry energy and neutron skin thickness of $^{208}\text{Pb}$ . . . . .	4
1.3	Nucleon density distributions . . . . .	6
1.3.1	Proton density distributions . . . . .	6
1.3.2	Neutron density distributions . . . . .	6
1.4	Purpose of this work . . . . .	8
<b>2</b>	<b>EXPERIMENTAL PROCEDURE</b>	<b>13</b>
2.1	Beam line . . . . .	13
2.1.1	Polarized proton beam . . . . .	13
2.1.2	Beam line polarimeter . . . . .	15
2.2	Targets . . . . .	16
2.3	Faraday Cups . . . . .	17
2.4	Magnetic spectrometer, “Grand Raiden” . . . . .	17
2.5	Focal plane detectors . . . . .	20
2.6	Trigger system . . . . .	21
2.7	Data acquisition system . . . . .	22
<b>3</b>	<b>DATA REDUCTION &amp; RESULTS</b>	<b>25</b>
3.1	BLP data . . . . .	25
3.1.1	Beam polarization . . . . .	25
3.1.2	Beam intensity . . . . .	28
3.2	Particle identification . . . . .	28
3.3	Multi-wire drift chambers . . . . .	31
3.3.1	Track reconstruction of scattered particles . . . . .	31
3.3.2	Tracking efficiency . . . . .	36
3.4	Differential cross sections and analyzing powers . . . . .	37
<b>4</b>	<b>ANALYSIS</b>	<b>41</b>
4.1	Relativistic impulse approximation . . . . .	41
4.1.1	Realistic point proton density distributions . . . . .	43

---

4.1.2	Scalar and Vector density distributions . . . . .	44
4.2	Medium modification of $NN$ interaction . . . . .	46
4.3	Calibration of the medium effect parameters . . . . .	47
4.4	Extraction of neutron density distributions . . . . .	50
4.4.1	Estimation of error-envelopes . . . . .	52
<b>5</b>	<b>RESULTS AND DISCUSSION</b>	<b>63</b>
5.1	Charge, proton, and neutron rms radii . . . . .	63
5.2	Neutron skin thicknesses . . . . .	64
<b>6</b>	<b>SUMMARY</b>	<b>79</b>
<b>A</b>	<b>Data table</b>	<b>83</b>
<b>B</b>	<b>Relativistic impulse approximation</b>	<b>91</b>
<b>C</b>	<b>Equation of state of nuclear matter</b>	<b>97</b>

# Chapter 1

## INTRODUCTION

Since 1950s, various nuclear ground-state properties such as the masses of nuclei, the shapes and sizes of nuclear matter or nuclear charge distributions, the binding energy per nucleon, and the nuclear incompressibilities, have been measured by a variety of experimental methods in many accelerator facilities in the world. Based on the measurements of such properties, a number of theoretical studies have been also performed over the ages. However even for the stable nuclei it is not easy to understand the enormous aspects of the nuclear many-body system.

For the last few decades, in addition, new phenomena such as skin and halo structures, and the change of the nuclear magic number have been found from the experimental studies of unstable nuclei, whose neutron number  $N$  is very different from its proton number  $Z$ . In the light unstable nuclei, for example,  $^{11}\text{Li}$  was found to have a large neutron halo through the measurements of interaction cross sections [1]. The excess two neutrons in  $^{11}\text{Li}$  are remarkably widespread by the tunneling effect and very weakly bound around  $^9\text{Li}$  core. The radius of  $^{11}\text{Li}$  is comparable to that of  $^{208}\text{Pb}$ . It is now expected that the complementary research for such exotic nuclei as well as for stable nuclei is powerful tool not only to understand these new features of nuclei, but also to establish more precise and comprehensive framework of nuclear many-body system including a large isospin asymmetry. For this purpose, several next-generation facilities in the world, which can provide high-energy and high-intensity radioactive heavy-ion beams, has been constructed or planned in recent years. Above all, the RI Beam Factory (RIBF) at RIKEN in Japan has already started providing heavy-ion beam such as  $^{238}\text{U}$  at 345 MeV/u and some fruitful results of the productions of new rare isotopes has been reported [2].

### 1.1 Equation of state of asymmetric nuclear matter

Among these new phenomena, the role of *isospin asymmetry* in nuclei and nuclear matters have received a lot of attention in both the nuclear physics and astrophysics, and have been investigated using many experimental results and theoretical models. Particularly, the isospin-dependent term of the equation of state (EOS), i.e., the density dependence of the nuclear

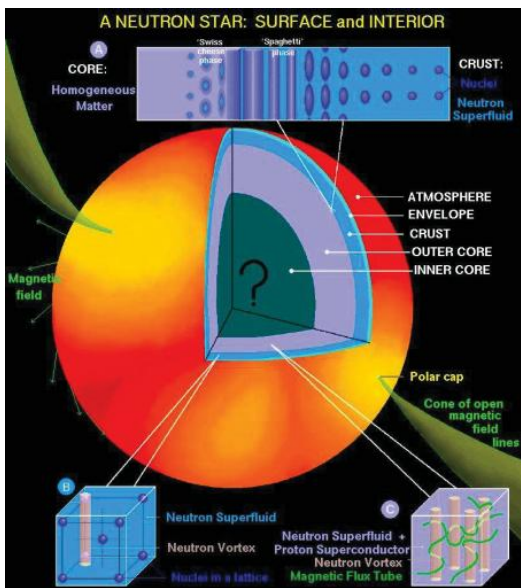


Figure 1.1: Rendition of the assumed structure and phases of a neutron star. Taken from Ref. [33].

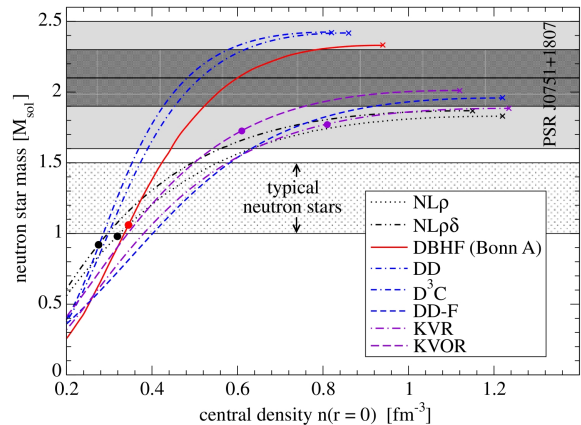


Figure 1.2: Neutron star mass versus central density obtained from various types of the EOSs by relativistic hadronic field models, taken from Ref. [34]

symmetry energy is now considered as one of the most important question to be solved.

There have been quite a lot of microscopic and phenomenological, non-relativistic and relativistic approaches to understand the equation of state of asymmetric nuclei and nuclear matters, such as the Brueckner-Hartree-Fock [3, 4] and the Dirac-Brueckner-Hartree-Fock [5–8] approach with bare  $NN$  interaction, and the non-relativistic mean-field model based on the Skyrme interactions [9–15] and the relativistic mean-field model [16–27]. In addition, the EOS of the asymmetric nuclear matter is essential to the understanding of astrophysical phenomena such as supernova explosions, neutron stars structure and cooling system, and x-ray bursts [28–32]. Figure 1.1 shows the assumed structure and phases of a neutron star. The composition of a neutron star depends on the EOS of the neutron matter as shown in Fig. 1.2. Figure 1.3 shows the typical calculations of the EOS of the symmetric nuclear and pure neutron matter by microscopic many-body theories and phenomenological approaches.

For asymmetric nuclear matter, the equation of state, i.e., the energy per nucleon can be generally approximated as

$$\mathcal{E}(\rho, \delta) = \mathcal{E}(\rho, 0) + S(\rho)\delta^2 + \mathcal{O}(\delta^4), \quad (1.1)$$

in terms of baryon density  $\rho = \rho_n + \rho_p$ , local isospin asymmetry  $\delta = (\rho_n - \rho_p)/\rho$ , energy per nucleon in symmetric nuclear matter  $\mathcal{E}(\rho, \delta = 0)$ , and so-called nuclear symmetry energy  $S(\rho)$ . This equation (1.1) is known as the empirical parabolic law for the EOS of asymmetric nuclear matter. The odd-order terms of  $\delta$  is vanishing due to the exchange symmetry between protons and neutrons. Although it has been reported that the higher order terms  $\mathcal{O}(\delta^4)$  become important for determining the transition density and pressure at the inner edge separating the

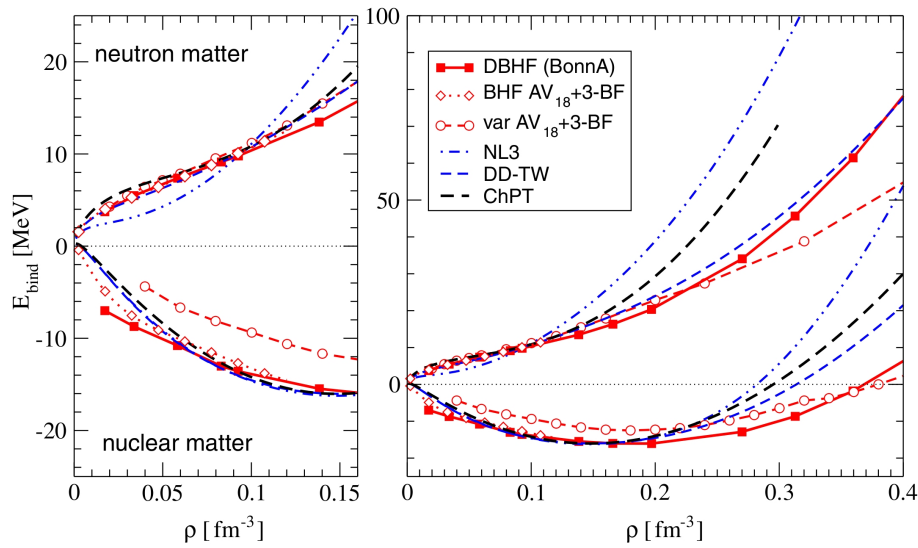


Figure 1.3: The EOS of symmetric nuclear matter and pure neutron matter calculated by the non-relativistic Brueckner-Hartree-Fock and variational approaches using AV18 interaction with three body force (dotted red), the Dirac-Brueckner-Hartree-Fock using Bonn A (solid red), chiral perturbation theory (dashed black), and several phenomenological mean field models (blue) taken from Ref. [34].

liquid core form the solid crust of neutron stars [32], the higher order terms are generally negligible around normal density [35]. Therefore, the density-dependent symmetry energy  $\mathcal{S}(\rho)$  can be obtained from  $\mathcal{S}(\rho) \approx \mathcal{E}(\rho, 1) - \mathcal{E}(\rho, 0)$ . This means the energy difference between the EOS of the neutron matter and the symmetric nuclear matter.

The EOS of the symmetric nuclear matter  $\mathcal{E}_0(\rho) = \mathcal{E}(\rho, 0)$  around the saturation density  $\rho_{\text{sat}}$  can be expanded as

$$\mathcal{E}_0(\rho) = \mathcal{E}_0 + \frac{K_0}{2}\epsilon^2 + \mathcal{O}(\epsilon^3), \quad (1.2)$$

$$K_0 = 9\rho_{\text{sat}}^2 \left. \frac{d^2\mathcal{E}_0(\rho)}{d\rho^2} \right|_{\rho=\rho_{\text{sat}}}, \quad (1.3)$$

where  $\epsilon = (\rho - \rho_{\text{sat}})/3\rho_{\text{sat}}$ . The coefficient  $K_0$  is the so-called incompressibility of symmetric nuclear matter. The binding energy per nucleon  $\mathcal{E}_0$  and the incompressibility  $K_0$  which characterize the symmetric nuclear matter are now known to be about  $-16$  MeV and  $230$  MeV, respectively. The incompressibility, in particular, has been recently constrained by many measurements of giant resonances for various nuclei via  $\alpha$ -inelastic scattering at  $0$  degree [36–40].

## 1.2 Symmetry energy and neutron skin thickness of $^{208}\text{Pb}$

On the other hand, the symmetry energy  $\mathcal{S}(\rho)$  was previously studied by the systematic measurements of the masses of stable nuclei, small  $\delta$  and  $\rho$  around the saturation, based on the earlier empirical mass formula [41–43]. Thus it was difficult to verify the isospin-asymmetry dependence of  $\mathcal{S}(\rho)$ . The importance of the symmetry energy of asymmetric nuclear matter has been recognized by the study of the exotic nuclei with a large neutron excess at the radioactive ion beam facilities. However the isospin dependence of the symmetry energy  $\mathcal{S}(\rho)$  is still less certain and the predictions vary widely among many theoretical models [12, 44, 45].

The nuclear symmetry energy  $\mathcal{S}(\rho)$  which characterizes the asymmetric nuclei and nuclear matter is also expanded around the saturation density as follows:

$$\mathcal{S}(\rho) = \mathcal{S}(\rho_{\text{sat}}) + L\epsilon + \frac{K_{\text{sym}}}{2}\epsilon^2 + \mathcal{O}(\epsilon^3), \quad (1.4)$$

$$L = 3\rho_{\text{sat}} \left. \frac{d\mathcal{S}(\rho)}{d\rho} \right|_{\rho=\rho_{\text{sat}}}, \quad (1.5)$$

$$K_{\text{sym}} = 9\rho_{\text{sat}}^2 \left. \frac{d^2\mathcal{S}(\rho)}{d\rho^2} \right|_{\rho=\rho_{\text{sat}}}, \quad (1.6)$$

where  $L$  and  $K_{\text{sym}}$  are the slope and curvature coefficient of the symmetry energy at the saturation, respectively. From Eq. (1.1), (1.2), and (1.4), the saturation properties of the asymmetric nuclear matter such as the saturation density  $\rho_{\text{sat}}(\delta)$ , energy per nucleon  $E_0(\delta)$ , and the incompressibility  $K_0(\delta)$  as a function of the isospin asymmetry  $\delta$ , are also derived. The details of the evolution of the saturation point are described in Appendix C.

In order to describe not only the symmetric but also asymmetric nuclei or nuclear matter, the non-relativistic mean-field models based of the Skyrme interactions and the relativistic mean-field models including various types of medium density-dependence have been developed together with the experimental results of the ground-state properties of finite nuclei over the ages. It has been shown that the thickness of the neutron skin ( $\Delta r_{np}$ ), defined as the difference between the neutron ( $r_n$ ) and proton ( $r_p$ ) root-mean-square (rms) radii of a nucleus ( $\Delta r_{np} \equiv r_n - r_p$ ), is determined by the balance among the various nuclear matter properties. Indeed, the neutron skin thickness of  $^{208}\text{Pb}$  is strongly correlated with the nuclear symmetry energy coefficients  $\mathcal{S}(\rho_{\text{sat}})$ ,  $L$ , and  $K_{\text{sym}}$  of the equation of state in asymmetric nuclear matter [25, 26, 44–50]. Figures 1.4–1.6 show that the strong correlations between neutron skin thickness for  $^{208}\text{Pb}$  and some symmetry energy parameters such as  $\mathcal{S}(\rho_{\text{sat}})$ ,  $L$ , and  $K_{\text{sym}}$  exist by both the non-relativistic and relativistic mean field models.

$^{208}\text{Pb}$  is the heaviest stable nucleus who has doubly-closed shell structure ( $Z = 82$  and  $N = 126$ ) having major shell gaps, and hence its nuclear properties such as the binding energy, charge radius, have been precisely determined.

Therefore the precise extraction of the neutron skin thickness of  $^{208}\text{Pb}$  is related to constrain the isospin dependence of the effective nuclear interactions and EOS of the isospin asymmetric nuclear matter, particularly, the density dependence of the nuclear symmetry energy. Furthermore, it has been suggested that a precise measurement of the skin thickness of

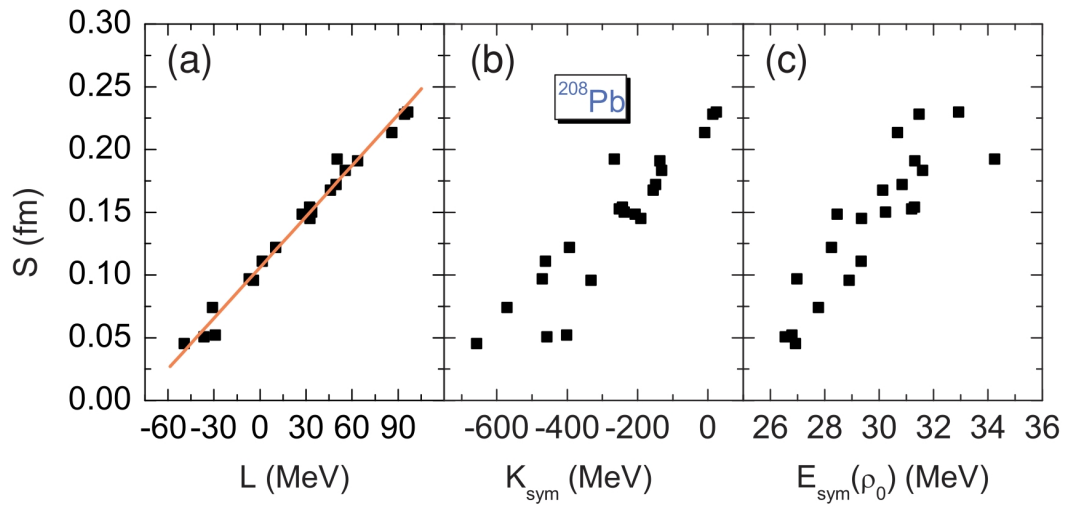


Figure 1.4: Neutron skin thickness for  $^{208}\text{Pb}$  as a function of (a)  $L$ , (b)  $K_{\text{sym}}$ , and (c)  $E_{\text{sym}}(\rho_0) = S(\rho_{\text{sat}})$  for 21 sets of Skyrme parameterizations. Taken from Ref. [51].

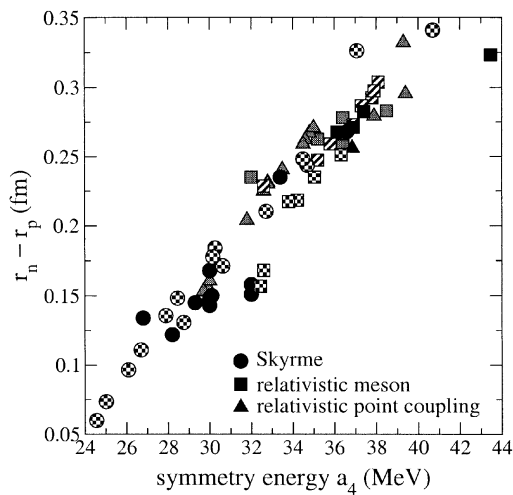


Figure 1.5: Correlation between neutron skin for  $^{208}\text{Pb}$  and the symmetry energy  $a_4 = S(\rho_{\text{sat}})$  at saturation. Take from Ref. [45].

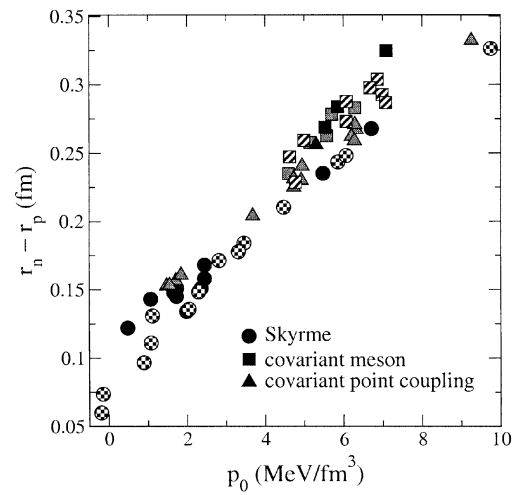


Figure 1.6: Correlation between neutron skin for  $^{208}\text{Pb}$  and the slope of the symmetry energy  $p_0 = \rho_{\text{sat}}L/3$ . Take from Ref. [45].

$^{208}\text{Pb}$  is very important for studying the radius, composition, and cooling system of neutron stars [23, 24, 26, 30–32, 52, 53].

## 1.3 Nucleon density distributions

The nucleon density distribution is one of the most fundamental properties of nuclei. The precise extraction of the nucleon density distributions ( $\rho_p, \rho_n$ ) and hence the neutron skin thickness  $\Delta r_{np}$  is now known to be indispensable for studying the EOS of the asymmetric nuclear matter as mentioned in the previous section.

However, compared to other ground-state properties of finite nuclei such as charge densities, charge radii, and binding energies, it is difficult to measure the size and shape of the neutron densities precisely due to the large ambiguity of the hadronic process.

### 1.3.1 Proton density distributions

In the case of stable nuclei, the proton density  $\rho_p$  and radius  $r_p$  can be derived from the nuclear charge density  $\rho_{ch}$  and the intrinsic nucleon charge density. Nuclear charge distributions for a variety of stable nuclei are now known accurately from a lot of experiments [54–56]. For example, the charge radius of  $^{208}\text{Pb}$  is 5.5010(9) fm with an accuracy of 0.02 % according to a combined analysis of electron scattering, muonic atom X-rays, and isotope shift as shown in Ref. [56]. An electromagnetic probe, due to its simple reaction mechanism, can extract precise information about charge density deep inside a nucleus.

### 1.3.2 Neutron density distributions

Neutron density and radius have been studied by many researchers using proton,  $\alpha$ , pion scattering, and antiprotonic atoms [57–68]. However, typical experimental uncertainties of extracted neutron rms radius are more than ten times as large as those of the charge radius. Hadronic probes exhibit uncertainties in the reaction mechanism which is mainly caused by an incomplete knowledge of the nucleon–nucleon ( $NN$ ) scattering amplitude inside the nuclear medium. In order to extract precise information about the neutron density distribution an appropriate probe and an effective  $NN$  interaction must be carefully chosen.

**“Proton elastic scattering”** Proton–nucleus elastic scattering at intermediate energies ( $E_p \sim 300$  MeV) is a relatively good probe for extracting information about both the nuclear surface and interior. The energy of the incident protons is low enough to suppress meson production and hence allow a shallow absorptive potential to be obtained. It is also high enough to be described by an impulse approximation. As mentioned above, however, uncertainties in the  $NN$  interaction in the nucleus are a problem.

In our previous papers [69, 70], we reduced the uncertainties in the  $NN$  interaction inside the nuclear medium by introducing a phenomenological medium modification in the relativistic Love–Franey interaction in terms of the density dependent parameters. This correction is effectively described as a modification of the masses and coupling constants of the exchanged mesons according to the nucleon density. To calibrate these “medium effect” parameters, we use proton elastic scattering from  $^{58}\text{Ni}$ , because the proton and neutron densities are suppressed

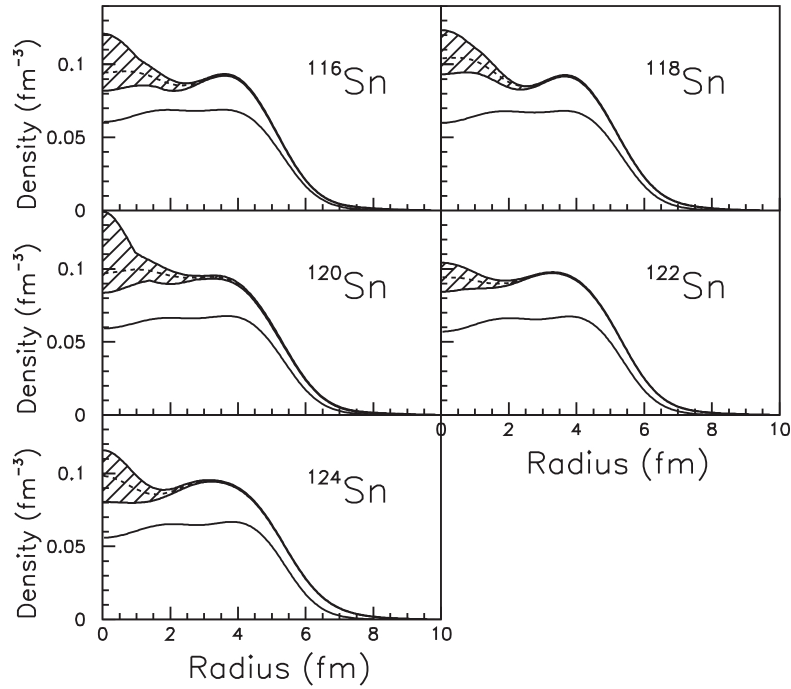


Figure 1.7: Neutron density distributions of  $^{116,118,120,122,124}\text{Sn}$  in the model-independent form of SOG function extracted from polarized proton elastic scattering at  $E_p = 295$  MeV [70].

to have almost the same shape and radius in  $^{58}\text{Ni}$  [8, 13, 58, 66]. Then, using the medium-effect parameters calibrated for  $^{58}\text{Ni}$ , we have extracted the neutron density distributions of tin isotopes in the form of model-independent Sum-of-Gaussians (SOG) distributions. The accuracy of the neutron radii of tin isotopes were found to be less than 0.03 fm including both the statistical and model uncertainties [70] as shown in Fig. 1.7.

After the success of our analysis method for Ni and Sn isotopes, we have performed several experiments to measure proton elastic scattering from heavier or lighter stable nuclei such as  $^{204,206,208}\text{Pb}$ ,  $^{40,42,44,48}\text{Ca}$ ,  $^{36}\text{Ar}$ ,  $^{32}\text{S}$ ,  $^{24}\text{Mg}$ ,  $^{20}\text{Ne}$ , and  $^{16,18}\text{O}$ . Now we have examined the applicability of our analysis method to these isotopes. In addition, since our recent analysis has showed that the absolute values of the cross sections are very important to determine the model-independent density distributions, a separate experiment has been performed to know absolute efficiencies of some detectors [71]. Several improvements to reduce the experimental uncertainties have been also considered in recent analyses.

Above all, we have focused on the neutron density distributions of lead isotopes since the neutron skin of  $^{208}\text{Pb}$ , which is strongly correlated with the EOS parameters as mentioned above, is expected to constrain the EOS of asymmetric nuclear matter. In this thesis, thus, we report the most recent results from the analysis of the proton elastic scattering data of lead isotopes.

## 1.4 Purpose of this work

**Pb isotopes** The purpose of this work is to evaluate the sensitivity of proton elastic scattering to the neutron densities in heavy nuclei such as lead isotopes  $^{204,206,208}\text{Pb}$  with a new  $\chi^2$  method including the ambiguity associated with the interaction model used in the present analysis. It is important for the understanding of isospin asymmetry to study the systematic behavior of the extracted neutron densities. We also focus on the extracted neutron skin thicknesses of  $^{204,206,208}\text{Pb}$  to constrain on the EOS parameters such as  $\mathcal{S}(\rho_{\text{sat}})$  and  $L$ .

Furthermore, if our analysis method to describe the scattering observables and to extract the precise information of the density distributions works successfully even for lead isotopes with large isospin asymmetries, we could apply this approach to unstable nuclei on the basis of this work. Indeed, we have already proposed and performed the so-called ESPRI project (**E**lastic **S**cattering of **P**rotons with **RI** beams) at NIRS-HIMAC in Chiba, Japan, GSI in Germany, and RIBF in RIKEN, Japan. This project aims to measure the cross sections of proton elastic scattering from unstable nuclei by missing mass spectroscopy. Protons, which are inverse-kinematically scattered from solid hydrogen target by heavy ion beam of unstable nuclei at  $E_p = 300 \text{ MeV}/A$ , are detected up to the momentum transfer of  $2.5 \text{ fm}^{-1}$  with recoil particle spectrometer (RPS) which consists of plastic scintillators, multi-wire-drift chambers, and NaI(Tl) calorimeter arrays. We have already performed developments and experiments for several unstable nuclei such as  $^{9,10,11}\text{C}$ ,  $^{20}\text{O}$ , and  $^{66,70}\text{Ni}$ , and achieved 1-mm-thick solid hydrogen target and the excitation energy resolution of  $\sigma \sim 500 \text{ keV}$ . An approved experiment is planned to be performed at RIBF in FY2011.

**Previous or planned experiments for  $^{208}\text{Pb}$**  Since 1980s, there have been several attempts to extract the neutron density distribution or the neutron skin thickness of  $^{208}\text{Pb}$  as listed in Table 1.1. They were all deduced by using hadronic reaction and consistent with each other within the errors. However, except for the  $^{208}\text{Pb}(p, p)$  at 650 MeV analysis, they must assume a specific model-dependent function or a specific theoretical calculation as the neutron density distribution of  $^{208}\text{Pb}$  because they cannot reduce the large uncertainties caused by the various model assumptions. Thus, the uncertainties associated with the theoretical models are inherent in all the results listed in Table 1.1. It is difficult to estimate the errors due to the model uncertainties, which are usually not mentioned, but they really should do unless they use hadronic probes. On the other hand, wide-ranged angular distributions of scattering observables are powerful tools to evaluate how precisely the reaction and structure models can explain the real data. In addition, we used the realistic proton density and the effective  $NN$  interaction tuned by the real data. This enables us to reduce the ambiguity of the reaction model and to use the model-independent density distributions.

There have been also several attempts to extract the neutron density distributions of  $^{208}\text{Pb}$  from proton elastic scattering data [58, 62]. The energy of the incident protons,  $E_p = 650$  and  $800 \text{ MeV}$  used in Refs. [58, 62] are rather high, where the real part of the optical potential is completely repulsive and the imaginary part is about  $50 \text{ MeV}$  deep. Thus the information about the nuclear interior is masked by the strong absorption. To avoid this large ambiguity

Table 1.1: The previous results of  $r_n$ ,  $r_p$  and  $\Delta r_{np}$  for  $^{208}\text{Pb}$  deduced from several experiments using various hadronic probes (all in fm). Except for X-ray cascade from  $\bar{p}$ -atom (2), the errors are experimental only.

Experiment	$r_p$	$r_n$	$\Delta r_{np}$
$^{208}\text{Pb}(p, p)$ at 800 MeV [58]*	5.45	5.59(4)	0.14(4)
$^{208}\text{Pb}(p, p)$ at 650 MeV [62]†	5.46	5.66(4)	0.20(4)
Isospin diffusion data in Sn + Sn at 50 MeV/u [51]‡	-	-	0.22(4)
GDR from $(\alpha, \alpha')$ at 120 MeV[61]	-	-	0.19(9)
PDR from $^{129-132}\text{Sn}(\gamma, \gamma')$ [68]¶	-	-	0.18(4)
PDR in $^{68}\text{Ni}$ and $^{132}\text{Sn}$ [72]	-	-	0.194(24)
X-ray cascade from $\bar{p}$ -atom (1)[67]**	5.44	5.60	0.16(2) <sub>stat</sub> (4) <sub>syst</sub>
X-ray cascade from $\bar{p}$ -atom (2)[73]††	5.45	5.65(5) <sub>mdl</sub>	0.20(4) <sub>exp</sub> (5) <sub>mdl</sub>

\*2nd-order KMT potential assuming 3pG neutron density.

†Density-dependent  $t$ -matrix using model-independent FB neutron density.

‡21 sets of the Skyrme interaction parameters.

¶PDR strengths analyzed by RHB+RQRPA calculations with DD-ME parametrization.

||Energy weighted sum rule by PDR data globally fitted with various mean field models

\*\*antiproton-nucleus optical potentials assuming 2pF proton and neutron density.

††newly developed Skyrme parametrization Skxsxx constrained by antiproton data of Ref. [67].

of the interior structure, Starodubsky and Hintz [62] assumed that the nuclear matter density in the nuclear interior is almost constant. They did not use the model-independent function itself to extract the neutron density, but instead used the Skyrme–Hartree–Fock density plus a small correction expanded in a Fourier–Bessel series to estimate the error-envelopes of the neutron densities which reflect only the statistical errors of the experimental data. They also used a density-dependent  $t$  matrix calibrated by  $p$ - $^{40}\text{Ca}$  scattering data in the framework of the non-relativistic formalism. Their approach is very similar to ours, as seen in our previous study for tin isotopes [70], but they did not estimate the errors due to the model ambiguity, which is an unavoidable problem in describing hadronic reactions.

There are several theoretical approaches for energy-independent global analysis. Skyrme–Hartree–Fock models with modern parameterizations have been tested employing the  $g$ -folding optical potential to explain the data obtained from nucleon-nucleus elastic scattering from  $^{208}\text{Pb}$  at 40, 65, and 200 MeV [63]. It has been suggested that  $^{208}\text{Pb}$  has a neutron skin thickness of  $\sim 0.17$  fm, because the SkM\* model gives the best agreement with the experimental data. Another global analysis of proton-nucleus elastic scattering data in the energy range from 500 to 1040 MeV based on the Dirac phenomenological optical model in Ref. [64] gave a range of  $\Delta r_{np}$  from 0.083 to 0.111 fm for  $^{208}\text{Pb}$ . The obtained range of  $\Delta r_{np}$  changes depending on the momentum transfer range and the  $NN$  interaction used for the global fit. In

these theoretical approaches, statistical errors and the effect of the model-dependence must be considered in the error-estimation of  $\Delta r_{np}$ .

As a different experimental approach, a parity-violating electron elastic scattering measurement to extract the neutron radius in  $^{208}\text{Pb}$  (PREX) has been proposed at Jefferson Laboratory [74, 75]. This challenging experiment is planned to measure the neutron rms radius for  $^{208}\text{Pb}$  with an accuracy of 1 % assuming a simple model-dependent function such as a Woods-Saxon for the neutron density of  $^{208}\text{Pb}$ . The advantage of this method is said to be its “model independence” of the interaction mechanism, but the planned accuracy of 1 % is larger than the recent measurements using hadronic probes [62, 67, 68]. Besides this electroweak probe measurement has many experimental difficulties because of the required accuracy to measure the very “weak” violation ( $\sim 0.1 \text{ ppm} = 10^{-7}$ ).

**Previous analyses for the EOS parameters** Several studies including listed Refs. in Table 1.1 deduced the  $\mathcal{S}(\rho_{\text{sat}})$  and  $L$  from various measurements such as isospin diffusion [51], pigmy dipole resonance [68, 72], and world data of various nuclear reactions [76]. The extracted regions are not so different each other, but widely spread, even though the uncertainties associated with the dependence of a certain theoretical model were not considered. Figures 1.8 and 1.9 taken from Refs. [72, 76], show that the recent results of the slope coefficient  $L$  are summarized. Thus, the situation of the EOS parameters is similar to that of the neutron skin thickness for  $^{208}\text{Pb}$  as mentioned above. Our approach may be also effective to constrain the theoretical models and the EOS parameters. The study for other nuclei as well as lead isotopes will give us more strict constraint on the EOS parameters.

This work aimed to extract the model-independent neutron density distributions and neutron rms radius of  $^{204,206,208}\text{Pb}$  with an accuracy of 1 % ( $\delta r_n/r_n$ ) even including the model uncertainties. This accuracy is comparable to the planned accuracy of the PREX experiment.

In this thesis we report our results of quantifying the uncertainty of both the experimental data and the present reaction model as the errors of the neutron densities in lead isotopes. The experimental procedures are described in Chap. 2. The experimental data of proton elastic scattering from  $^{58}\text{Ni}$ , and  $^{204,206,208}\text{Pb}$  at  $E_p = 295 \text{ MeV}$  have been newly obtained and several improvements have been applied at the data reduction, as explained in Chap. 3. so as to reduce the systematic uncertainties which have not been considered previously. This work is mainly based on the approach and technique described in Refs. [69, 70]. A brief outline of the medium-modified RIA model and the results of the extraction of the neutron density distributions in lead isotopes are given in Chap. 4. The extracted neutron rms radii and skin thickness are compared with several theoretical calculations in Chap. 5. Finally we provide a summary in Chap. 6.

This thesis is mainly based on the recent article Ref. [77].

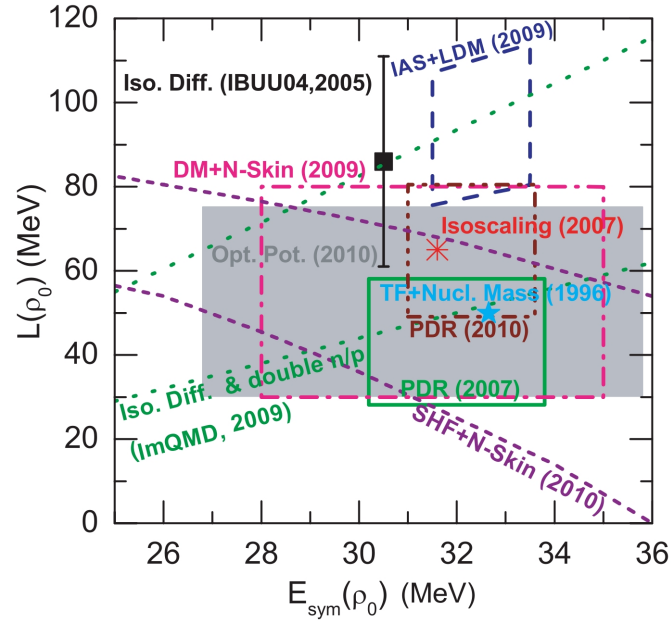


Figure 1.8: Constraint regions on the  $S(\rho_{\text{sat}})$ - $L$  plane by several recent analyses. Taken from Ref. [76].

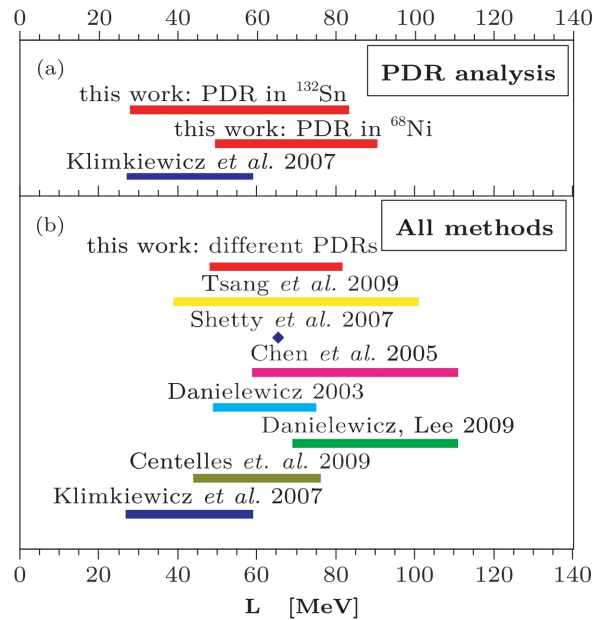


Figure 1.9: Constraint regions on the  $L$  by several recent analyses. Taken from Ref. [72].



# Chapter 2

## EXPERIMENTAL PROCEDURE

The experiment (E248) was performed at the ring cyclotron facility in the Research Center for Nuclear Physics (RCNP), Osaka University. An overview of the RCNP facility is shown in Fig. 2.1. The polarized proton elastic scattering from  $^{58}\text{Ni}$ , and  $^{204,206,208}\text{Pb}$  at  $E_p = 295$  MeV was measured by using the high-resolution magnetic spectrometer, “Grand Raiden” [78] and focal plane detectors [79]. Differential cross sections and analyzing powers were obtained in the angular range of  $7.5^\circ \leq \theta_{\text{lab}} \leq 48.0^\circ$ . In this chapter the details about the experimental setup and procedure are described.

### 2.1 Beam line

#### 2.1.1 Polarized proton beam

A high intensity polarized ion source (HIPIS) provided a polarized proton beam employing the cold atomic beam technology ( $\sim 30$  K) and an electron cyclotron resonance ionizer [80]. The polarized proton beam extracted from HIPIS was injected to an azimuthally varying field (AVF) cyclotron (K120) to keep the polarization axis in the vertical direction. The beam at 53 MeV after acceleration with the AVF cyclotron was further accelerated up to 295 MeV using a six sector ring cyclotron (K400) in a coupled mode. Since the single turn extraction from the ring cyclotron was achieved, the beam was very clean and free from the background caused by other bunches. The vertically polarized proton beam from the ring cyclotron was achromatically transported to the WS beam line and scattered at a target in a scattering chamber. A typical size of the beam spot was less than 1 mm in diameter.

A schematic view of the WS beam line in the experimental hall is shown in Fig. 2.2. The beam was tuned by using many constituent elements of the beam line such as dipole, quadrupole, and steering magnets, and beam viewers so that the beam was transported along the central axis of the beam line arranged in advance. Since the beam was achromatically transported on the target, if the drift of the beam energy occurred due to instabilities of the beam conditions, we cannot recognize the drift by the beam spot on the target position only. Therefore, during the experiment we regularly checked the two beam viewers of BV9-WS

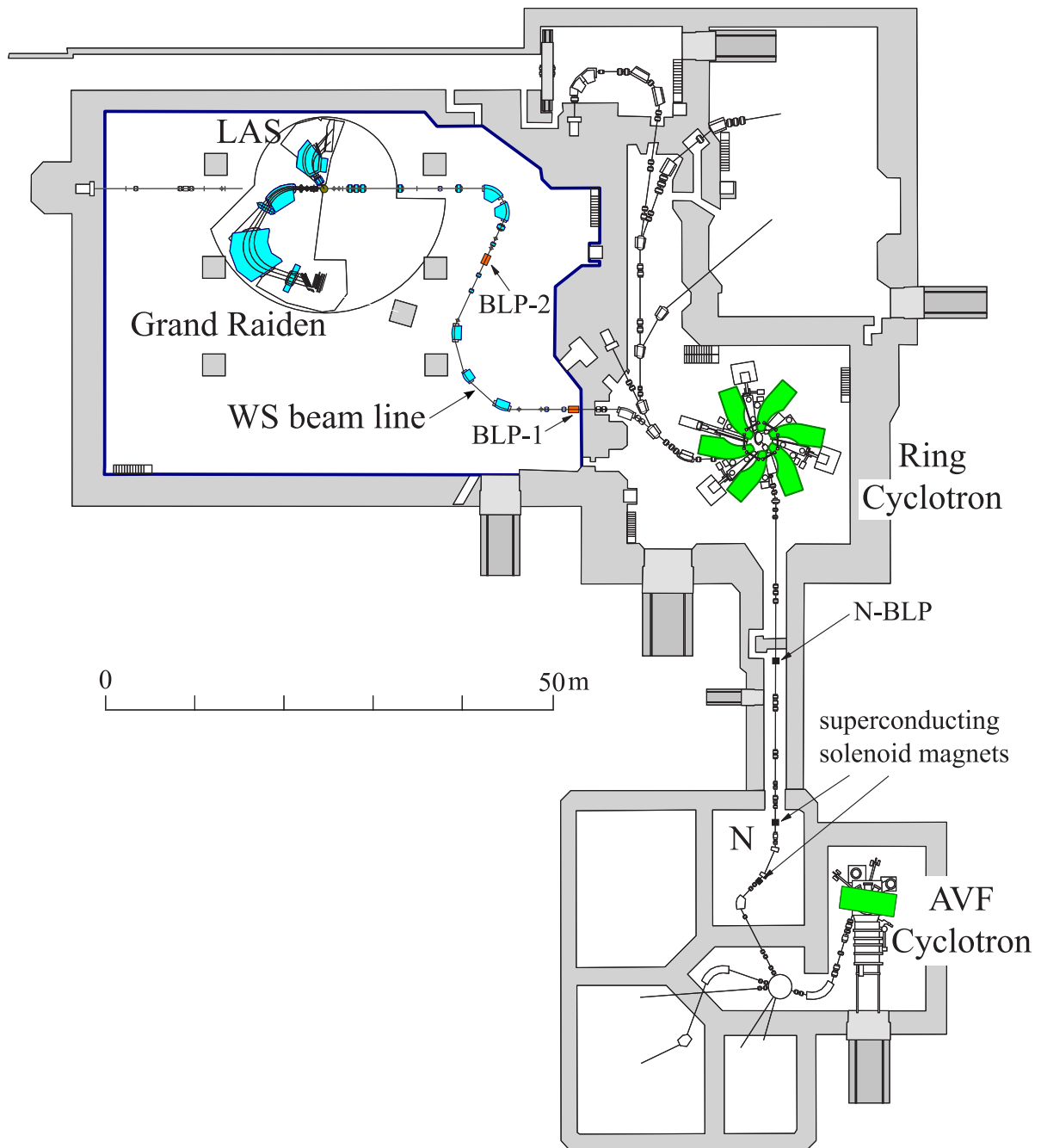


Figure 2.1: Overview of the RCNP ring cyclotron facility with the WS beam line. AVF and Ring cyclotron operate in a coupled mode and provide polarized proton beam at  $E_p = 295$  MeV to the WS beam line in west experimental hall.

and BV8-WS located at momentum-dispersive positions ( $\sim 3$  m and  $\sim 10$  m upstream from the target position, respectively) as shown in Fig. 2.2. At BV9-WS, for example, the dispersion is

## WS beam line in West Experimental Hall @ RCNP

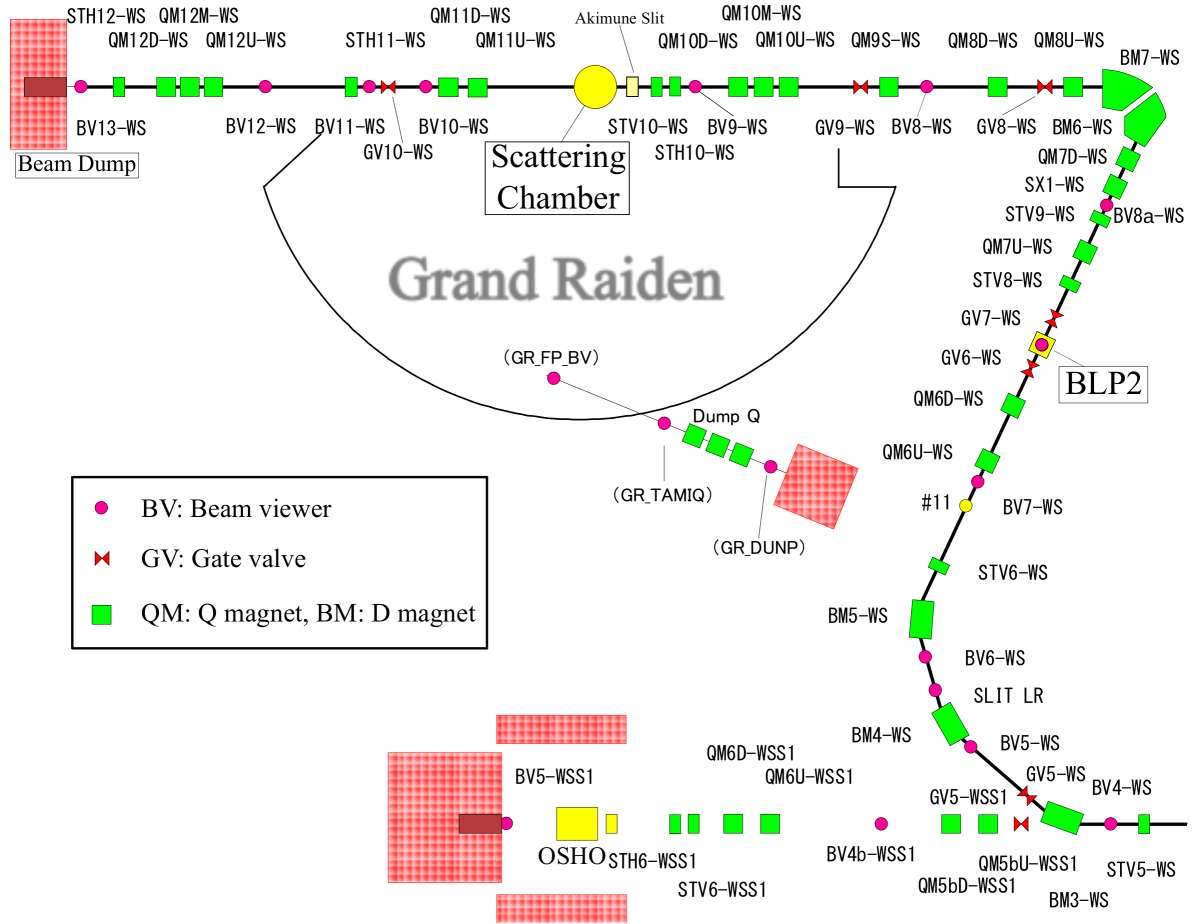


Figure 2.2: Schematic view of WS beam line

about  $\pm 5$  mm, this value corresponds to the range of the beam incident angle  $-0.1^\circ \leq \theta_{\text{inc.}} \leq 0.1^\circ$  ( $\pm 5/3000$  rad). Thus, the uncertainty of the incident beam angle was approximately,  $\delta\theta_{\text{inc.}} \approx \pm 0.02^\circ$  after the beam spot at BV9-WS were narrowed enough to distinguish the 1 mm drift of the beam at BV9-WS by eyes. The effect of this uncertainty on the scattering observables is referred to in Chap. 3.4.

### 2.1.2 Beam line polarimeter

The polarization of the proton beam was constantly monitored by using a sampling-type beam line polarimeter (BLP) placed in the WS beam line. The BLP consists of four (left, right, up, and down) pairs of plastic scintillation counters to measure  $p$ -H scattering from the  $(\text{CH}_2)_n$  foil. In Fig. 2.3 the top view of the BLP is shown and the left and right pairs of counters in the horizontal plane can be seen. The other (up and down) pairs are located in the vertical plane.

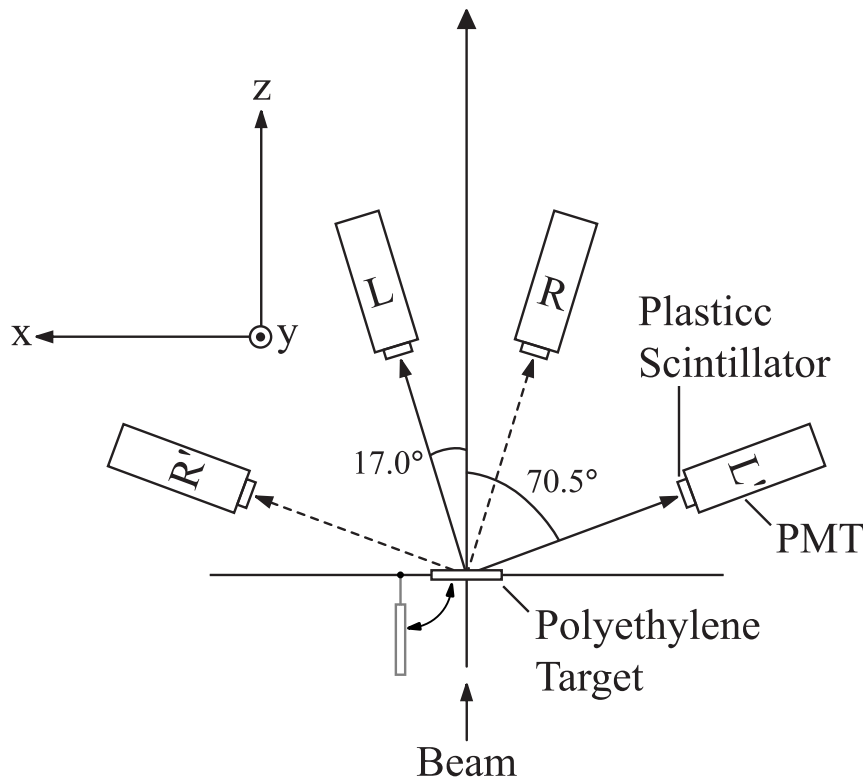


Figure 2.3: Setup of the BLP (top view)

A proton in the beam was elastically or quasi-elastically scattered from another proton of hydrogen or carbon in the  $(\text{CH}_2)_n$  foil and the scattered and recoiled protons are simultaneously detected with a pair of scintillation counters. Each pair of scintillation counters was located at the scattering and recoil angles of  $17.0^\circ$  and  $70.5^\circ$  where  $p$ - $p$  scattering from  $(\text{CH}_2)_n$  realizes the large effective analyzing power  $A_y = 0.40$ . The  $y$ -component of the polarization was derived from the asymmetry of the number of the events counted by the left and right pairs of scintillation counters. A typical beam polarization was about 70 %. The up and down pairs of the counters were used to determine the beam intensity during the measurements as mentioned in Sec. 2.3.

The polyethylene target was periodically inserted into the beam position during the polarization measurement, while it was removed out of the beam position during the data acquisition of the focal-plane events. The polarization direction of the proton beam was reversed for every one second to reduce the systematic asymmetries.

## 2.2 Targets

Self-supporting metal foils were used as  $^{204,206,208}\text{Pb}$  and  $^{58}\text{Ni}$  targets in this experiment. Two types of thin and thick metal foils were prepared for each target except for  $^{204}\text{Pb}$ . Thin targets

were for the measurements at forward angles ( $7.5^\circ \leq \theta_{\text{lab}} \leq 28.5^\circ$ ) in order to reduce the dead time of the data acquisition less than 10 %, while thick ones were for the measurements at backward angles ( $25.5^\circ \leq \theta_{\text{lab}} \leq 48.0^\circ$ ) to increase the yields. The thicknesses and enrichments of the targets are listed in Table 2.1.

In order to reduce the relative systematic errors due to instabilities of the beam condition or detectors, the four targets were automatically interchanged every  $\sim 5$  minutes at each scattering angle. Typically the errors of the target thicknesses are about 1 %.

Table 2.1: Target thicknesses and enrichments of Ni, and lead isotopes.

Nucleus	Thin	Thick	Enrichment
$^{204}\text{Pb}$	23.7 mg/cm <sup>2</sup>	not prepared	99.6 %
$^{206}\text{Pb}$	18.4 mg/cm <sup>2</sup>	50.9 mg/cm <sup>2</sup>	99.3 %
$^{208}\text{Pb}$	31.5 mg/cm <sup>2</sup>	78.8 mg/cm <sup>2</sup>	99.7 %
$^{58}\text{Ni}$	39.5 mg/cm <sup>2</sup>	100 mg/cm <sup>2</sup>	99.39 %

## 2.3 Faraday Cups

The proton beam was stopped by two kinds of Faraday cups depending on the settings of the measurement. In the measurements at forward angles ( $7.5^\circ \leq \theta_{\text{lab}} \leq 28.5^\circ$ ) the Faraday cup was mounted inside the scattering chamber (SCFC). This Faraday cup was most stable against the fluctuations of the beam profile, and its charge collection efficiency has been measured by a separate experiment [71].

In the measurements at backward angles ( $25.5^\circ \leq \theta_{\text{lab}} \leq 48.0^\circ$ ) the intensity of the proton beam was much higher than that for the forward measurements to increase the yields. The other Faraday cup located about 25 m downstream from the scattering chamber (WallFC) was used due to the regulation of the radiation control. The relative charge collection efficiency between the SCFC and WallFC was monitored by using  $p$ -H cross section counted by up and down pairs of BLP.

## 2.4 Magnetic spectrometer, “Grand Raiden”

Scattered particles from a target nucleus were analyzed using the high resolution magnetic spectrometer “Grand Raiden” (GR) [78]. Figure 2.4 shows a schematic view of the GR spectrometer and focal plane detectors [79].

The GR spectrometer has a Q1-SX-Q2-D1(-MP)-D2(-DSR) configuration, where D, Q, and SX denote a dipole, a quadrupole, and a sextupole magnet, respectively. Design specifications of the spectrometer are summarized in Table 2.2. The multipole magnet (MP) is designed

Table 2.2: Design specifications of the GR spectrometer

Configuration	Q1-SX-Q2-D1(-MP)-D2(-DSR)
Mean orbit radius	3 m
Total deflection angle	162°
Measureable angle	-4°-90°
Focal plane length	120 cm
Focal plane tilting angle	45°
Maximum magnetic rigidity	5.4 T·m
Momentum range	5%
Momentum resolution ( $p/\Delta p$ )	37000
Momentum dispersion ( $x \delta$ )	15.45 m
Horizontal magnification ( $x x$ )	-0.417
Vertical magnification ( $y y$ )	5.98

to minimize the higher-order aberrations. The third dipole magnet (DSR) is additionally used for measurements of the spin rotation parameters or the polarization transfers. The MP and DSR magnets were not used in the present experiment.

The GR spectrometer can rotate around the axis located at the center of the scattering chamber from  $-4^\circ$  to  $90^\circ$ . Therefore we can obtain the angular distributions of the scattering observables such as the cross sections, analyzing powers, and spin rotation parameters using polarized beam. In this experiment, we measured the polarized proton scattering over the angular range covered from  $7.5^\circ$  to  $48.5^\circ$  in  $1.5^\circ$  steps. This angular range corresponds to the momentum transfer from  $0.55 \text{ fm}^{-1}$  up to  $3.5 \text{ fm}^{-1}$ .

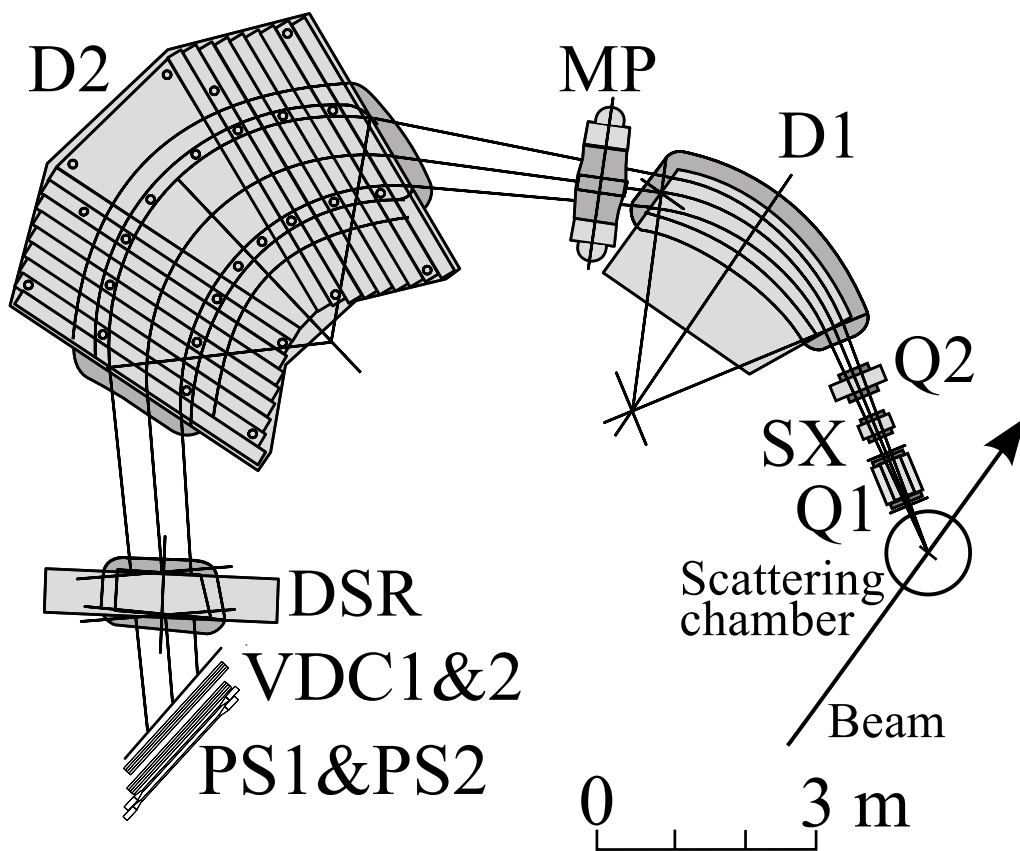


Figure 2.4: Schematic view of the magnetic spectrometer, "Grand Raiden"

Table 2.3: Specifications of the VDCs.

Wire configuration	X(0°), U(-48.2°)
Active area	1150 <sup>W</sup> mm × 120 <sup>H</sup> mm
Number of sense wires	192(X), 208(U)
Anode-cathode gap	10 mm
Anode wire spacing	2 mm
Sense wire spacing	6 mm (X), 4 mm (U)
Sense wires	20 $\mu\text{m}\phi$ gold-plated tungsten wire
Potential wires	50 $\mu\text{m}\phi$ gold-plated beryllium-copper wire
Cathode	10 $\mu\text{m}$ -thick carbon-aramid film
Applied voltage	-5.6 kV (cathode), -0.3 kV (potential), 0 V (sense)
Gas mixture	Argon (71.4%) + Iso-butane (28.6%) + Isopropyl-alcohol
Entrance and exit window	12.5 $\mu\text{m}$ aramid film
Pre-amplifier	LeCroy 2735DC
Digitizer	LeCroy 3377 TDC

## 2.5 Focal plane detectors

The trajectories of the scattered particles were reconstructed from two sets (X1, U1 and X2, U2) of vertical-type multi-wire drift chambers (VDCs) [79]. VDCs were placed at the focal plane of the GR spectrometer. Specifications of VDCs are summarized in Table 2.3. Each VDC consists of two sets of anode wire planes (X and U), sandwiched between three cathode planes. The structure of a X plane is illustrated in Fig. 2.5. Sense wire spacings are 6 mm and 4 mm for X and U planes, respectively, as shown in Fig. 2.6.

VDCs were filled with mixture gas of argon (71.4%), iso-butane (28.6%), and iso-propyl-alcohol. The saturated vapor of iso-propyl-alcohol at 2°C and 1 atm was used to avoid a gain loss caused by aging effects such as polymerizations of the quencher gas, which contaminate the anode wires. High voltages of -5.6 kV and -0.3 kV were supplied to the cathode planes and the potential wires, respectively, while the sense wires were grounded (0 V).

The atoms in the gas were ionized along the trajectory of the incoming charged particle. Electrons in ionized gas moved toward a sense wire. The drift velocity was almost constant and avalanche multiplications occurred near the sense wire where the electric field rapidly become strong. Signals from sense wires were amplified and discriminated with LeCroy 2735DC cards and timing information was digitized with LeCroy 3377 drift chamber TDC.

Two 1-cm-thick plastic scintillators (PS1 and PS2) right behind the VDCs were used to generate the trigger signals of the data acquisition. Timing and pulse-height information of the signals of PS1 and PS2 are digitized by using LeCroy FERA and FERET systems. A 1-cm-

thick aluminum plate was placed between the two plastic scintillators to prevent  $\delta$ -electrons knocked out by scattered particles at PS1 from entering PS2.

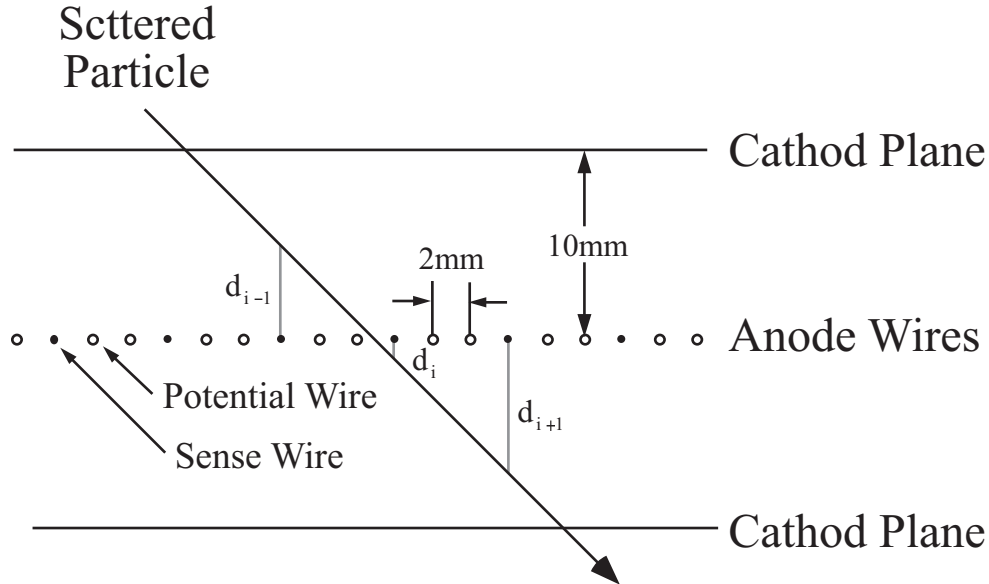


Figure 2.5: Structure of a X plane of the VDCs.

## 2.6 Trigger system

The readout electronics and trigger systems of the focal plane scintillators for GR are shown in Fig. 2.7. Output analog signals from plastic scintillators (PS1 and PS2) were divided into two passages, the one was discriminated by a constant fraction discriminator (CFD; Ortec 935) and the other was sent to a FERA (Fast Encoding and Readout ADC; LeCroy 4300B) module after a delay. One of the CFD outputs was transmitted to TFC (Time to FERA Converter) backed by FERA modules. A coincidence signal of the CFD outputs from both sides of the same scintillators was generated by a Mean-Timer circuit (REPIC PRN-070), in which the times of two signals were averaged.

The trigger system was constructed with LeCroy 2366 universal logic modules (ULM) with field programmable gate-array (FPGA) chips [81]. The logical circuits were designed using a CAD program on a personal computer and down-loaded to the ULMs. As shown in Fig. 2.7, the trigger system received signals from the outputs of the Mean Timers and generated the GR trigger by the coincidence of PS1 and PS2, internally.

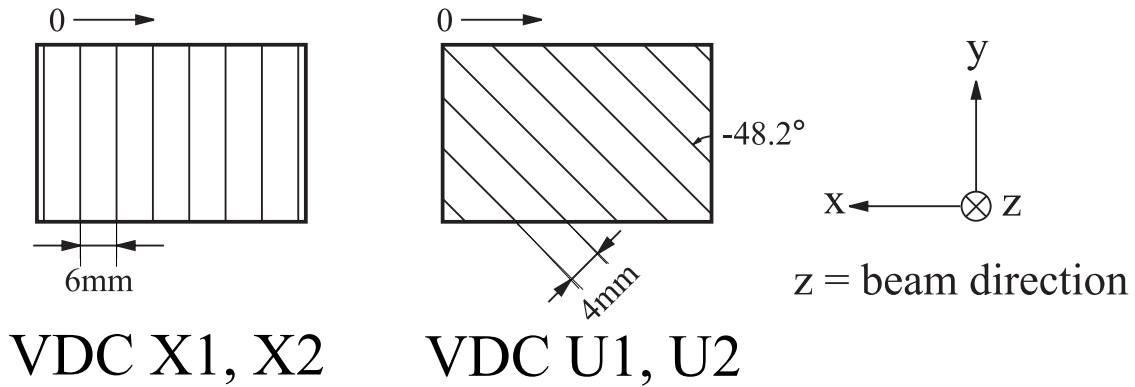


Figure 2.6: Wire configurations of the VDCs. The wire numbering orders are shown by the arrows

## 2.7 Data acquisition system

Schematic view of the data acquisition (DAQ) system [82, 83] is shown in Fig. 2.8. Two types of data line, i.e., the drift-time data detected by two VDCs and the charge and timing data detected by trigger scintillators (PS1 and PS2), existed in this experiment. They were digitized by LeCroy 3377 system and LeCroy FERA/TFC system, respectively, event by event. For the subsequent event reconstruction, an event header, an event counter, and input register words are attached to the each digitized data by using a specified modules, that is, the Flow Controlling Event Tagger (FCET) [84].

The digitized data for each detector system was transferred and accumulated in parallel via the ECL bus to high speed memory modules (HSM) in the VME crate. Each data line was connected to a pair of two HSMs, which worked in a double-buffer mode to reduce the dead time caused by the transfer of the buffered data. Finally, the buffered data was transferred and stored in the work station server “IBM RS/6000 SP” via the Gigabit Ethernet link. The event reconstruction and online data analysis were performed also on this computer.

This data readout flow completely starts with hardware logics, which does not include software management nor CAMAC functions. Therefore the typical dead time for an event is less than 30 micro seconds. In the present experiment, the acquired data is about 50 GBytes.

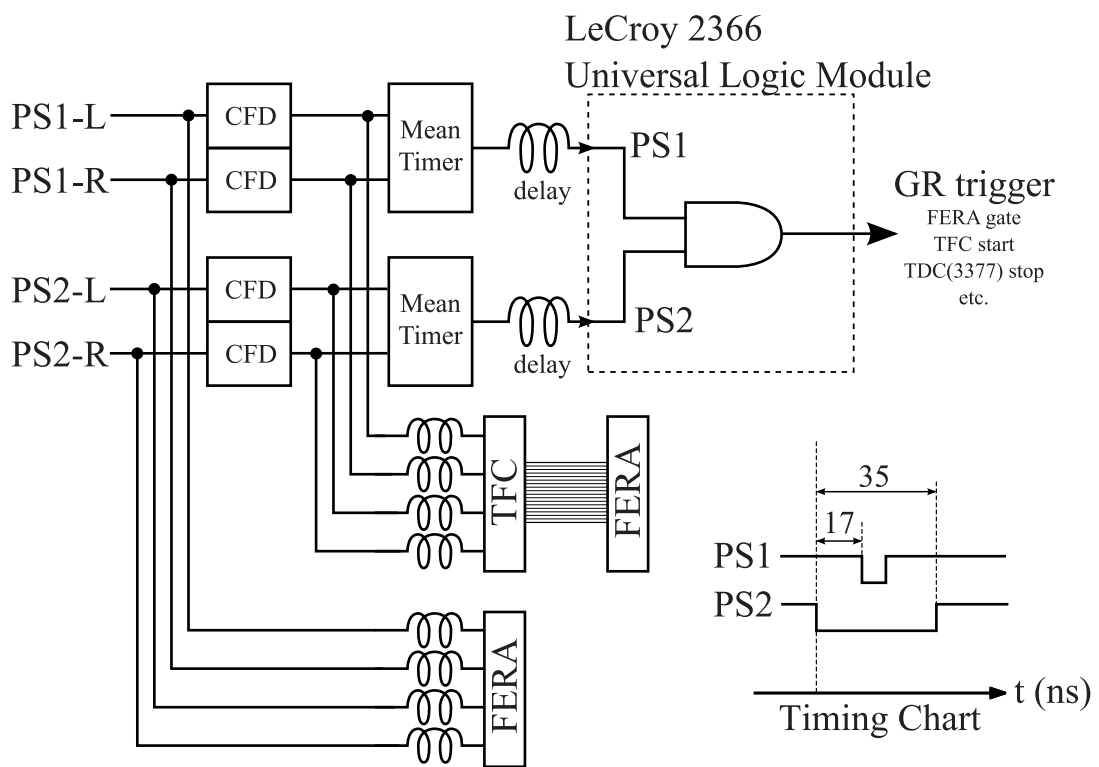


Figure 2.7: Wire configurations of the VDCs. The wire numbering orders are shown by the arrows

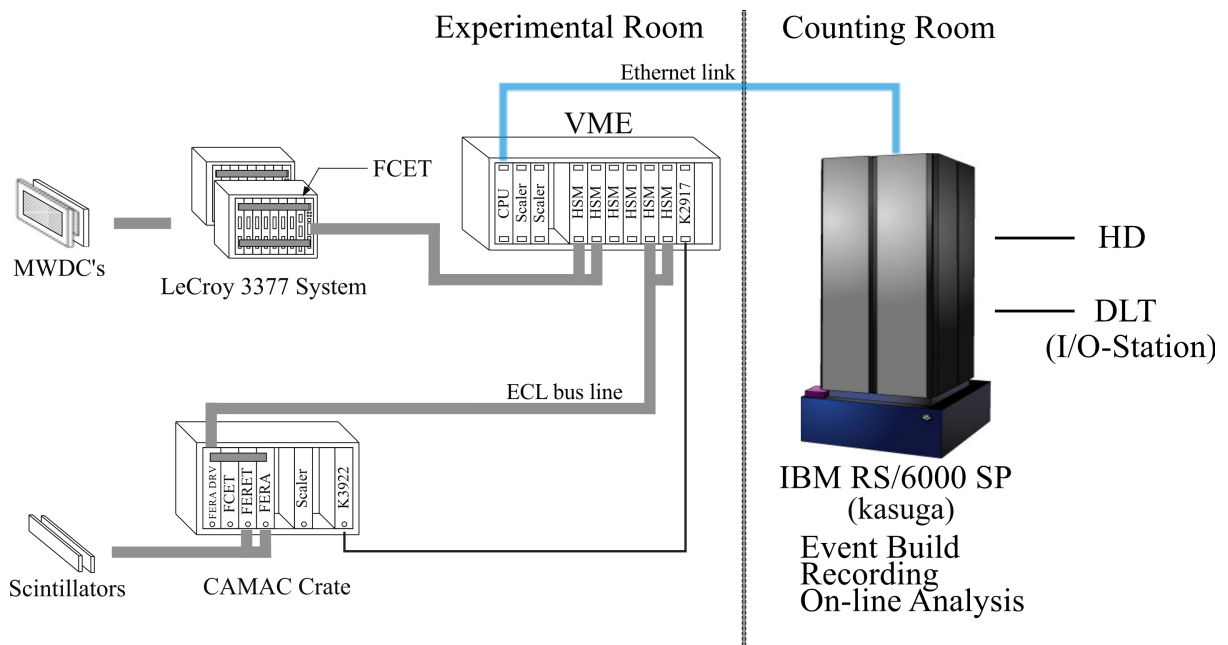


Figure 2.8: Schematic view of the data acquisition system

# Chapter 3

## DATA REDUCTION & RESULTS

The data reduction was performed by using the central computing system at RCNP, i.e., IBM RS/6000 SP system named “kasuga”.

The acquired data consists of the BLP data and the focal plane detectors data. While the BLP data was used to determine and calibrate the beam properties such as the beam polarizations and the beam intensities, the data of the focal plane detectors was used to identify the incoming particles and to determine their focal plane positions, i.e., to obtain the elastically scattered proton events. Now the details of these procedures are described in this chapter.

### 3.1 BLP data

Yields on the four ( $L$ ,  $R$ ,  $U$ , and  $D$ ) pairs of scintillators ( $N_L$ ,  $N_R$ ,  $N_U$ , and  $N_D$ ) at the BLP for spin-up ( $\uparrow$ ) and spin-down ( $\downarrow$ ) modes are described as

$$N_{L(U)}^{\uparrow} = N_{L(U)}^{p\uparrow} - N_{L(U)}^{a\uparrow} = \sigma_0 N_0 N_b^{\uparrow} \epsilon_{L(U)} \Delta\Omega_{L(U)} (1 + A_y p_{y(x)}^{\uparrow}), \quad (3.1)$$

$$N_{R(D)}^{\uparrow} = N_{R(D)}^{p\uparrow} - N_{R(D)}^{a\uparrow} = \sigma_0 N_0 N_b^{\uparrow} \epsilon_{R(D)} \Delta\Omega_{R(D)} (1 - A_y p_{y(x)}^{\uparrow}), \quad (3.2)$$

$$N_{L(U)}^{\downarrow} = N_{L(U)}^{p\downarrow} - N_{L(U)}^{a\downarrow} = \sigma_0 N_0 N_b^{\downarrow} \epsilon_{L(U)} \Delta\Omega_{L(U)} (1 + A_y p_{y(x)}^{\downarrow}), \quad (3.3)$$

$$N_{R(D)}^{\downarrow} = N_{R(D)}^{p\downarrow} - N_{R(D)}^{a\downarrow} = \sigma_0 N_0 N_b^{\downarrow} \epsilon_{R(D)} \Delta\Omega_{R(D)} (1 - A_y p_{y(x)}^{\downarrow}), \quad (3.4)$$

where  $N_p$  and  $N_a$  are the numbers of prompt and accidental coincidence events measured by BLP, respectively.  $\sigma_0$  and  $A_y$  are the unpolarized cross section and analyzing power for  $p$ -H scattering from polyethylene target.  $N_0$  and  $N_b$  are numbers of the target and beam particles.  $p_{y(x)}$  is the vertical (horizontal) component of the beam polarization and  $p^{\downarrow} \leq 0 \leq p^{\uparrow}$ .  $\epsilon$  and  $\Delta\Omega$  are the efficiency and solid angle of each detector. The scattering angles of forward and backward protons were  $\theta_{lab} = 17.0^\circ$  and  $70.5^\circ$  for 295 MeV proton beam, respectively.

#### 3.1.1 Beam polarization

The beam polarization was determined by using the left-right asymmetry at BLP as described in Sec. 2.1.1. The analyzing powers of  $A_y = 0.40 \pm 0.01$  for the inclusive ( $p$ ,  $2p$ ) scattering from

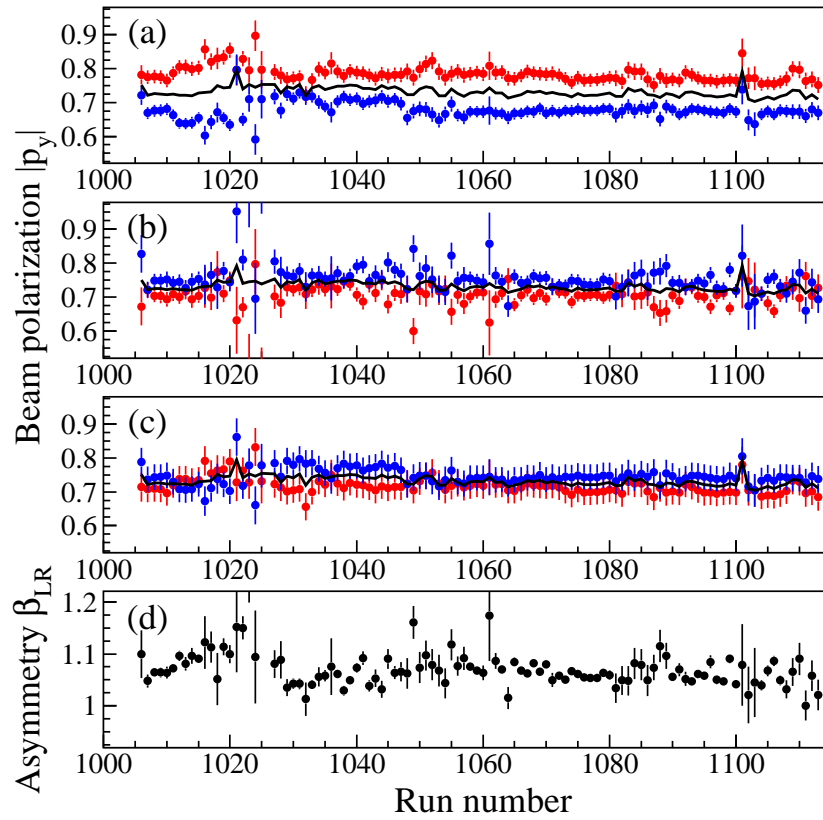


Figure 3.1: Three types of beam polarization (a, b, c) and instrumental asymmetry (d) for each run. Red and blue circles mean  $|p^{\uparrow(\downarrow)}|$  (spin-up and -down mode). Beam polarizations (a) assuming asymmetry  $\beta_{LR} = 1$ , (b) using each  $\beta_{LR}$ , and (c) using the averaged  $\beta_{LR}$  fitted by a Gaussian as shown in Fig. 3.2 are compared with each other. In this data reduction the type of (c) was used.

the polyethylene target, which was previously calibrated by another BLP installed between the AVF and ring cyclotrons [85, 86], was used to determine the beam polarization.

The beam polarization can be obtained from Eq. (3.1), (3.2), (3.3), (3.4) as follows:

$$p_y^{\uparrow(\downarrow)} = \frac{1}{A_y} \frac{N_L^{\uparrow(\downarrow)} - \beta_{LR} N_R^{\uparrow(\downarrow)}}{N_L^{\uparrow(\downarrow)} + \beta_{LR} N_R^{\uparrow(\downarrow)}}, \quad (3.5)$$

$$\beta_{LR} \equiv \frac{\epsilon_L \Delta \Omega_L}{\epsilon_R \Delta \Omega_R} = \frac{N_L^{\downarrow} N_b^{\uparrow} - N_L^{\uparrow} N_b^{\downarrow}}{N_R^{\uparrow} N_b^{\downarrow} - N_R^{\downarrow} N_b^{\uparrow}} = \frac{N_L^{\downarrow} Q^{\uparrow} - N_L^{\uparrow} Q^{\downarrow}}{N_R^{\uparrow} Q^{\downarrow} - N_R^{\downarrow} Q^{\uparrow}}, \quad (3.6)$$

where  $Q$  is the charge of the proton beam collected by SCFC or WallFC. Since  $\beta_{LR}$  in Eq. (3.6) is the form of the fraction, the collection efficiency of each Faraday cup is canceled out. The instrumental asymmetry  $\beta_{LR}$  should be constant and independent from the beam polarization during the measurement. However, due to instabilities of the beam condition or detectors the

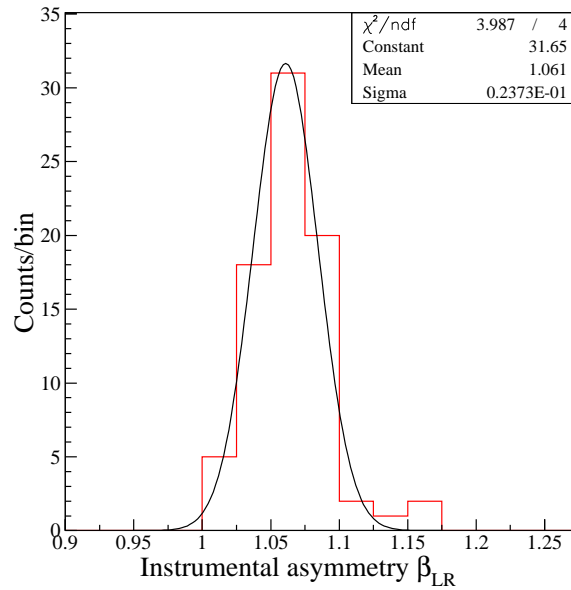


Figure 3.2: The projection of the instrumental asymmetries  $\beta_{LR}$  in Fig. 3.1(d) was fitted with a Gaussian.

asymmetry  $\beta_{LR}$  calculated from Eq. (3.6) fluctuated for each run as shown in Fig. 3.1(d). Since the trigger rate dependence of  $\beta_{LR}$  was not seen, the main source of this fluctuation is thought to be the beam instabilities.

Figure 3.1(a), (b), and (c) show three types of the beam polarization  $|p^{\uparrow(\downarrow)}|$  for each run. Red and blue circles represent spin-up and spin-down mode, respectively. The three types (a), (b), and (c) in Fig. 3.1 means the calculations of beam polarizations using three different  $\beta_{LR}$ ; (a) assuming no instrumental asymmetry, that is,  $\beta_{LR} = 1$ , (b) using  $\beta_{LR}$  calculated for each run, and (c) using the averaged value of  $\beta_{LR}$ . The averaged  $\beta_{LR}$  was determined from the projection of the instrumental asymmetries  $\beta_{LR}$  of Fig. 3.1(d). The histogram in Fig. 3.2 was fitted with a Gaussian. The half width at half maximum (HWHM) of the fitted Gaussian is used as an uncertainty of the averaged  $\beta_{LR}$ . The solid lines in (a), (b), and (c) are the arithmetic means of spin-up and -down beam polarizations for each type of polarization. It is found that the solid lines are almost constant and the same with each other independently from run number and the types of the  $\beta_{LR}$ . This means that the polarization of the protons produced by the ion source kept stable during the experiment and independent from the instability of the beam conditions such as the energy and the transmission which mainly depend on the beam line and the cyclotrons.

While the polarizations calculated by type (b) are unstable due to the fluctuated  $\beta_{LR}$ , the type (c) calculation realized stable  $|p_y|$  since the constant value of  $\beta_{LR} = 1.06(3)$  was used. The beam polarization the type (c) was used in this data reduction. The typical beam polarization was about 75 % during the measurement.

### 3.1.2 Beam intensity

In the measurements at backward angles the thick target and WallFC were used for high-intensity proton beam ( $\sim 400$  nA) as mentioned in Sec. 2.3. Because of the multiple scattering at a target, the transmission efficiency of the proton beam from the target to the WallFC is less than 100 %. Then we used the up and down pairs of the BLP detectors (U and D) to determine the relative charge collection efficiency of the WallFC to the SCFC including the loss of the beam transmission behind the target.

The absolute charge collection efficiency of the SCFC has been already calibrated by an separate experiment [71]. The SCFC, which is located right behind the target, can catch almost all the incident protons which enter the target area. Thus the SCFC is suitable for the reliable reference.

From Eqs. (3.1)-(3.4), the intensity of the incident proton beam ( $N_b^{\uparrow(\downarrow)}$ ) at the BLP is given as

$$N_b^{\uparrow(\downarrow)} = (N_U^{\uparrow(\downarrow)} + \frac{N_D^{\uparrow(\downarrow)}}{\beta_{UD}}) / (2\sigma_0 N_0 \epsilon_D \Delta\Omega_D), \quad (3.7)$$

$$\beta_{UD} \equiv \frac{\epsilon_U \Delta\Omega_U}{\epsilon_D \Delta\Omega_D} = \frac{N_U^\downarrow N_b^\uparrow - N_U^\uparrow N_b^\downarrow}{N_D^\uparrow N_b^\downarrow - N_D^\downarrow N_b^\uparrow}. \quad (3.8)$$

Assuming the transmission from the BLP to the Faraday Cup and the  $\epsilon\Delta\Omega$  are constant during the measurement, the beam charge  $Q_{\text{SC(Wall)}}$  collected by the SCFC (WallFC) is proportional to the number of the beam and the yield ( $N_U + N_D/\beta_{UD}$ ) from Eq. (3.7) as follows:

$$Q_{\text{SC(Wall)}} = R_{\text{SC(Wall)}} \cdot N_b = \frac{R_{\text{SC(Wall)}}}{2\sigma_0 N_0 \epsilon_D \Delta\Omega_D} \left( N_U + \frac{N_D}{\beta_{UD}} \right). \quad (3.9)$$

Thus the ratio  $R_{\text{SC(Wall)}}$  is described as

$$R_{\text{SC(Wall)}} = 2\sigma_0 N_0 \epsilon_D \Delta\Omega_D \frac{Q_{\text{SC(Wall)}}}{N_U + \frac{N_D}{\beta_{UD}}}. \quad (3.10)$$

From Eq. (3.10) the relative ratio  $R = R_{\text{Wall}}/R_{\text{SC}}$  was calculated for each run and target. The averaged ratio  $R$  for each target was determined as listed in Table 3.1. The ratio of  $^{204}\text{Pb}$  is relatively large compared to the other three targets. This is because the thin target was used for  $^{204}\text{Pb}$  only in the backward measurements. Compared to the case of the beam polarization in the previous subsection, the fluctuation of the up-down instrumental asymmetry  $\beta_{UD}$  were relatively small and hence, the errors of the ratios are about 1 % as shown in Table 3.1.

## 3.2 Particle identification

Timing and pulse-height information of trigger scintillators (PS1 and PS2) were used to identify the charged particle which triggered the event.

Table 3.1: The relative ratio  $R = R_{\text{Wall}}/R_{\text{SC}}$  of the beam collection efficiencies of SCFC and WallFC

Target	$^{204}\text{Pb}$	$^{206}\text{Pb}$	$^{208}\text{Pb}$	$^{58}\text{Ni}$
$R$	0.97(1)	0.95(1)	0.92(1)	0.95(1)

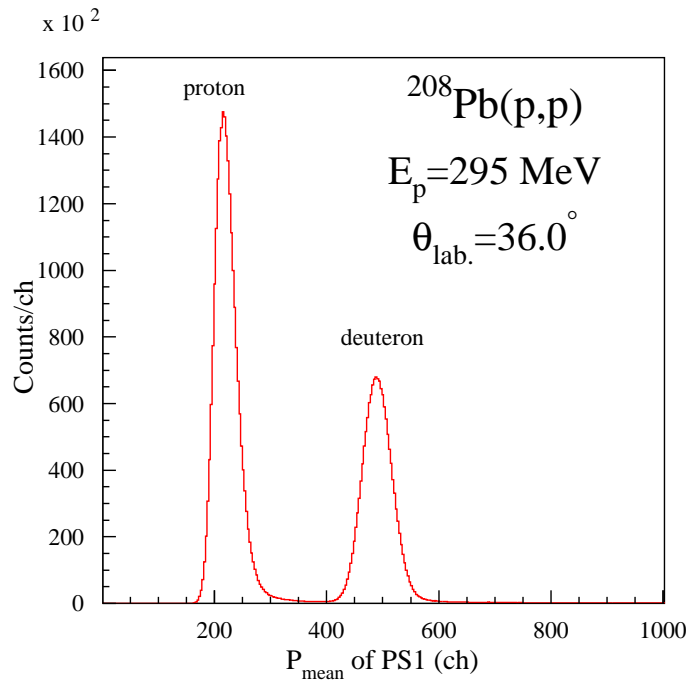


Figure 3.3: The spectrum of the geometrical mean  $\bar{P}$  of PS1. proton and deuteron peaks are identified.

The energy loss of a charged particle passing through a plastic scintillator ( $\Delta E$ ) depends on the charge and velocity as described by the well-known Bethe-Bloch formula. The scintillation photons produced at a position  $x$  where the charged particle passed through were detected by PMTs attached on both sides of a scintillator. The number of the scintillation photons initially produced at  $x$  was proportional to  $\Delta E$ , but it was attenuated due to the absorption in the material of the scintillator during the transmission. The number of photons entering a PMT ( $I$ ) is simply described as a function of position  $x$ ,

$$I(x) = I_0 \exp\left(-\frac{x}{l}\right), \quad (3.11)$$

where  $I_0$  is the initial number of photons at  $x$  and  $l$  is the attenuation length of the material. When the length of the scintillator is  $L$ , the numbers of photons at the both sides of the scintillator are  $I(x)$  and  $I(L - x)$ . The output charge of the left and right side of PMTs ( $P_L$  and  $P_R$ )

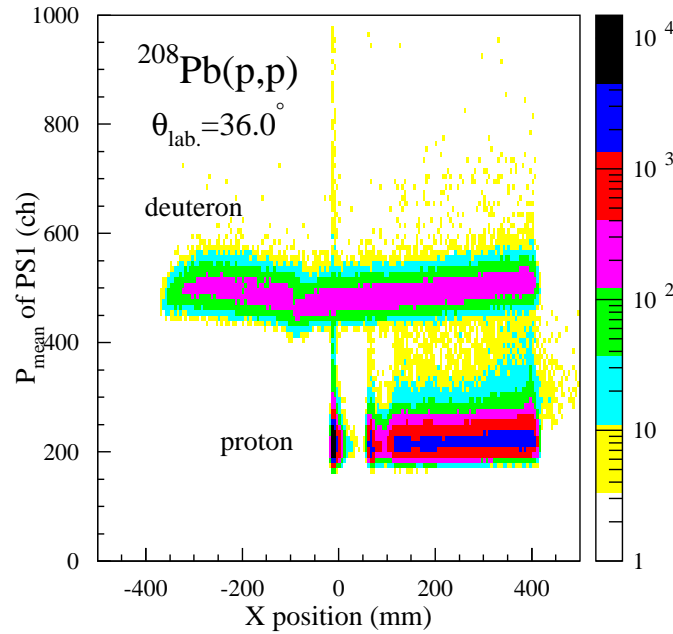


Figure 3.4: Colors plot of  $\bar{P}$  of PS1 versus the position spectrum at the focal plane. It is found that  $\bar{P}$  is independent of the focal plane position.

are proportional to  $I(x)$  and  $I(L - x)$  respectively. The geometrical mean  $\bar{P}$  of  $P_L$  and  $P_R$  is

$$\bar{P} = \sqrt{P_L \cdot P_R} \propto \sqrt{I(x) \cdot I(L - x)} = I_0 \exp\left(-\frac{L}{2l}\right). \quad (3.12)$$

$\bar{P}$  is independent of the position  $x$  and proportional to the initial number  $I_0$  and  $\Delta E$ . The  $\bar{P}$  spectra are useful for the particle identification (PID) as shown in Fig. 3.3. Figure 3.4 shows the  $\bar{P}$  of PS1 versus the X position at the focal plane. The X position at the focal plane was determined by VDCs data as written in the next section. The geometrical mean  $\bar{P}$  of PS1 is found to be independent of the position at the focal plane.

However the proton peak in the  $\Delta E$  spectrum has a tail structure over the deuteron peak region as clearly seen in Fig. 3.4. If only the  $\Delta E$  information was used for the particle identification, the proton events in the tail was cut off together with the deuteron and triton events. This causes the reduction of the yields, which accounts for about one percent of the total and is not negligible for the precise measurement of the cross sections, especially at the angles where the background events are relatively large.

Then the information about time of flight (TOF) was also used for PID. Figure 3.5 shows the time difference between the trigger produced by PS1 and PS2 and the radio-frequency (RF) signal of the AVF cyclotron. There exist two peaks in the Fig. 3.5 because the RF signals were downscaled to a half of its frequency. Two-dimensional colors plot of TOF versus the X position at the focal plane is also shown in Fig. 3.6. One can clearly distinguish the elastically

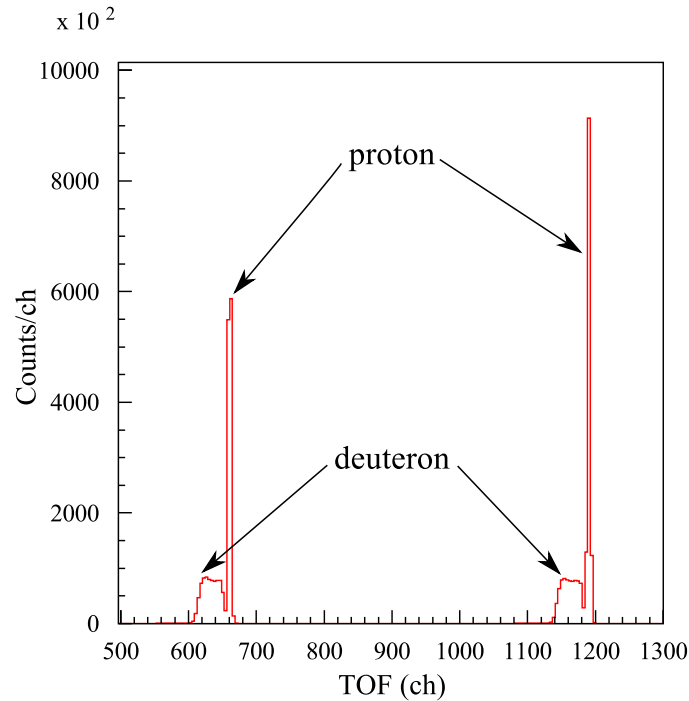


Figure 3.5: TOF spectrum between the trigger and the downscaled RF.

scattered protons from deuterons. It is found that the TOF spectrum is useful to identify the proton events. Figure 3.7 shows the two-dimensional plot of TOF versus  $\Delta E$  which was finally used for PID. The area surrounded by the dashed lines was used as the gate of the proton events.

## 3.3 Multi-wire drift chambers

### 3.3.1 Track reconstruction of scattered particles

As mentioned in Sec. 2.5, the scattered particles analyzed by the GR spectrometer were detected with VDCs at the focal plane. Since a charged particle enters VDCs in the  $45^\circ$  direction, the number of hit wires in one plane is usually more than three as shown in Fig. 2.5 while the background events such as the  $X$ - and  $\gamma$ -rays mostly hit only one wire.

The following procedures were applied for the reconstruction of each wire-plane position where the charged particle passed through in VDCs as reported in Ref. [87].

- A cluster had at least two hit wires. A single hit wire is not considered as a cluster and ignored.
- If there existed more than two hit wires in a single cluster, the hit wire of the shortest drift time was ignored. This is because the uniformity of the electric field was distorted near the sense wire.

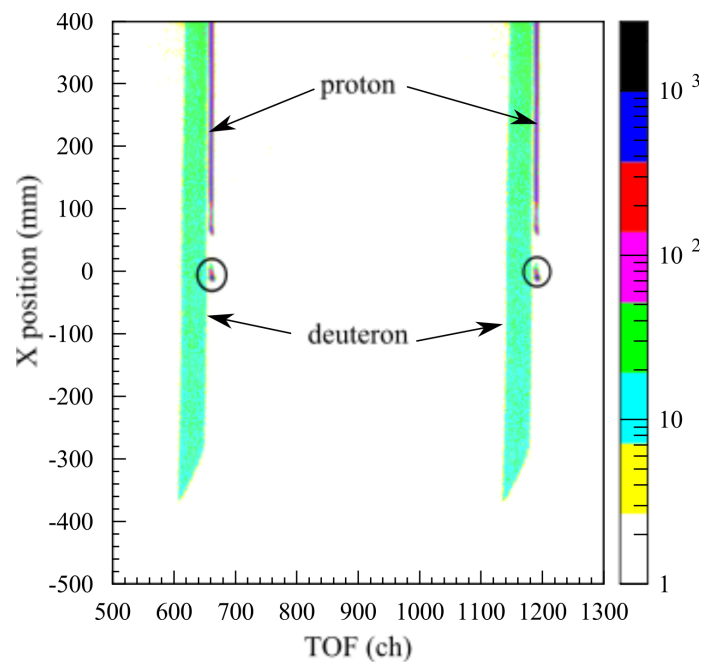


Figure 3.6: Colors plot of the X position at the focal plane versus TOF. Elastically scattered protons can be clearly identified as shown in the area surrounded by the solid circle.

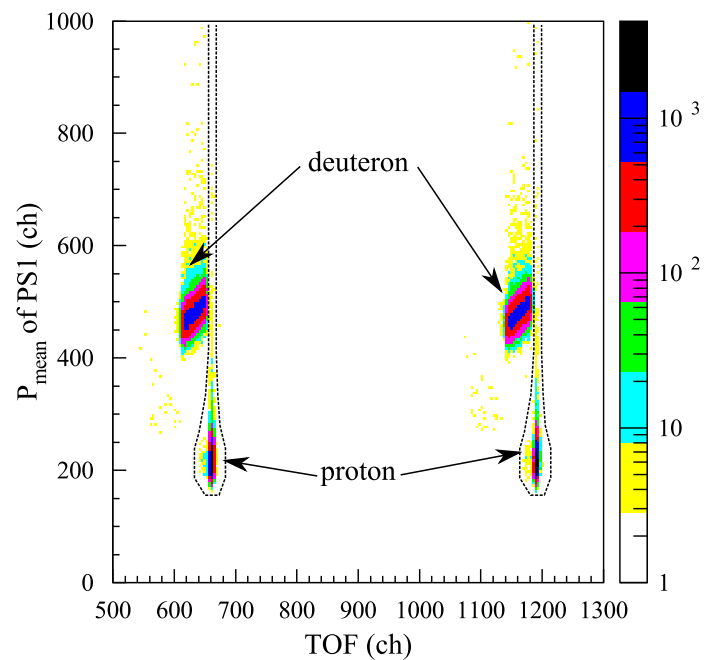


Figure 3.7: Colors plot of  $\bar{P}$  versus TOF of PS1 for PID.

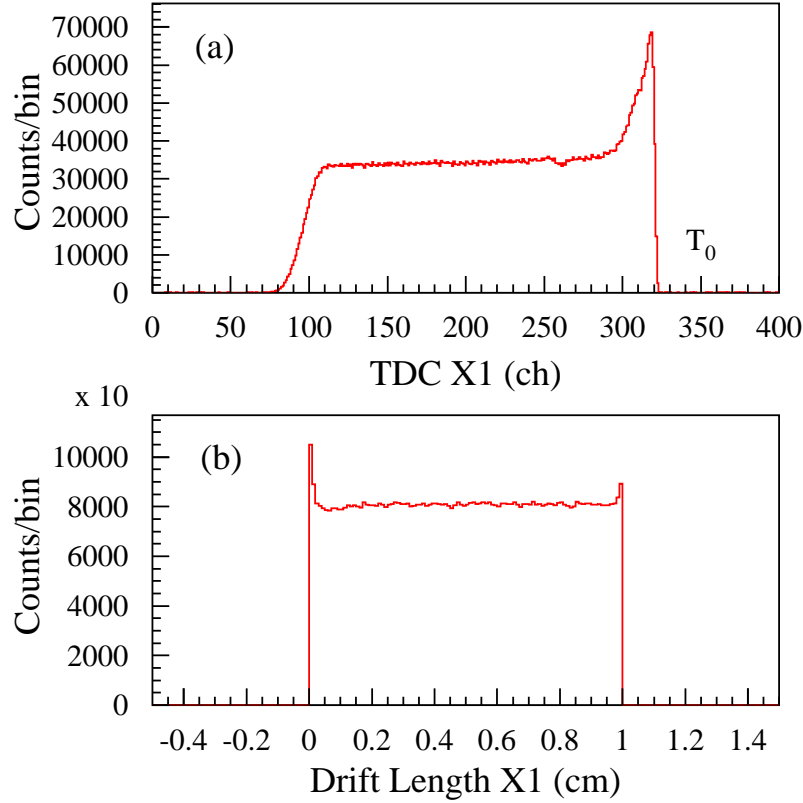


Figure 3.8: (a) TDC spectrum on X1 plane obtained from LeCroy 3377. (b) Drift length (cm) converted from TDC spectrum (a) by using so-called  $x-t$  relation.

- The intercept position and angle for each cluster were calculated by a least-square method.

The position and angle of a trajectory at each wire plane is calculated by a least-square fitting of the drift lengths of the hit wires in one cluster. The trajectory is uniquely determined by combining the deduced positions at four wire planes. The residual position resolution for each plane was about  $300 \mu\text{m}$  in full width at half maximum (FWHM). It corresponds to the energy resolution of about 10 keV at  $E_p = 295 \text{ MeV}$ , which is much smaller than the energy spread of the beam ( $\geq 100 \text{ keV}$  in FWHM). Figure 3.8 shows the typical TDC spectrum (drift time) and the converted drift length.

If more than one clusters existed in the X1(U1) and/or X2(U2) plane, the consistency among the angles was checked for all the possible combinations by  $\chi$  square method. In addition, If there were more than one good track (multi-track event), this event is ignored because we could not judge whether each track is true or not. However, the number of multi-track event is less than 1 % and neglected here. This multi-cluster treatment is effective for

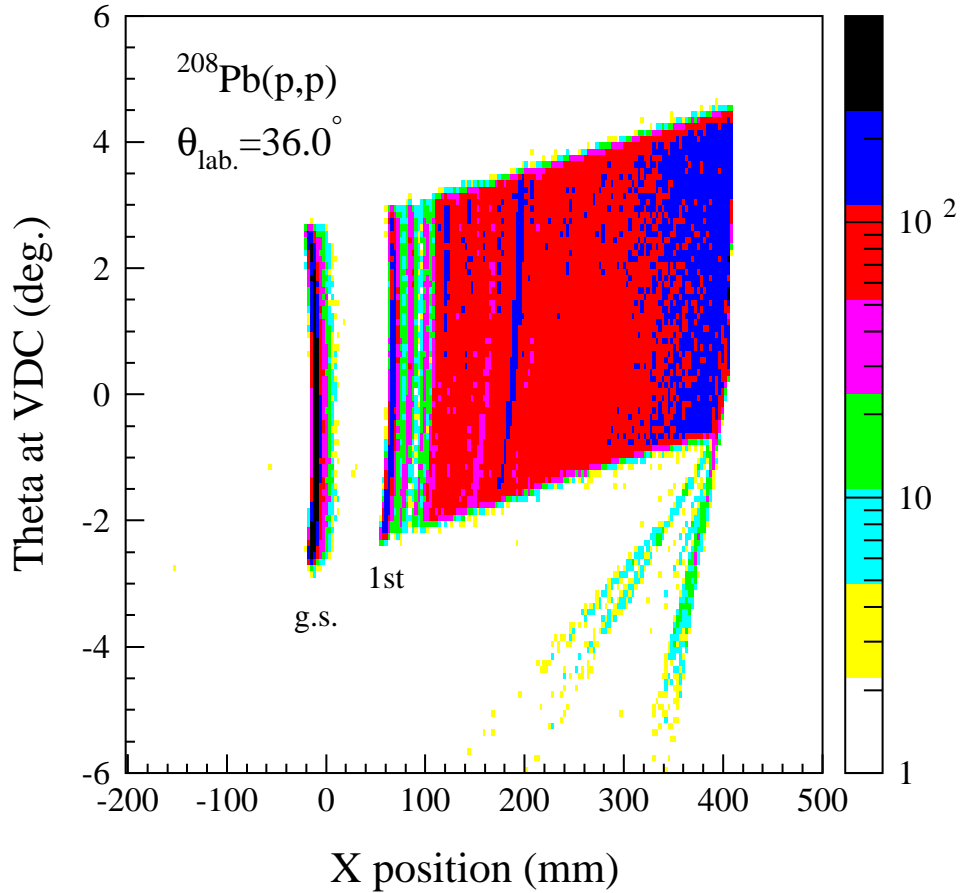


Figure 3.9:  $\theta$  versus  $X$  plot at the focal plane of the spectrometer reconstructed from the VDCs data in the case of  $^{208}\text{Pb}$  at  $\theta_{lab.} = 36.0^\circ$ .

avoiding severe reduction of the yields and efficiencies of VDCs especially at the scattering angles where the background events are relatively large. The yield ratios of single-cluster over multi-cluster events are about 80 ~ 95 %.

After the reconstruction of the trajectories of the scattered particles, the position and angle spectra at the focal plane were obtained as shown in Fig. 3.9. Figure 3.10 shows the typical position spectra of the four target nuclei at  $\theta_{lab.} = 36^\circ$ . Elastically scattered proton events can be distinguished from other inelastic events which represent excited states of each target nucleus. Finally their yields for  $^{204,206,208}\text{Pb}$  and  $^{58}\text{Ni}$  targets were counted within the  $3\sigma$  region of the elastic peaks in Fig. 3.10.

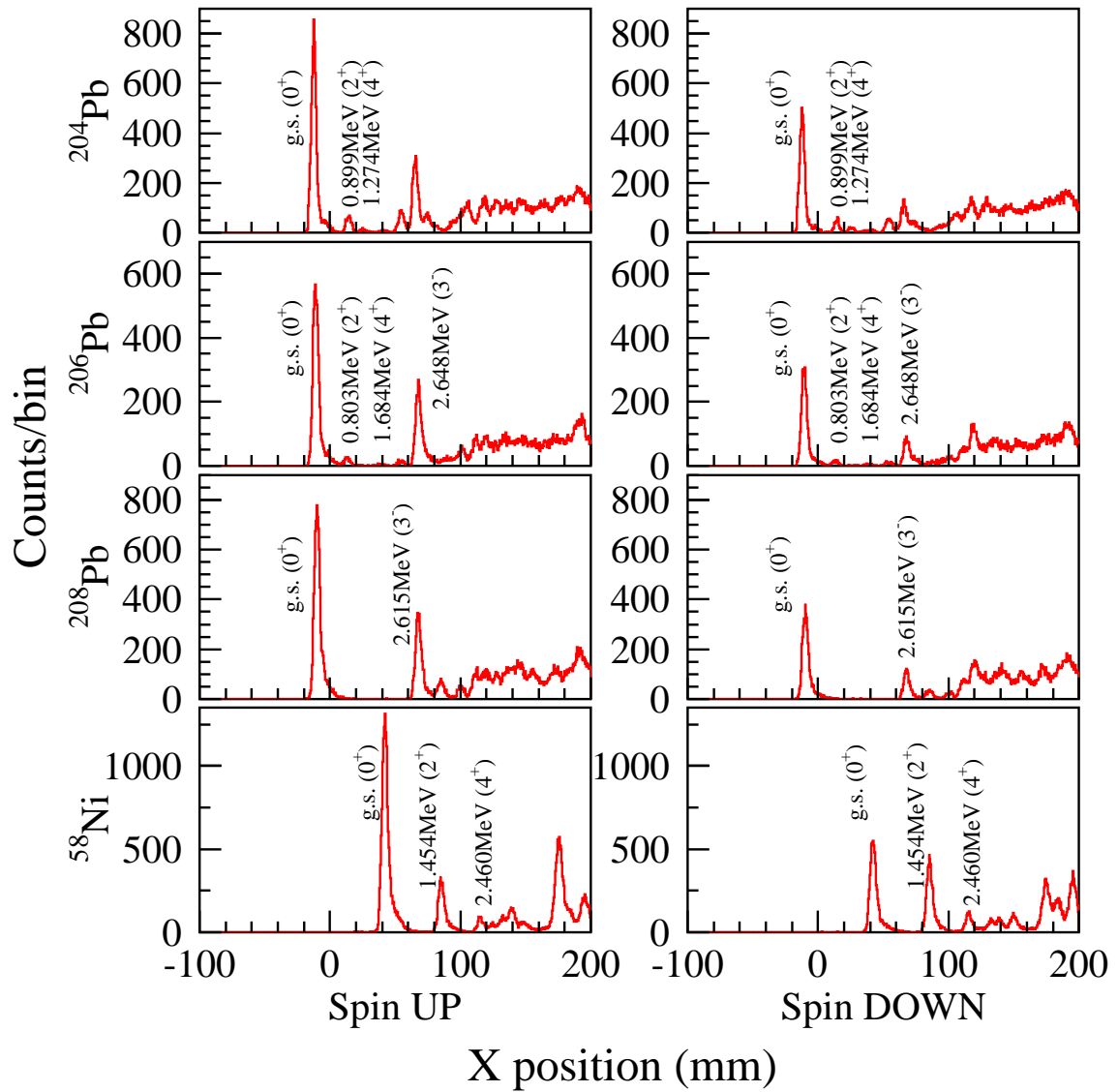


Figure 3.10: Typical position spectra for proton elastic scattering from  $^{204,206,208}\text{Pb}$  and  $^{58}\text{Ni}$  at  $\theta_{lab.} = 36.0^\circ$ . Elastic events (g. s. ( $0^+$ )) can be distinguished from other excited states in each spectrum.

### 3.3.2 Tracking efficiency

The tracking efficiencies of each plane of VDCs was estimated as follows:

$$\epsilon_{X1} = \frac{N_{X1 \cap U1 \cap X2 \cap U2}}{N_{U1 \cap X2 \cap U2}}, \quad (3.13)$$

$$\epsilon_{U1} = \frac{N_{X1 \cap U1 \cap X2 \cap U2}}{N_{X1 \cap X2 \cap U2}}, \quad (3.14)$$

$$\epsilon_{X2} = \frac{N_{X1 \cap U1 \cap X2 \cap U2}}{N_{X1 \cap U1 \cap U2}}, \quad (3.15)$$

$$\epsilon_{U2} = \frac{N_{X1 \cap U1 \cap X2 \cap U2}}{N_{X1 \cap U1 \cap X2}}, \quad (3.16)$$

where  $N_{X1 \cap U1 \cap X2 \cap U2}$  denotes the number of events in which the cluster positions can be determined for all planes, while  $N_{U1 \cap X2 \cap U2}$ , for example, denotes the number of three planes except for X1 plane. The total tracking efficiency for the elastic events is estimated by multiplying the efficiencies of all the four planes:

$$\epsilon_{\text{total}} = \epsilon_{X1} \epsilon_{U1} \epsilon_{X2} \epsilon_{U2}. \quad (3.17)$$

The obtained efficiencies were about 95 ~ 98% per plane. Thus the total efficiencies  $\epsilon_{\text{total}}$  were about 86 ~ 92%. The efficiencies gradually decreased as the scattering angle become large. This is because at the backward angles the rate and yield of the background events is getting large compared to the elastic events, and thereby the inefficient moment, when the electric field is effectively lowered, becomes large. If the mulcti-cluster treatments were not performed, the efficiency of each plane would get down to ~ 90% because of the high amount of the background events.

It should be noted that even if one analyzes only single cluster events for the track reconstruction, in order to calculate the efficiency for each plane by using Eqs. (3.13)–(3.16) one must use all the events including multi-cluster events for the denominators of Eqs. (3.13)–(3.16). Otherwise, the efficiency is misestimated and seems to be much higher than it should be especially where the background events relatively increase and make the multi-cluster events.

This is mainly caused by the strong correlations of the background events among four planes. Now we think about the case of the X1 plane efficiency, for example. In case of no correlation between four planes, from Eq. (3.13), the tracking efficiency  $\epsilon_{X1}$  for the single-cluster events is written as

$$\epsilon_{X1} = \frac{\prod_{i=1}^4 \epsilon_i (1 - m_i) Y}{\prod_{i=2}^4 \epsilon_i (1 - m_i) Y} = \epsilon_1 (1 - m_1), \quad (3.18)$$

where  $\epsilon_i$ ,  $m_i$ , and  $Y$  are the intrinsic efficiency against elastically scattered protons for each plane, the probability of making multi-cluster for each plane, and the real yield, respectively.

However, if there existed correlations between four planes, the  $\epsilon_{X1}$  is

$$\epsilon_{X1} = \frac{\left(\prod_{i=1}^4 \epsilon_i\right) (1 - m) Y}{\left(\prod_{i=2}^4 \epsilon_i\right) (1 - m) Y} = \epsilon_1. \quad (3.19)$$

Here, for simplicity, it is assumed that all four planes are simultaneously correlated with one another and thus the probability of detecting multi-cluster events is  $m$ . The two equations above shows that the existence of the correlations causes the overestimation of the efficiencies of single-cluster tracks.

Indeed, it is found that there exists the correlations among four planes and the efficiencies calculated by Eqs. (3.13)–(3.16) are little different between the single- and multi-cluster analyses. Besides, the yield reconstructed by single-cluster analysis is, of course, smaller than by multi-cluster analysis. Therefore, when one uses such an overestimated efficiency, the cross sections finally obtained are doubly underestimated. It is known that this estimation causes about 5 ~ 20 % decrease of the cross sections depending on the scattering angles. The previously measured data for  $^{58}\text{Ni}$  in Ref. [69] used only single cluster events to estimate the VDCs efficiencies. This is one of the reasons that we newly measured the data for  $^{58}\text{Ni}$  as well as lead isotopes.

### 3.4 Differential cross sections and analyzing powers

Elastically scattered proton events for each target nucleus can be chosen from the position spectrum of the focal plane as shown in Fig. 3.10. Yields of the elastic events for each spin direction of the beam ( $\uparrow$  and  $\downarrow$ ) are expressed as

$$Y^{\uparrow(\downarrow)} = \frac{d\sigma}{d\Omega} \left(1 + p_y^{\uparrow(\downarrow)} A_y\right) N_t N_b^{\uparrow(\downarrow)} l^{\uparrow(\downarrow)} \epsilon^{\uparrow(\downarrow)} \Delta\Omega_{\text{GR}}, \quad (3.20)$$

where  $p_y$ ,  $N_t$ ,  $N_b$ ,  $l$ ,  $\epsilon$ , and  $\Delta\Omega_{\text{GR}}$  are the  $y$  component of the beam polarization, number of target nuclei in unit area, number of protons in the beam, live-time ratio of the DAQ system, total detector efficiency, and solid angle of the Grand Raiden spectrometer, respectively. The number of proton in the beam  $N_b$  was derived from the collected charge by each Faraday Cup and the collection efficiency of the SCFC as mentioned in Sec. 3.1.2. The total efficiency  $\epsilon$  was determined by the product of the total efficiency of the VDCs and the trigger efficiency of PS1 and PS2 for protons at 295 MeV. The absolute trigger efficiency of PS1 and PS2 has been also measured in a separate experiment recently as written in Ref. [71]. The solid angle  $\Delta\Omega_{\text{GR}}$  was defined by the slit of  $\pm 20$  mrad wide and  $\pm 30$  mrad high which was located at the entrance of the Grand Raiden spectrometer.

Therefore, differential cross sections  $d\sigma/d\Omega$  and analyzing powers  $A_y$  at each scattering angle are derived from Eq. (3.20) as follows:

$$\frac{d\sigma}{d\Omega} = \frac{1}{p_y^{\uparrow} - p_y^{\downarrow}} \left( \frac{Y^{\downarrow} p_y^{\uparrow}}{N_b^{\downarrow} \epsilon^{\downarrow} l^{\downarrow}} - \frac{Y^{\uparrow} p_y^{\downarrow}}{N_b^{\uparrow} \epsilon^{\uparrow} l^{\uparrow}} \right) \frac{1}{N_t \Delta\Omega_{\text{GR}}}, \quad (3.21)$$

$$A_y = \frac{1 - \alpha}{\alpha p_y^{\uparrow} - p_y^{\downarrow}}, \quad (3.22)$$

$$\alpha = \frac{Y^{\downarrow}}{N_b^{\downarrow} \epsilon^{\downarrow} l^{\downarrow}} \bigg/ \frac{Y^{\uparrow}}{N_b^{\uparrow} \epsilon^{\uparrow} l^{\uparrow}}. \quad (3.23)$$

Note that  $p_y^\downarrow$  is a negative value, thus  $d\sigma/d\Omega$  becomes positive definite. Statistical errors of cross sections and analyzing powers ( $\Delta(d\sigma/d\Omega)$  and  $\Delta A_y$ ) are estimated by the simple way of the propagation of uncertainty and described as

$$\begin{aligned} \Delta\left(\frac{d\sigma}{d\Omega}\right) &= \frac{d\sigma}{d\Omega} \cdot \frac{1}{p_y^\uparrow - p_y^\downarrow} \cdot \frac{1}{\alpha p_y^\uparrow - p_y^\downarrow} \\ &\times \left\{ (1 - \alpha)^2 \left[ (p_y^\downarrow \Delta p_y^\uparrow)^2 + (p_y^\uparrow \Delta p_y^\downarrow)^2 \right] \right. \\ &\left. + (p_y^\uparrow - p_y^\downarrow)^2 \left( \frac{p_y^{\downarrow 2}}{Y^\uparrow} + \frac{\alpha^2 p_y^{\uparrow 2}}{Y^\downarrow} \right) \right\}^{1/2}, \end{aligned} \quad (3.24)$$

$$\begin{aligned} \Delta A_y &= \frac{1}{(\alpha p_y^\uparrow - p_y^\downarrow)^2} \left\{ (1 - \alpha)^2 (\alpha^2 \Delta p_y^{\uparrow 2} + \Delta p_y^{\downarrow 2}) \right. \\ &\left. + \alpha^2 (p_y^\uparrow - p_y^\downarrow)^2 \left( \frac{1}{Y^\uparrow} + \frac{1}{Y^\downarrow} \right) \right\}^{1/2}. \end{aligned} \quad (3.25)$$

The uncertainties of the counting statistics ( $1/\sqrt{Y}$ ) are so small that the statistical errors are mainly determined by the uncertainty of the polarization ( $p_y \sim 0.75(4)$  determined from BLP data) especially for the analyzing powers. The statistical errors are typically about  $1 \sim 2\%$ .

The systematic errors of this measurement mainly consist of the uncertainties of the beam instability and the target thicknesses, and these are about  $1\%$  respectively. The ambiguity of the incident angle is the main component of the beam instability which affects the scattering observables for heavy nuclei such as lead isotopes. This uncertainty was estimated from the change of the cross sections when the the scattering angles change with  $\pm 0.02^\circ$ , which were calculated by the RIA calculation. <sup>a</sup>

Therefore, the systematic errors account for a main part of the uncertainties of this experimental data. The error of  $N_b$  was due to the error of the charge collection efficiency as written in Sec. 3.1.2. In this data reduction this error was added to the systematic errors, not to the statistical errors described above. We totally estimated the the systematic errors as  $\pm 3\%$  of the obtained data. Therefore the experimental uncertainties are finally obtained by adding the  $\pm 3\%$  systematic errors to the statistical errors calculated from Eq. (3.24) and (3.25)

Compared to previous measurements at RCNP as performed in Ref. [69] and [70], there are several improvements in both the measurement and data reduction which are already mentioned above. Thus newly obtained data is systematically improved and especially the data set of cross sections for  $^{58}\text{Ni}$  is around  $10 \sim 15\%$  larger than the previous set used in Ref. [69] and [70]. Although the previous data cannot be compared directly with the new data since the con-

<sup>a</sup> As mentioned in Chap. 2.1, we monitored the beam positions to keep the beam conditions stable after each measurement. That means that we did not recognize the short-term and real-time stability of the beam just as the measurement is running. The BLP data in Figs. 3.1 and 3.2 partly shows the instabilities of the beam conditions during the measurement. Thus, we estimated the uncertainty from the beam angle a little bit larger than the simply calculated from the angular range of  $\theta_{lab.} \pm 0.02^\circ$ . For more sophisticated measurement with small uncertainty of the beam conditions, we need new instruments for nondestructive monitoring of the real-time beam position with an accuracy of less than 1 mm.

ditions of the measurements are different from each other, we summarize these improvements and the effects on the cross section data:

- Monitoring the beam condition by beam line viewers after each run. (keep the variation of the cross section due to the angular fluctuation about  $\pm 1$  %.)
- Particle identification using dE-TOF information. (increase of  $\geq 1$  %: see in Ref. [71])
- Multi-cluster treatments for the VDCs data reduction. (increase of 5 ~ 20 % if one used Eqs. (3.13)–(3.16) to estimate the tracking efficiencies.)
- Calibrations of absolute efficiencies of the trigger scintillators and absolute collection efficiencies of the SCFC by a separate experiment in Ref. [71]. (increase of  $\sim 2.0$  % and 1.5 %, respectively )

Data sets of angular distributions of differential cross sections and analyzing powers for polarized proton elastic scattering from  $^{58}\text{Ni}$  and  $^{204,206,208}\text{Pb}$  were obtained over an angular range of  $7^\circ < \theta < 50^\circ$ , corresponding to a range of momentum transfer from  $0.55 \text{ fm}^{-1}$  to  $3.5 \text{ fm}^{-1}$ . The digital data are listed in Appendix A. In the next chapter the analysis method to extract the neutron density distributions in lead isotopes via the experimental data of proton elastic scattering are given.



# Chapter 4

## ANALYSIS

In this chapter, we report our analysis method and results of the neutron density distributions extracted from the experimental data of proton elastic scattering from  $^{204,206,208}\text{Pb}$ .

The analysis method is based on the framework of the relativistic impulse approximation (RIA) using the relativistic Love-Franey (RLF)  $NN$  interaction [88] proposed by Murdock and Horowitz (MH model) [89, 90].

### 4.1 Relativistic impulse approximation

In the MH model the nucleon–nucleus optical potential is calculated by folding the RLF  $NN$  interaction with the nucleon vector and scalar density of the target nucleus. The RLF  $NN$  interaction is based on the Lorentz invariant  $NN$  scattering amplitude of

$$\begin{aligned} \mathcal{F} = & \mathcal{F}^S + \mathcal{F}^V \gamma_{(0)}^\mu \gamma_{(1)\mu} + \mathcal{F}^{PS} \gamma_{(0)}^5 \gamma_{(1)}^5 \\ & + \mathcal{F}^T \sigma_{(0)}^{\mu\nu} \sigma_{(1)\mu\nu} + \mathcal{F}^A \gamma_{(0)}^5 \gamma_{(0)}^\mu \gamma_{(1)}^5 \gamma_{(1)\mu}, \end{aligned} \quad (4.1)$$

where  $\mathcal{F}^S$ ,  $\mathcal{F}^V$ ,  $\mathcal{F}^{PS}$ ,  $\mathcal{F}^T$ , and  $\mathcal{F}^A$  denote the scalar, vector, tensor, pseudoscalar, and axial vector amplitudes, and the subscripts (0) and (1) represent the incident and recoil nucleon, respectively. For a spin-zero spherical nucleus, only the scalar and the zeroth-component of the vector amplitudes are dominant contribution to the optical potential. The details of the RIA calculations by MH model are mentioned in Appendix B.

Figure 4.1 shows the obtained experimental data of cross sections and analyzing powers for elastic scattering from  $^{204,206,208}\text{Pb}$ , and  $^{58}\text{Ni}$  compared with two kinds of model calculations. The solid and dashed lines are the RIA calculations [89, 90] with Dirac–Hartree (DH) [17] densities of the target nuclei, and the calculations using the recent global Dirac optical model by Cooper, Hama and Clark [91], respectively. Although both calculations well reproduce the analyzing powers, only the global Dirac optical model is in good agreement with the cross sections. The MH model poorly reproduces the angular distributions of the cross section especially at backward angles. This is because neither the RLF interaction nor the nucleon densities used in the MH model are realistic. However, even though a realistic nucleon density

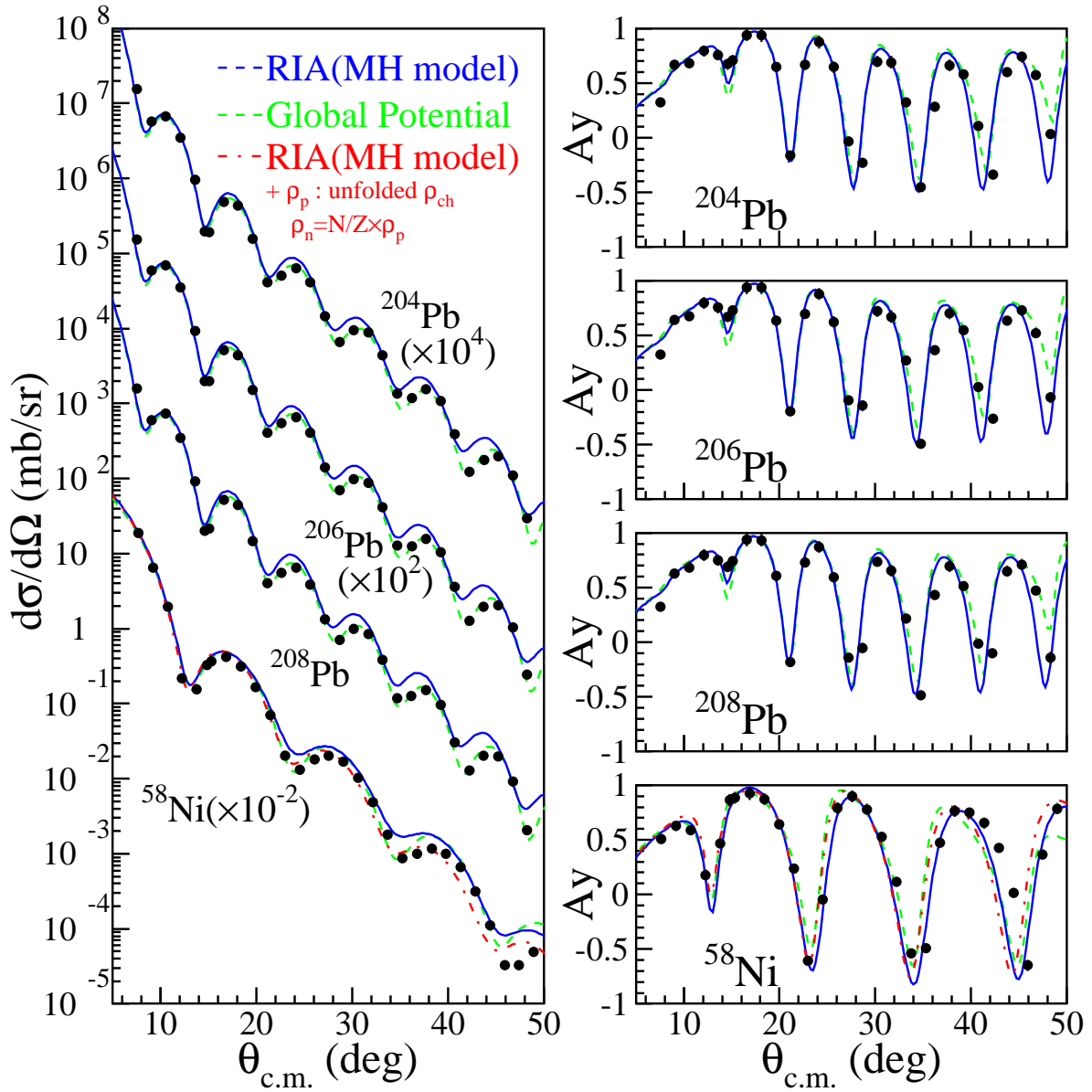


Figure 4.1: Obtained data of differential cross sections and analyzing powers for elastic scattering from  $^{58}\text{Ni}$  and  $^{204,206,208}\text{Pb}$  at  $E_p = 295$  MeV, whereas the lines are due to Murdock and Horowitz (solid) [89, 90] and the global Dirac optical potential (dashed) [91]. The dash-dotted lines show the MH model calculations for  $^{58}\text{Ni}$  with the realistic nucleon density by an unfolding charge density.

of  $^{58}\text{Ni}$ , as mentioned in the next subsection, was used in place of the DH density for the MH calculation (dash-dotted lines in Fig. 4.1), the disagreement with the experimental data of  $^{58}\text{Ni}$  still remains. In order to explain the experimental data we need the effective  $NN$  interaction inside the nuclear medium in place of the RLF interaction.

### 4.1.1 Realistic point proton density distributions

A realistic point proton density distribution was determined by unfolding the nuclear charge distribution extracted from electron elastic scattering [54, 55, 92–94] with the intrinsic charge distributions of the proton and neutron. Using the Fourier transform of the radial density  $\tilde{\rho}(q) = \mathcal{F}\{\rho(r)\}$  where  $q$  is the momentum transfer, the relationship between the charge, proton, neutron, intrinsic proton-charge, and intrinsic neutron-charge densities  $\rho_{ch}$ ,  $\rho_p$ ,  $\rho_n$ ,  $\rho_{ch}^p$ ,  $\rho_{ch}^n$  is approximately described as

$$\begin{aligned}\tilde{\rho}_{ch}(q) &\simeq \tilde{\rho}_p(q)\tilde{\rho}_{ch}^p(q) + \tilde{\rho}_n(q)\tilde{\rho}_{ch}^n(q) \\ &\simeq \tilde{\rho}_p(q)G_E^p(q^2) + \tilde{\rho}_n(q)G_E^n(q^2),\end{aligned}\quad (4.2)$$

where in the non-relativistic limit,  $\tilde{\rho}_{ch}^{p(n)} \simeq G_E^{p(n)}(q^2)$  which is the experimentally determined Sachs electric form factor in proton (neutron). The correction term by the spin–orbit and relativistic effects on the Sachs form factors in the Breit frame, the so-called Darwin–Foldy correction, are negligible because their effects on the nuclear size are one order smaller than the neutron-charge radius and comparable with the error of charge radius as shown in Refs. [58, 95].

For the nuclear charge distributions of  $^{204,206,208}\text{Pb}$  and  $^{56}\text{Ni}$ , we used the parameter sets of the model-independent analyses of electron scattering and/or muonic X-ray data as listed in Ref. [54]. The Sum-of-Gaussians (SOG) expansion were used for  $^{206,208}\text{Pb}$ ,  $^{56}\text{Ni}$ , whereas the Fourier-Bessel (FB) series expansion for  $^{204}\text{Pb}$ . The model-independent analyses in the form of SOG and FB have been originally developed by Sick [92], and Friar and Negele [94, 96], respectively.

For the intrinsic nucleon charge form factor  $\tilde{\rho}_{ch}^{p(n)}$ , we adopted a new set of nucleon electromagnetic form factors which have been recently extracted from the reanalysis of the *world e-p* and *e-d* scattering data at low-momentum transfers from 0.3 to 1  $\text{GeV}^2/c^2$  where the nucleon charge form factor is very sensitive to its model-independent charge radius [97–100]. The proton-charge radius of 0.895(18) fm obtained from  $\tilde{\rho}_{ch}^p$  in Refs. [97–99] is much larger than the value of 0.863(4) fm used in the previous work [101], but is consistent with the value of 0.883(14) fm obtained from the recent measurement of the hydrogen 1S Lamb shift [102].<sup>a b</sup>

In order to know the neutron density distribution, not only the nucleon-charge radius but also its density is required because the realistic point proton distribution is derived from nucleus- and nucleon-charge density. In this work we adopted the parameterization of nucleon charge distribution reported in Ref. [99], which can reproduce the model-independent

<sup>a</sup> Compared to the new analysis of elastic *e-p* scattering data, the previous analyses [101, 103] did not include various higher-order corrections at both low and high momentum transfers such as the Darwin-Foldy term, Coulomb distortion, etc. [104–106], while the analyses of the atomic Lamb shift measurements have developed including various QED corrections. Thus the previously extracted nucleon form factors are rather model-dependent and can not give the intrinsic charge radii which should be compared with the Lamb shift results.

<sup>b</sup> It should be noted, however, that the very recent measurement of the muonic-hydrogen Lamb shift has resulted in  $r_{ch}^p = 0.84184(67)$  fm with a remarkable accuracy of 0.08% [107]. This new value is very inconsistent with, and  $5\sigma$  smaller than the ones mentioned above. The origin of this large discrepancy is not understood at this time and requires further validation of this measurement and the QED effects on muonic-hydrogen atoms.

nucleon charge radius. The procedure of unfolding method follows the same way as mentioned in Ref. [70]. Figure 4.2 shows the extracted proton density distributions of  $^{58}\text{Ni}$  and  $^{204,206,208}\text{Pb}$  (solid lines) by unfolding method. Compared to the theoretical DH calculations (blue dotted lines), the extracted distributions show the gradual change of density as a function of radius and particularly the slopes of the surface diffusenesses are relatively small. On the contrary, the Hartree–Fock–Bogolyubov calculations with several Skyrme interactions (green lines) have more gradual slopes than the extracted proton densities.

In the case of  $^{58}\text{Ni}$ , the neutron rms radius is expected to be almost the same as the proton rms radius as mentioned later. Therefore we assumed that the neutron density of  $^{58}\text{Ni}$  has the same shape as the proton density, that is,  $\rho_n = (N/Z)\rho_p$ .

### 4.1.2 Scalar and Vector density distributions

For the RIA calculations, scalar density distributions are necessary as well as baryon density distributions. While the vector density is normalized to the mass number by baryon number conservation, there is no analogous normalization condition for the scalar density. Scalar density distributions can not be extracted directly, unless the wave functions of the ground state are known in advance by solving the field equations for the scalar meson. In the relativistic mean field theory [108], however, the scalar density  $\rho^S$  is approximated in the form of the vector density  $\rho^V$  as follows:

$$\rho^S(r) \approx \left\{ 1 - \frac{3}{10} \frac{k_F^2}{M^{*2}} \right\} \rho^V(r), \quad (4.3)$$

where  $k_F$  and  $M^*$  are the local Fermi momentum and the effective mass, respectively. The density ratio of  $\rho^S/\rho^V$  derived from Eq. (4.3) is usually about 0.93 at the saturation ( $k_F \simeq 1.30 \text{ fm}^{-1}$  and  $M^* \simeq 0.6M$ ), but around the surface of nuclei the ratio gradually approaches one. According to the DH calculations for heavy nuclei the volume integral of the ratios are almost constant at 0.96, as reported in Refs. [69, 70]. Therefore, we simply assumed a scalar density  $\rho^S$  of  $\rho^S = 0.96\rho^V$  for a vector density  $\rho^V$  using the realistic nucleon density.

The effect of the negative-energy states in the filled "Dirac sea", namely, the vacuum polarization on the scalar density was reported in Ref. [109] and causes 10% reduction of the scalar density in the nuclear center. In this work we did not deal with the effect explicitly, but it may be included somewhat by the density-dependent modification of the effective  $NN$  interaction as written in the next section.

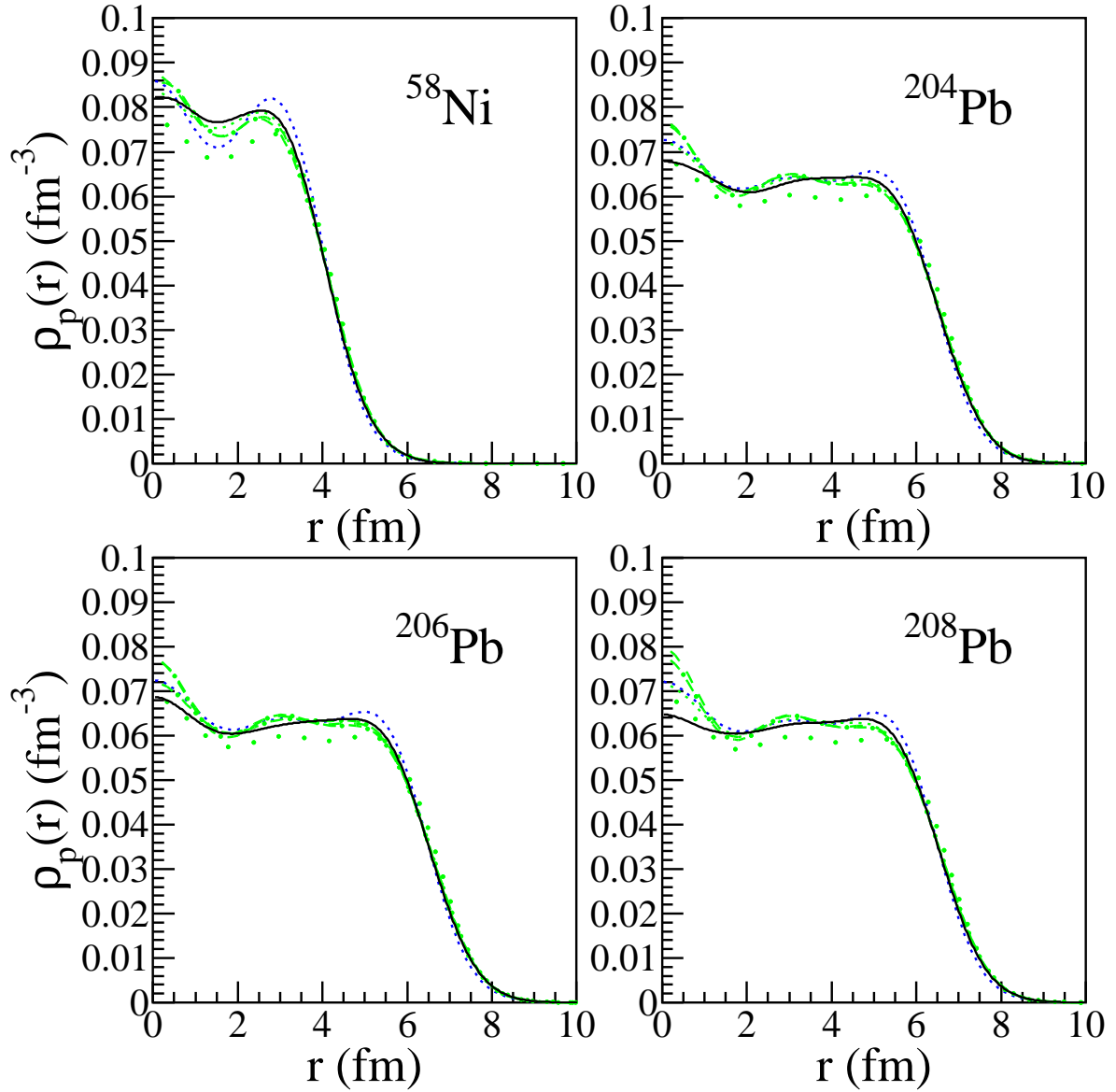


Figure 4.2: Proton density distributions of  $^{58}\text{Ni}$  and  $^{204,206,208}\text{Pb}$  by unfolding charge distributions with the new parameter sets of nucleon charge form factor (solid lines). The blue dotted lines are due to the DH calculations for comparison, while the green long-dotted, short-dotted, dashed, and dash-dotted lines are due to Skyrme-Hartree-Fock-Bogolyubov calculations with SIII, SKM\*, SKP, and SLY4 parametrizations, respectively.

## 4.2 Medium modification of $NN$ interaction

The RLF interaction in the MH model is described by a set of five Lorentz covariant functions and was determined from the free  $NN$  phase shift analysis [88]. It was found that the Dirac optical potential folded by the free  $NN$  interaction can not fully reproduce the experimental data at high momentum transfers even using the realistic nucleon density. In order to explain the experimental data, we introduced a medium modification into the RLF  $NN$  scattering amplitudes by varying the coupling constants and masses of the  $\sigma$  and  $\omega$  mesons depending on the local density as follows:

$$g_j^2, \bar{g}_j^2 \rightarrow \frac{g_j^2}{1 + a_j \rho(r)/\rho_0}, \frac{\bar{g}_j^2}{1 + \bar{a}_j \rho(r)/\rho_0} \quad (4.4)$$

$$m_j, \bar{m}_j \rightarrow m_j \left[ 1 + b_j \frac{\rho(r)}{\rho_0} \right], \bar{m}_j \left[ 1 + \bar{b}_j \frac{\rho(r)}{\rho_0} \right] \quad (4.5)$$

$j = \sigma, \omega,$

where  $m_j, \bar{m}_j, g_j,$  and  $\bar{g}_j$  are the masses and coupling constants of  $\sigma$  and  $\omega$  mesons for real and imaginary amplitudes, respectively. The normal density  $\rho_0$  is  $0.1934 \text{ fm}^{-3}$ . In free space, where the density of the target nucleus is zero, the masses and coupling constants of the exchanged mesons are set to be the same as those of the free  $NN$  interaction, but inside the nucleus the modification is assumed to be proportional to the nucleon density  $\rho(r)$  with the phenomenological parameters  $a_j, \bar{a}_j, b_j,$  and  $\bar{b}_j$ . This density-dependence describes the first-order approximation in terms of the nuclear density and partially explains various many-body effects such as Pauli blocking<sup>c</sup>, vacuum polarization [109, 110], multi-step processes [111], and partial restoration of chiral symmetry [112]. This density-dependent correction has the analogous expression of the nuclear effective interaction in a nucleus reported by Nagata and co-workers in Ref. [113].

Since the modification has a universal form of local-density dependent terms, we can apply it to any other nuclei once the parameters are calibrated with a real nucleus. At the present stage we have used four parameters assuming the same modification for the real and imaginary parts of the  $NN$  scattering amplitude ( $a_j = \bar{a}_j, b_j = \bar{b}_j$ ) because with eight parameters there are so many degrees of freedom that these parameters have strong correlations with each other.

The extraction of the neutron densities of lead isotopes is based on the medium-modified RIA calculation with realistic proton densities. For this purpose we first need to determine the medium-modification of the effective RLF interaction. In the next subsection, we report the calibration of the medium-effect parameters using the experimental data of proton elastic scattering from  $^{58}\text{Ni}$ .

<sup>c</sup>Though in the MH model the correction of the Pauli blocking effect is introduced by modifying the optical potentials with a local-density approximation based on the Dirac-Brueckner calculation [89, 90], when using the medium-modified RIA we omit the Pauli blocking correction in the MH model. For the Pauli blocking correction we phenomenologically modified the  $NN$  interaction, not the optical potential.

### 4.3 Calibration of the medium effect parameters

For the calibration of the four medium-effect parameters,  $a_j$  and  $b_j$  ( $j = \sigma, \omega$ ), we have chosen  $p$ - $^{58}\text{Ni}$  elastic scattering because  $^{58}\text{Ni}$  is the heaviest spherical nucleus with  $N \approx Z$  and the neutron density of  $^{58}\text{Ni}$  is expected to have a similar distribution to the proton density ( $\rho_n = (N/Z)\rho_p$ ). Both the experimental and theoretical results [8, 13, 27, 58, 66, 114] support a neutron rms radius for  $^{58}\text{Ni}$  that is almost the same as the proton rms radius, while for  $N = Z$  nuclei, such as  $^{40}\text{Ca}$  or  $^{56}\text{Ni}$ , the proton rms radii are larger than the neutron rms radii due to Coulomb repulsion. Figure 4.3 and 4.4 is neutron-number dependence of neutron skin thicknesses for Ni isotopes by several relativistic and non-relativistic calculations, respectively, and shows that all the listed theoretical calculations also agree that the neutron skin thickness of  $^{58}\text{Ni}$  is almost zero. The realistic proton density of  $^{58}\text{Ni}$  is extracted by unfolding the charge density with the new intrinsic nucleon-charge density.

A fit to the  $^{58}\text{Ni}$  data of cross sections and analyzing powers obtained in this experiment and spin rotation parameters previously measured at the same energy [87] was carried out by  $\chi^2$  test [115] with the four medium-effect parameters. The value of  $\chi^2$  is given by

$$\chi^2 = \sum_{\theta_i} (y_{\theta_i}^{\text{exp}} - y_{\theta_i}^{\text{calc}})^2 / \Delta y_{\theta_i}^2, \quad (4.6)$$

where  $y_{\theta_i}^{\text{exp}}$ ,  $\Delta y_{\theta_i}$ , and  $y_{\theta_i}^{\text{calc}}$  are the  $i$ th experimental data, error, and medium-modified RIA calculation for  $^{58}\text{Ni}$  at each  $\theta_i$ . The best-fit parameters providing a minimum of  $\chi^2$  ( $\chi_{\min}^2$ ), are listed in Table 4.1. The solid line in Fig. 4.5 is the medium-modified RIA calculation with these best-fit parameters and the realistic nucleon densities deduced from the charge distribution. Compared to the previous work [70], the modifications by the best-fit parameters are very small. The best-fit calculations are in better agreement with the experimental data than the previous data even though the number and angular range of the data points is much larger than for the previous data [69, 70]. This means that the improvements to reduce the experimental systematic uncertainties work very well. The standard error of each best-fit parameter in Table 4.1 was determined from a contour corresponding to an increase of 1 in  $\chi^2$  from  $\chi_{\min}^2$  by allowing all the other parameters to vary freely to minimize  $\chi^2$  for each chosen value of the parameter.

Table 4.1: Best-fit medium-effect parameters  $a_j$  and  $b_j$  ( $j = \sigma, \omega$ ) in Eq. (4.4), (4.5).

$j$	$\sigma$	$\omega$
$a_j$	$-0.044 \pm 0.026$	$0.037 \pm 0.040$
$b_j$	$0.097 \pm 0.013$	$0.075 \pm 0.021$

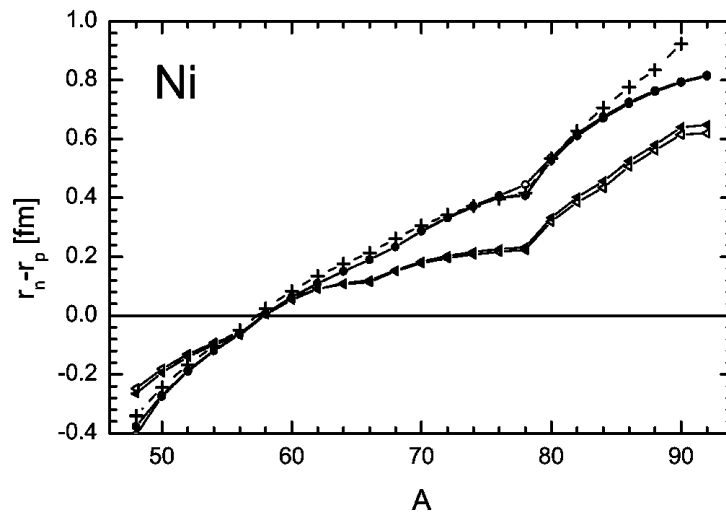


Figure 4.3: The neutron skin thicknesses for even-Ni isotopes calculated by DBHF with the Groningen (triangles) and Bonn A (circles) interactions, and RMF with the NL3 [19] parametrization. All of them shows that the neutron skin thickness of  $^{58}\text{Ni}$  is almost zero. Taken from Ref. [8].

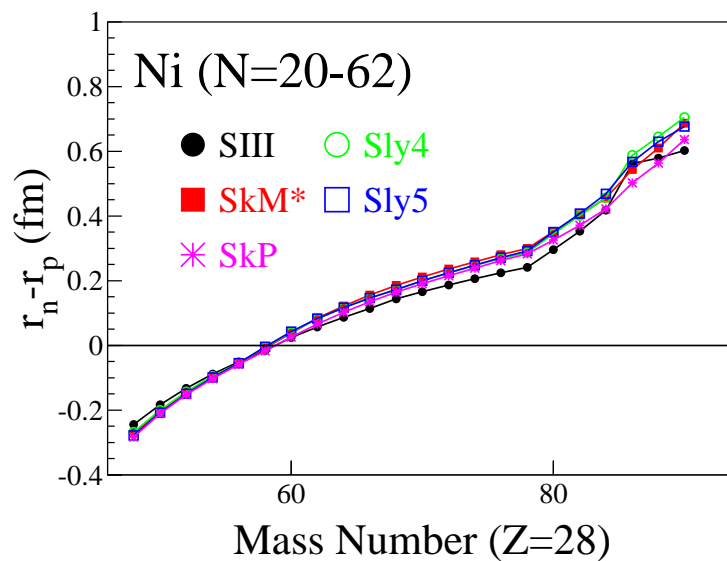


Figure 4.4: The neutron skin thicknesses for even-Ni isotopes calculated by Hartree–Fock–Bogolyubov (HFB) plus pairing corrections using five types of Skyrme forces, that is, SIII [116] (filled circles), SkM\* [9] (filled squares), SkP [10] (asterisks), Sly4 [11] (open circles), and SLy5 [11] (open squares) parameterizations. As is the case with relativistic models in Fig. 4.3 nonrelativistic models show that the neutron skin thickness of  $^{58}\text{Ni}$  is almost zero.

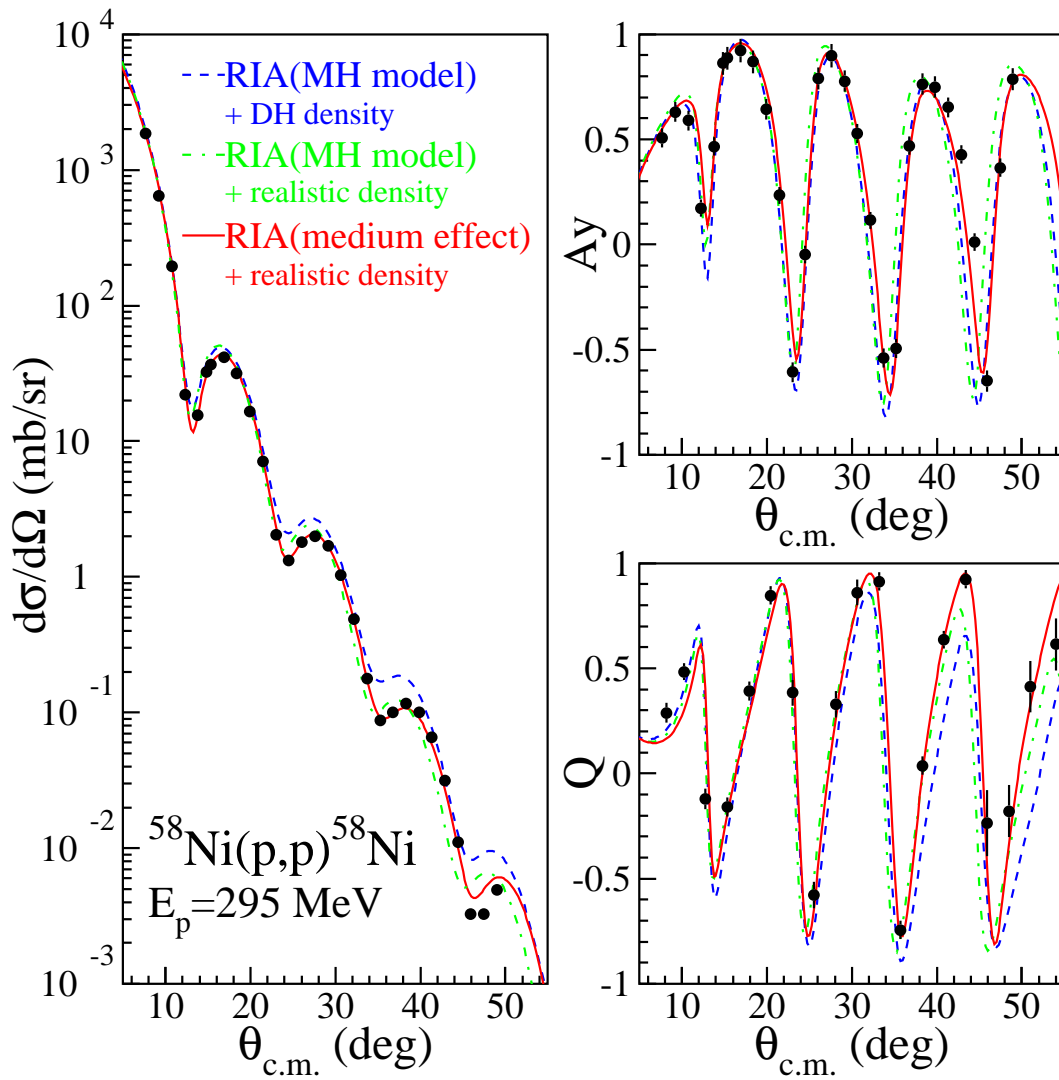


Figure 4.5: Calibration of medium-effect parameters by fitting to the experimental data for  $^{58}\text{Ni}$ . The solid line is the medium-modified RIA calculation with best-fit parameters. The dashed and dash-dotted lines are from the original MH model with DH and realistic nucleon densities.

## 4.4 Extraction of neutron density distributions

Using the effective  $NN$  interaction calibrated by  $^{58}\text{Ni}$  data we extracted the neutron density distributions of  $^{204,206,208}\text{Pb}$ . The realistic proton density distributions of lead isotopes were also used by unfolding charge distributions.

In order to find the best-fit neutron density distribution, we used a sum-of-Gaussian (SOG) function, which has been originally investigated in the model-independent analysis of charge distributions [54, 55]. The SOG neutron density is described as

$$\rho_n(r) = \frac{N}{2\pi^{3/2}\gamma^3} \sum_{i=1}^{12} \frac{Q_i}{1 + 2R_i^2/\gamma^2} \times (e^{-(r-R_i)^2/\gamma^2} + e^{-(r+R_i)^2/\gamma^2}), \quad (4.7)$$

where  $N$  and  $Q_i$  are the number of neutrons, and the fraction of  $N$  in the  $i$ th Gaussian with the normalization condition  $\sum_i Q_i = 1$ , respectively. For simplicity we fixed the width  $\gamma$  and position  $R_i$  of the  $i$ th Gaussian to the same values used for the charge distributions of  $^{208}\text{Pb}$  in Ref. [54] since the  $e^{-208}\text{Pb}$  elastic scattering data covers a wider range of momentum transfer from 0.44 to 3.7  $\text{fm}^{-1}$  than our data from 0.55 to 3.5  $\text{fm}^{-1}$ .

We searched for the best-fit values of  $Q_i$  by the  $\chi^2$  method. Figure 4.6 shows the results of the medium-modified RIA calculations with the best-fit neutron density distributions of  $^{204,206,208}\text{Pb}$  (solid lines). The medium-modified RIA calculations with the DH nucleon density (dash-dotted lines) well reproduce the analyzing powers and the angular positions of the diffraction peaks and minima compared with the original MH calculations (dashed lines), but still overestimate the absolute values of the cross sections. The best-fit calculations (solid lines) are in good agreement with the experimental data of both the cross sections and analyzing powers even in the high momentum transfer region up to 3.5  $\text{fm}^{-1}$ . It was found that the absolute values of the cross sections affect the nucleon density distributions quite directly. Thus when using the model-independent densities it is very important to determine the cross sections precisely. The typical reduced  $\chi_{\min}^2$ , namely  $\chi_{\min}^2/\nu$ , where  $\nu$  is the number of degrees of freedom, is about 4.

**Coulomb potential effect in lead isotopes** In the search for the best-fit parameters of the neutron densities, it was also found that the the Coulomb potentials, i.e., the charge radii of lead isotopes are sensitive to the scattering observables especially at high momentum transfers. For the calculation of the Coulomb potential the charge density of the target nucleus is assumed to be that of a uniformly charged sphere of radius  $r_0 A^{1/3}$  where  $r_0 = 1.25$  fm is usually known to be the reduced Coulomb radius. Where the radius is larger than  $R_0 = r_0 A^{1/3}$ , non-relativistic Coulomb wave functions are used. In the case of  $^{208}\text{Pb}$ , for example,  $r_0$  is about 1.20 fm, which reproduces experimentally determined value of the rms charge radius of  $^{208}\text{Pb}$ . If the reduced Coulomb radius  $r_0$  is changed by  $\pm 5\%$  ( $r_0 = 1.14, 1.26$  fm), the reduced  $\chi^2$  of the fitting with the experimental data increases by about  $\delta\chi^2/\nu = \pm 50/47 \sim \pm 1$ . This  $\chi^2$  increase is surprisingly larger than the value corresponding to 1 standard deviation (details are mentioned

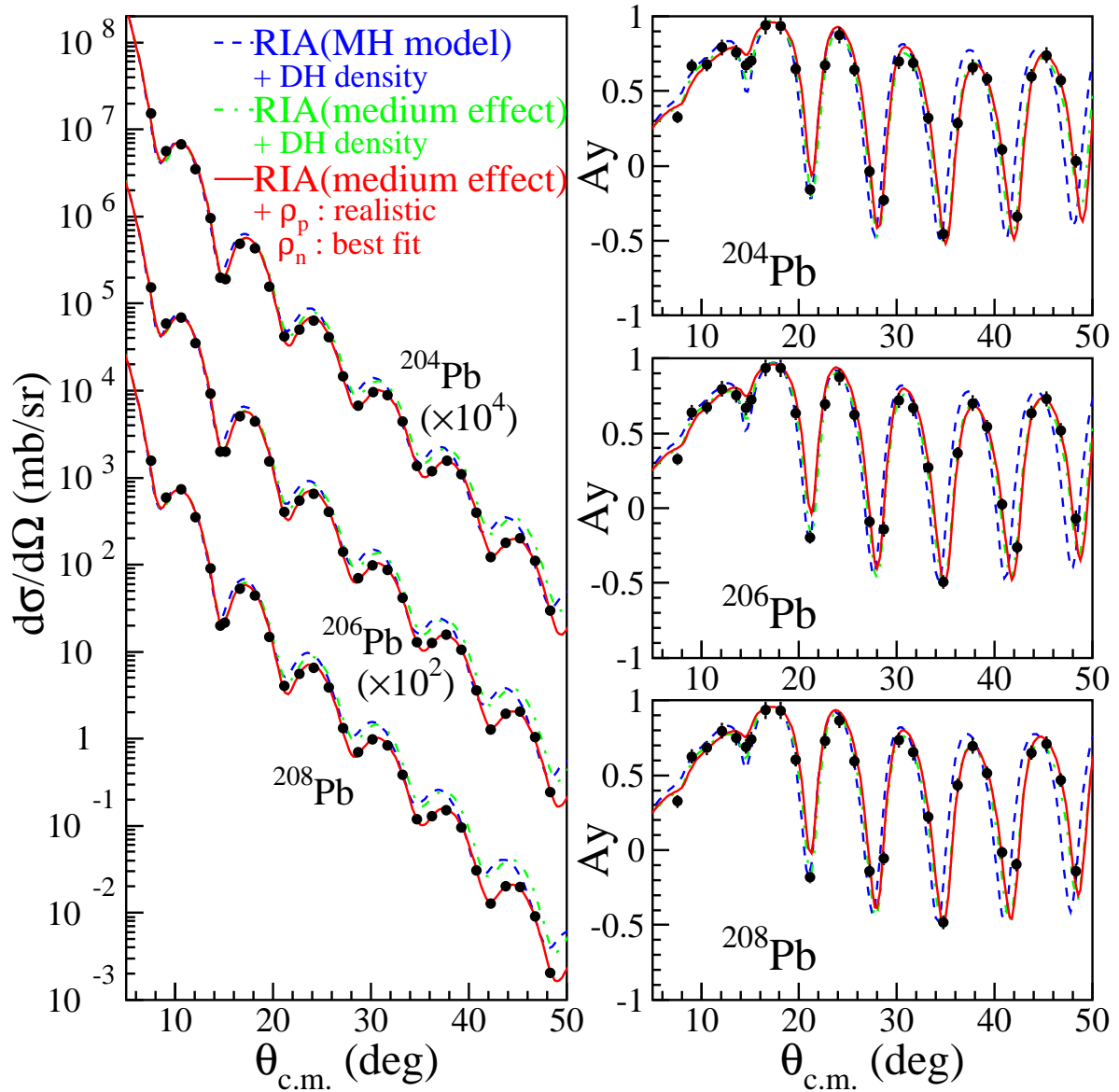


Figure 4.6: Best fit results for neutron density distributions in  $^{204,206,208}\text{Pb}$ , are shown as solid lines. The original MH and medium-modified RIA calculations with the DH nucleon density are also shown by dashed and dash-dotted lines.

in the next subsection) and shows that the precise measurement of the experimental data with small systematic uncertainties has been achieved to such an extent that the small change of Coulomb radius can be distinguished. The difference of the calculated observable between  $r_0 = 1.20$  fm and  $r_0 = 1.14, 1.26$  fm occurs almost at the backward angles ( $\theta_{lab.} > 30^\circ$ ), and hence arises from the change of the depth of the Coulomb potential rather than its radius due to the nuclear charge conservation. Therefore in the RIA calculations in this thesis we used the

adjusted values of the reduced Coulomb radii of target nuclei which reproduce the rms charge radii reported in Ref. [54, 56].

#### 4.4.1 Estimation of error-envelopes

**“Experimental uncertainties”** The standard error-envelopes of the neutron density distributions due to the experimental errors can be estimated by the increase  $\Delta\chi^2$  corresponding to 1 standard deviation from  $\chi_{\min}^2$ , expressed as the following inequality:

$$\chi^2 \leq \chi_{\min}^2 + \Delta\chi^2. \quad (4.8)$$

For the error-estimation of the neutron density we need to know the 1–standard deviation region encompassed by the joint variation of multi parameters.  $\Delta\chi^2$  for multi parameters obeys the  $\chi^2$  probability distribution function for  $m$  degrees of freedom, where  $m$  is the number of fitted parameters [115], and is roughly equal to  $m$  for 1 standard deviation ( $\Delta\chi^2 \approx m = 11$  in this case). By using the Monte Carlo technique, we determined both the minimum and maximum envelopes of all the possible neutron density distributions which satisfy Eq. (4.8) as the standard error-envelope. The errors of the neutron rms radii are also determined from the maximum and minimum value of the rms radii of the allowed neutron density distributions.

Figure 4.7 shows the case of  $^{208}\text{Pb}$ . The hatched area surrounded by the solid lines in Fig. 4.7 (c) shows the standard error-envelope of the neutron density in  $^{208}\text{Pb}$  estimated by Eq. (4.8), together with the DH neutron density distribution (dashed line). The three-parameter-Gaussian (3pG) neutron density extracted from the  $p$ - $^{208}\text{Pb}$  elastic scattering at 800 MeV using the second-order Kerman-McMaus-Thaler (KMT) model [58] (dash-dotted line) is also shown for comparison. The inset in Fig. 4.7 (c) is a magnification of the density distributions in the radial range from 4.5 fm to 6.5 fm.

The lines presented with the experimental observables for  $p$ - $^{208}\text{Pb}$  in Figs. 4.7 (a) and (b), are the medium-modified RIA calculations with the best-fit neutron density (solid), the 3pG neutron density (dash-dotted), and the DH nucleon density (dashed). Although there seems to be little difference between the medium-modified RIA calculations with the best-fit and 3pG neutron density since the solid line overlaps with the dash-dotted line extensively,  $\chi^2$  for the 3pG neutron density ( $= 255.3$ ) is about  $5\sigma$  ( $= 5\Delta\chi^2 \approx 55$ ) larger than  $\chi_{\min}^2$  ( $= 192.5$ ) especially at data points of high momentum transfer. The difference also appears in the rms radii. Our analysis gave a neutron rms radius for  $^{208}\text{Pb}$  of  $r_n = 5.653^{+0.026}_{-0.029}$  fm, which is 0.06 fm larger than the value of  $r_n = 5.593$  fm of the 3pG neutron density. This means that the data even at high momentum transfers can affect the rms radius. Because of the conservation of neutron number  $N$ , the information of the scattering observables at high and low momentum transfers, which reflects the bulk and surface structure, respectively, can doubly constrain the neutron radius. This allows us to extract the precise information about the neutron density from proton elastic scattering.

Figure 4.8 shows the percent deviation  $d$  between the experimental data and the medium-

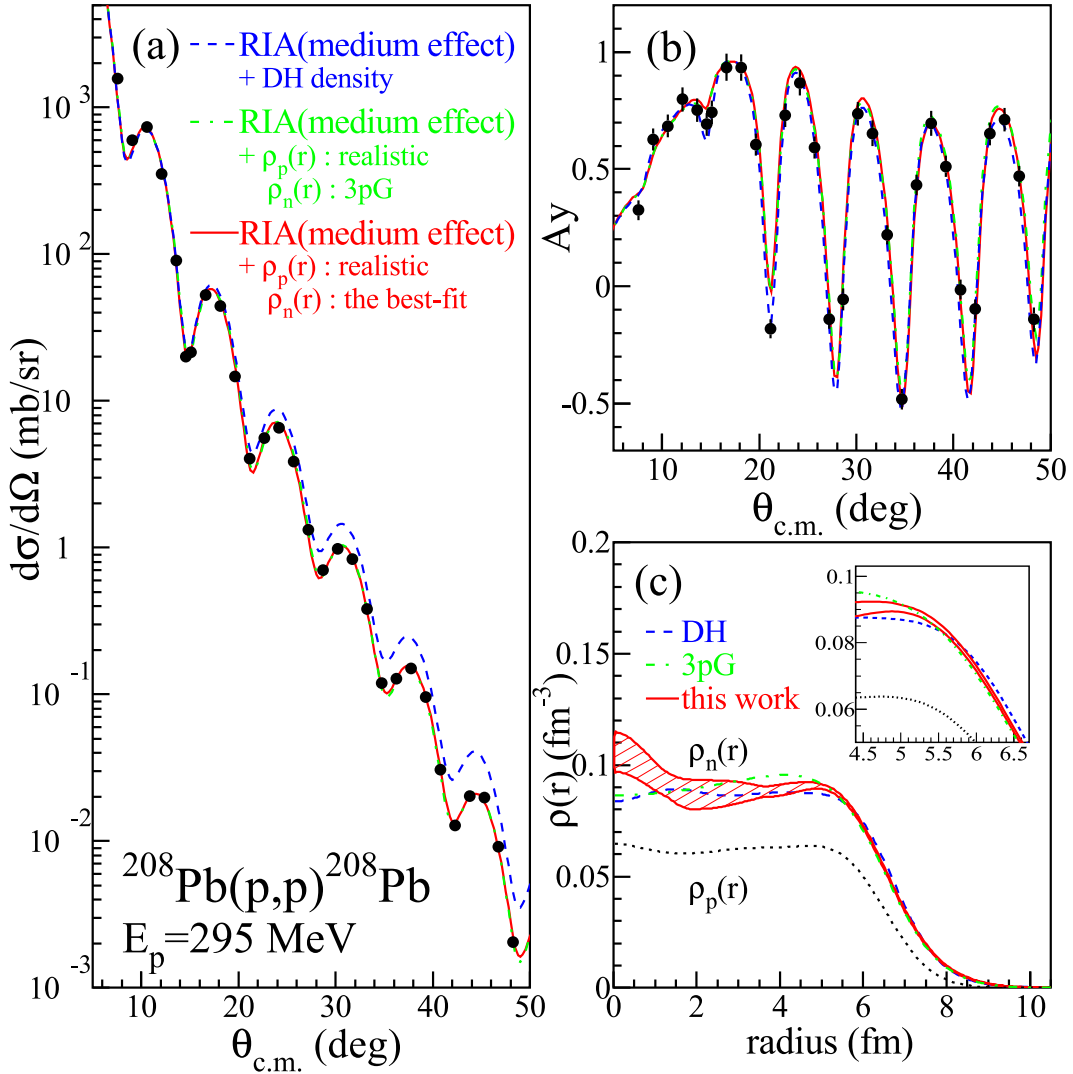


Figure 4.7: Results of fitting to the experimental data and extracted neutron density of  $^{208}\text{Pb}$  with its standard error-envelope (solid lines). The dashed and dash-dotted lines are medium-modified RIA calculations but using the DH nucleon densities and the 3pG neutron density by Ray [58] respectively. The dotted line in (c) is the realistic proton density.

modified RIA calculations for cross sections for  $^{208}\text{Pb}$ , which is written as

$$d = 200 \times \frac{\sigma_{\text{exp}} - \sigma_{\text{cal}}}{\sigma_{\text{exp}} + \sigma_{\text{cal}}}, \quad (4.9)$$

where  $\sigma_{\text{exp(cal)}}$  is the experimental (theoretical) cross section at each scattering angle. The red, green, and blue marks stand for the same definitions as in Fig. 4.7. The agreement with the experimental data is almost at the level of  $\pm 10\%$ . Compared to the calculation of the 3pG neutron density (green marks), our results (red marks) are found to be improved particularly

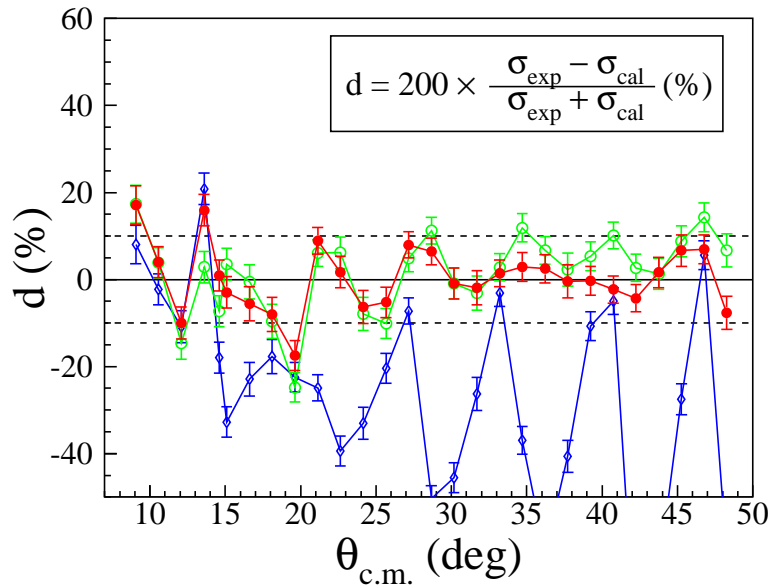


Figure 4.8: Percent deviation between the experimental data and the medium-modified RIA calculations of differential cross section at each angle defined as Eq. (4.9). The marks are the same definitions as Fig. 4.7. The lines are just for the guide.

at the backward angles. The percent deviation fluctuate largely at forward angles, where the angular distribution of the cross section rapidly changes.

The results for  $^{204,206}\text{Pb}$  are qualitatively similar to that for  $^{208}\text{Pb}$  and they are shown in Figs. 4.9 and 4.10.

It was found that our method to extract the neutron densities works successfully even for heavy nuclei like lead isotopes. The results of the fitting and the error estimation show that the systematic uncertainties of the experimental data are small enough to deduce the neutron radii with a good accuracy of 0.5 % and thereby the medium-modified RIA works well. However, the difference between the experimental data and the medium-modified RIA predictions still exists as the minimum reduced  $\chi^2$  is about 4.

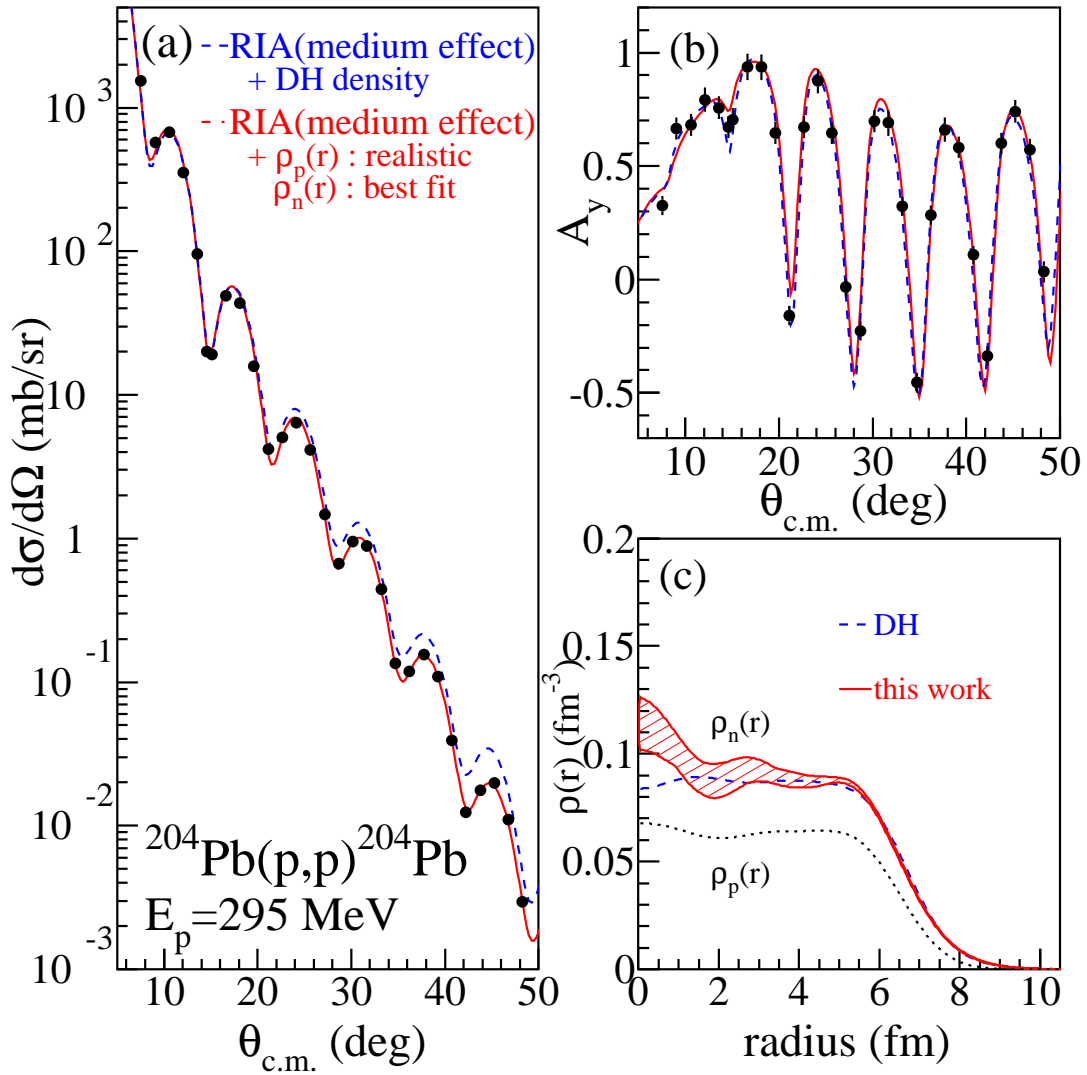


Figure 4.9: Results of fitting to the experimental data and extracted neutron density of  $^{204}\text{Pb}$  with its standard error-envelope (solid lines). The dashed lines are medium-modified RIA calculations but using the DH nucleon densities.

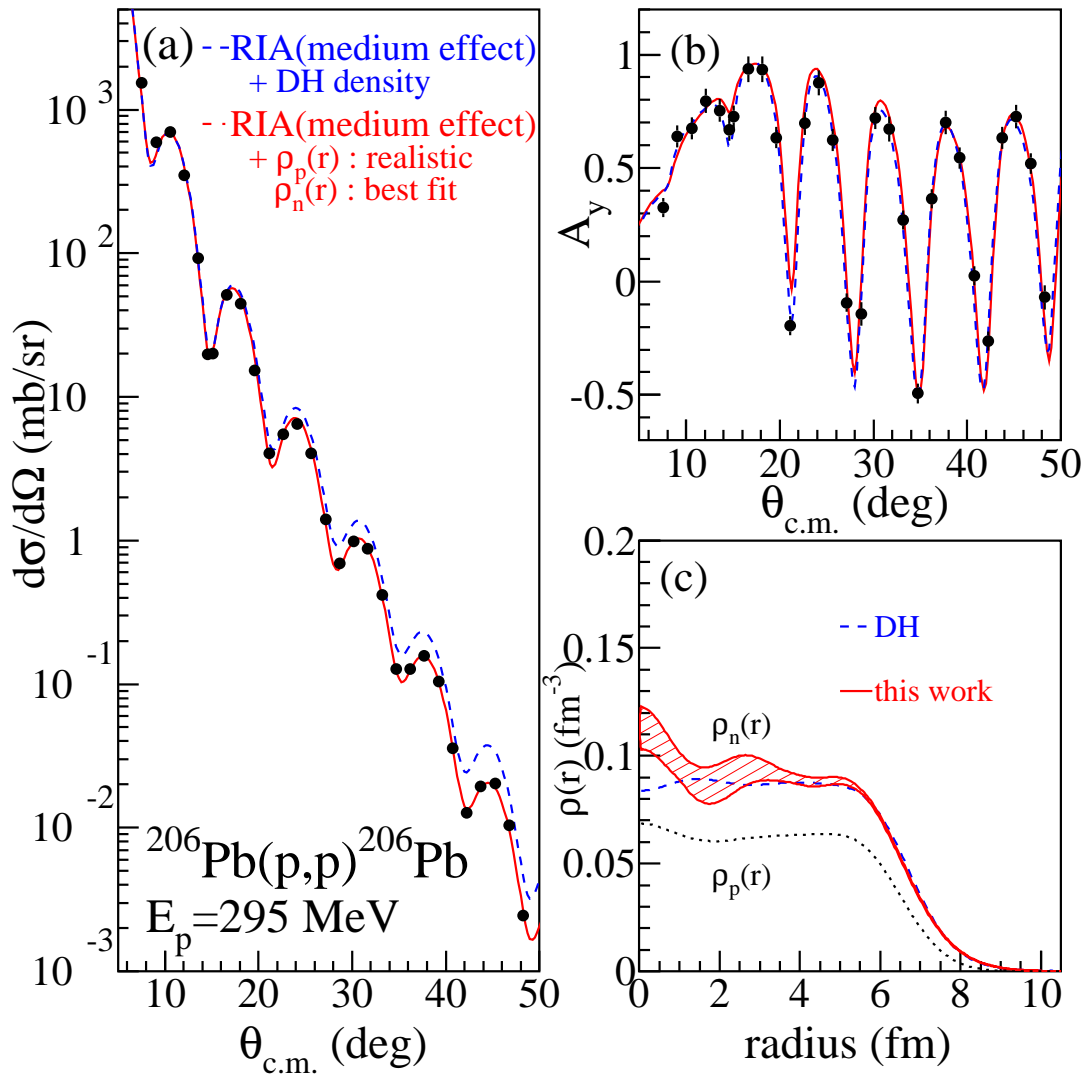


Figure 4.10: Results of fitting to the experimental data and extracted neutron density of  $^{206}\text{Pb}$  with its standard error-envelope (solid lines). The dashed lines are medium-modified RIA calculations but using the DH nucleon densities.

**“Model uncertainties”** In addition to the experimental uncertainty, we evaluated the error-envelopes including the model uncertainties in the medium-modified RIA. If the theoretical model was ideal, the reduced  $\chi_{\min}^2$  should be nearly equal to 1. However, the value of  $\chi_{\min}^2/\nu$  in this case is about 4, which is far from 1 and shows the incompleteness of this medium-modified RIA model as well as the unknown systematic errors of the experiment. To incorporate this incompleteness into Eq. (4.8) as the model uncertainties, we simply multiplied the experimental errors by a constant factor  $S$  which realizes  $\chi_{\min}^2/\nu = 1$ . Therefore, we defined a new chi-square as  $\tilde{\chi}^2 \equiv \chi^2/S^2$  assuming that  $\tilde{\chi}^2$  follows the same  $\chi^2$  distribution and Eq. (4.8):

$$\tilde{\chi}^2 \leq \tilde{\chi}_{\min}^2 + \Delta\tilde{\chi}^2, \quad (4.10)$$

where  $\tilde{\chi}_{\min}^2/\nu \equiv (\chi_{\min}^2/S^2)/\nu = 1$  and  $\Delta\tilde{\chi}^2 = \Delta\chi^2$ . Thus Eq. (4.10) is equivalent to

$$\begin{aligned} \chi^2 &\leq \chi_{\min}^2 + \Delta\chi^2 \times S^2 \\ &= \chi_{\min}^2 + \Delta\chi^2 \times (\chi_{\min}^2/\nu). \end{aligned} \quad (4.11)$$

The error-envelopes including the model uncertainties were estimated by Eq. (4.11) for  $^{204,206,208}\text{Pb}$  data <sup>d</sup>, where  $\Delta\chi^2$  for the  $^{204,206,208}\text{Pb}$  data is defined as the number of fitted parameters  $m$ , namely 11. The cross-hatched areas in Fig. 4.11 show the error-envelopes of the neutron density distributions for  $^{204,206,208}\text{Pb}$  obtained from Eq. (4.11) and the hatched areas are the standard error-envelopes due to Eq. (4.8). The radial distributions of the neutron surface densities  $4\pi r^2\rho(r)$  are also shown in Fig. 4.12 whose definitions are the same as Fig. 4.11. The neutron surface density distributions show that the errors of the neutron density distributions are large at both the inner (0–3 fm) and surface (8–10 fm) regions. Particularly, the error-envelopes of the surface regions causes the errors of the rms radii.

In this analysis for lead isotopes we neglected the density dependence of  $\rho$  and  $\pi$  mesons in the medium modification because the difference between the proton and neutron density is about 1/5 less than the normal density and the modification for  $\rho$  and  $\pi$  mesons is expected to be much smaller than for  $\sigma$  and  $\omega$  mesons. The error from this assumption is also included in the model uncertainties described by Eq. (4.11). When using model-dependent hadronic process, it is important to show these error-envelopes including the model uncertainties, in parallel with the conventional method of showing the experimental uncertainties only.

Table 4.2 lists the best-fit values of the SOG parameters  $Q_i$  and  $\chi_{\min}^2/\nu$  for each lead isotope. In addition, a fit to the upper and lower error-envelopes including the model uncertainties for each isotope was made by using the SOG parameters  $Q_i$  of Eq. (4.7) with the same  $\gamma$ ,  $N$ , and  $R_i$  as used in the investigation of the neutron densities. In this case the normalization condition is not satisfied ( $\sum Q_i \neq 1$ ) because the envelope is not the density distribution itself. The fitted parameters  $Q_i$  are listed in Table 4.3.

<sup>d</sup> In Ref. [70] it was reported that the error-envelopes of tin isotopes were estimated by Eq. (4.11) for the neutron-density parameters together with Eq. (4.8) for the medium-effect parameters, simultaneously. In that case, however, the envelope is doubly-estimated because the fluctuation of the medium-effect parameters indicated by Eq. (4.8) is a part of the uncertainties associated with the various model assumptions described by Eq. (4.11). Thus, Eq. (4.11) is enough to evaluate the error-envelopes including the model uncertainties.

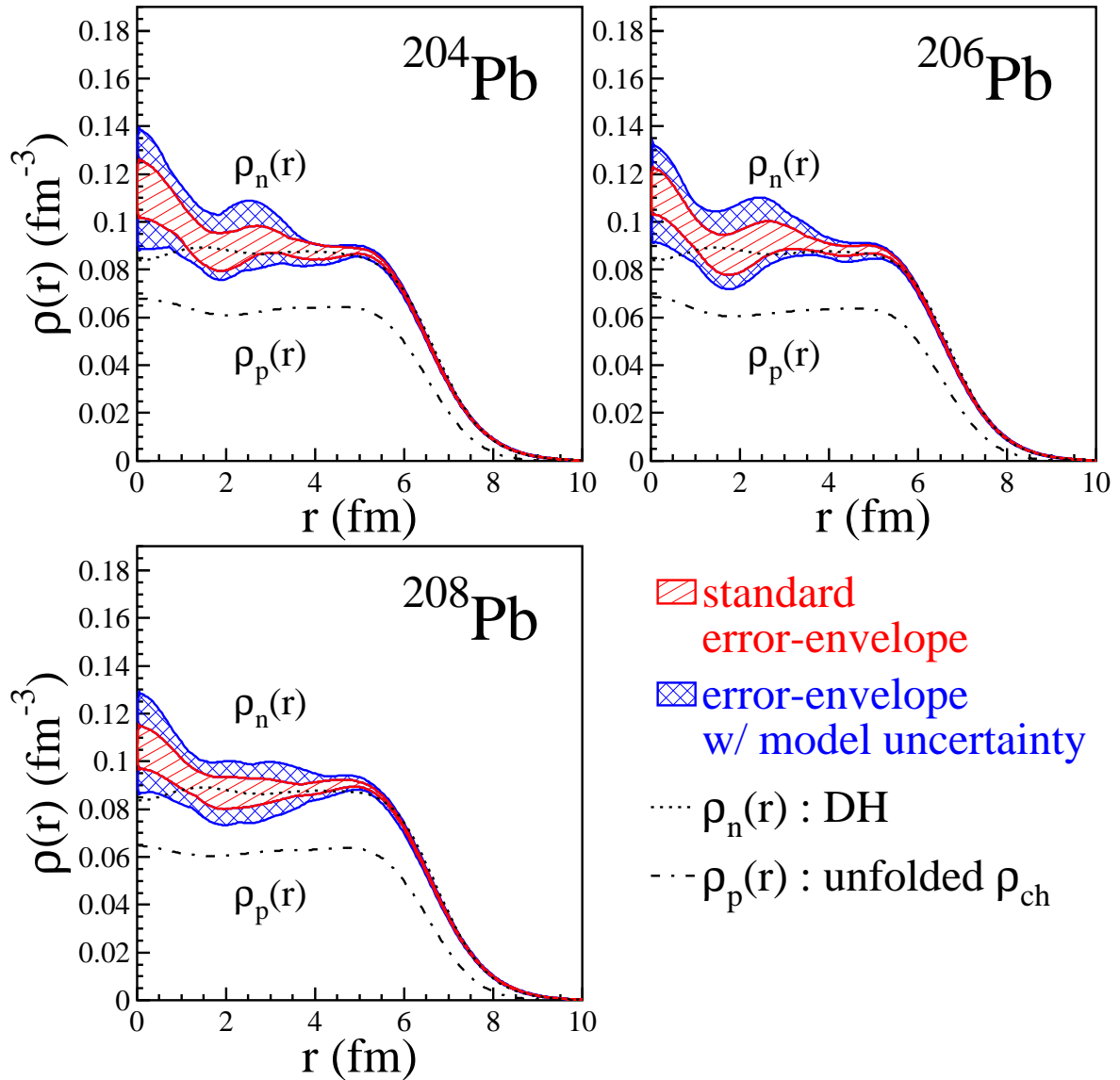


Figure 4.11: Extracted neutron densities for  $^{204,206,208}\text{Pb}$  with two types of error-envelopes shown together with DH neutron densities (dotted lines) and point proton densities by unfolding charge densities (dash-dotted lines). The cross-hatched blue and hatched red error-envelopes were estimated by Eq. (4.11) and Eq. (4.8), respectively.

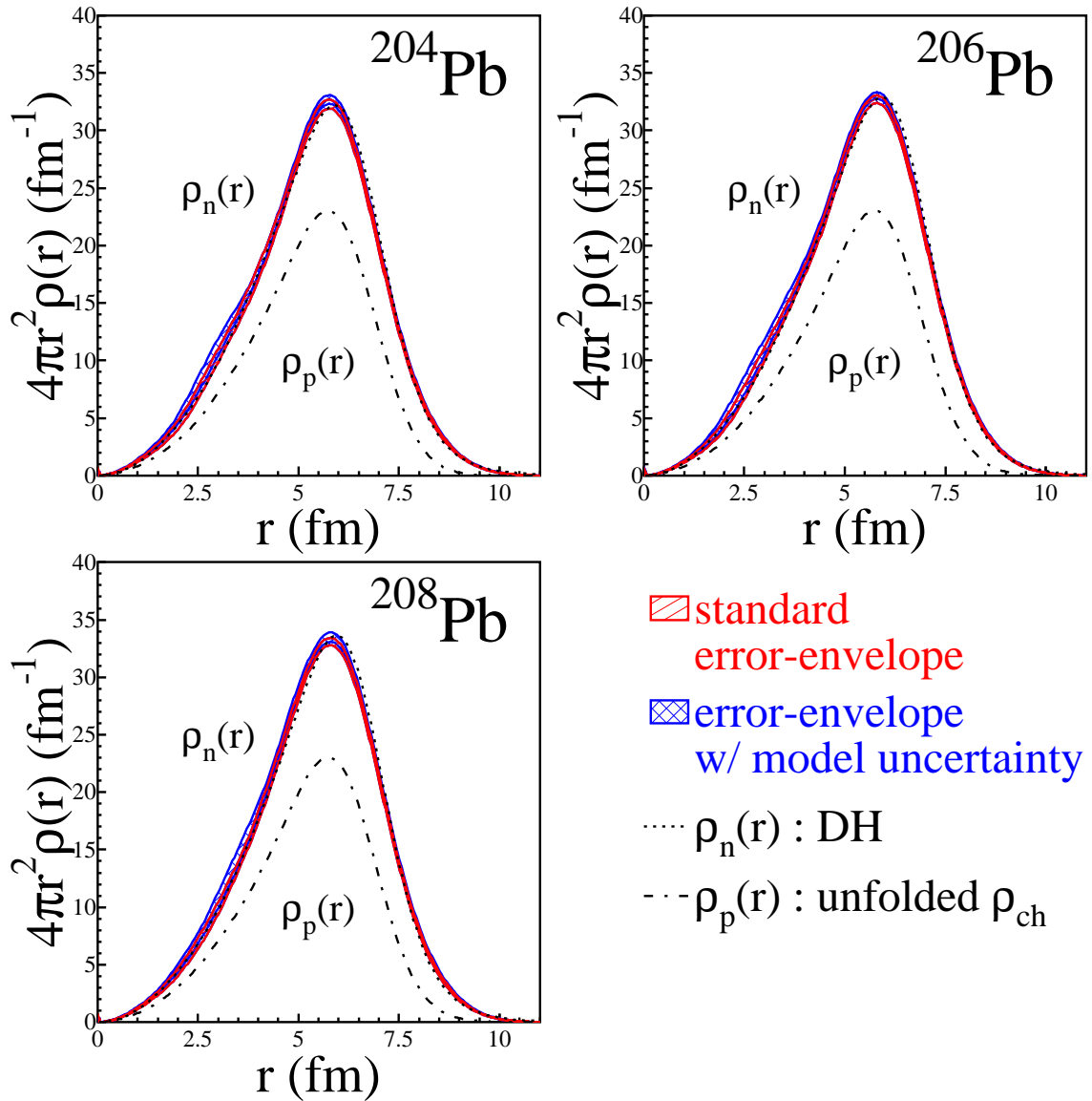


Figure 4.12: The radial distributions of neutron surface densities for  $^{204,206,208}\text{Pb}$  ( $4\pi r^2 \rho(r)$   $\text{fm}^{-1}$ ) with two types of error-envelopes shown together with DH neutron surface densities (dotted lines) and proton surface densities by unfolding charge densities (dash-dotted lines). The cross-hatched blue and hatched red error-envelopes were the same as Fig. 4.11.

Table 4.2: Best-fit SOG parameters of the neutron density distributions for  $^{204,206,208}\text{Pb}$ . The width  $\gamma$  ( $= 1.70/\sqrt{3/2}$ ) and position  $R_i$  of the  $i$ th Gaussian in Eq. (4.7) are fixed to the values of the charge distribution [54]. The number in the parentheses are the  $\chi^2_{\min}$  over the degrees of freedom  $\nu$  for each isotope.

$i$	$R_i$ (fm)	$Q_i$ (the fraction of $N$ in $i$ th Gaussian, $\sum_i Q_i = 1$ )		
		$^{204}\text{Pb}$ (180.1/47)	$^{206}\text{Pb}$ (185.3/47)	$^{208}\text{Pb}$ (192.5/47)
1	0.1	0.0065961	0.0068899	0.0053549
2	0.7	0.0126023	0.0123201	0.0106038
3	1.6	0.0063489	0.0000021	0.0208715
4	2.1	0.0323212	0.0231717	0.0096117
5	2.7	0.0703161	0.0998543	0.0767189
6	3.5	0.1150041	0.0677595	0.0639530
7	4.2	0.0413854	0.0961086	0.1324368
8	5.1	0.3317518	0.2860324	0.2484495
9	6.0	0.2994768	0.3249540	0.3467533
10	6.6	0.0315217	0.0333252	0.0271199
11	7.6	0.0526614	0.0495821	0.0581130
12	8.7	0.0000142	0.0000001	0.0000137

Table 4.3: Fitted SOG parameters  $Q_i$  of the upper and lower error-envelopes of the neutron density distribution for each lead isotope determined by Eq. (4.11).  $\gamma$ ,  $N$ , and  $R_i$  are the same as in Table 4.2, but the normalization condition is not satisfied in the case of the envelopes ( $\sum Q_i \neq 1$ ).

$i$	$R_i$ (fm)	$Q_i$					
		$^{204}\text{Pb}$		$^{206}\text{Pb}$		$^{208}\text{Pb}$	
		upper	lower	upper	lower	upper	lower
1	0.1	0.0094688	0.0000016	0.0140275	0.0001227	0.0084768	0.0001292
2	0.7	0.0127647	0.0189556	0.0007678	0.0155131	0.0096719	0.0172562
3	1.6	0.0000598	0.0140777	0.0000035	0.0003936	0.0132542	0.0157425
4	2.1	0.0311879	0.0063748	0.0704769	0.0046326	0.0280440	0.0000877
5	2.7	0.1455760	0.0595549	0.0864652	0.0624612	0.0850354	0.0723946
6	3.5	0.0080875	0.1396962	0.0398421	0.0909420	0.0764422	0.0516049
7	4.2	0.1394140	0.0019071	0.1516393	0.0225707	0.1243973	0.1416711
8	5.1	0.2843110	0.3534691	0.2477640	0.2273172	0.2607873	0.2296302
9	6.0	0.3396610	0.2677440	0.3580471	0.2415563	0.3540381	0.3434331
10	6.6	0.0181303	0.0464501	0.0231355	0.0216326	0.0245054	0.0257194
11	7.6	0.0593428	0.0452618	0.0566526	0.0330576	0.0663033	0.0502610
12	8.7	0.0000224	0.0000093	0.0000018	0.0000028	0.0000095	0.0000095



# Chapter 5

## RESULTS AND DISCUSSION

In the previous chapter, we succeeded in extracting the neutron density distributions of  $^{204,206,208}\text{Pb}$  and estimated their error-envelopes even including the uncertainties associated with our reaction model. The result of the density distributions and their parameters are already shown in Fig. 4.11, Tables 4.2 and 4.3. Now we show and discuss more details of the extracted quantities such as the neutron radii and the neutron skin thicknesses.

### 5.1 Charge, proton, and neutron rms radii

The differences between the rms radius of the best-fit neutron density and the maximum (minimum) rms radii in all the neutron densities constituting each error-envelope determined by Eq. (4.11) are listed in Table 5.1 as the upper (lower) errors of the rms radius of neutron  $\delta r_n^{\text{mdl}}$ , while the errors of the rms radii  $\delta r_n^{\text{std}}$  are the experimental ones determined by Eq. (4.8).

It is found that the effect of the model uncertainty on the errors of  $r_n$  for lead isotopes is as large as that of the experimental uncertainty. The neutron rms radii  $r_n$  were determined with a good accuracy of about 1 % ( $\approx 0.06$  fm) even including the model uncertainty.

Table 5.1: Root-mean-square radii of the charge  $r_{ch}$ , proton  $r_p^{\text{unfold}}$ , and neutron  $r_n$  used in this work. The two types of errors for  $r_n$ , namely,  $\delta r_n^{\text{mdl}}$  determined by Eq. (4.11) and  $\delta r_n^{\text{std}}$  by Eq. (4.8), are listed (all in fm).

Nucleus	$r_{ch}$	$r_p^{\text{unfold}}$	$r_n$	$\delta r_n^{\text{std}}$	$\delta r_n^{\text{mdl}}$
$^{204}\text{Pb}$	5.479(2)	5.420(2)	5.598	+0.029 -0.020	+0.047 -0.059
$^{206}\text{Pb}$	5.490(2)	5.433(2)	5.613	+0.026 -0.026	+0.048 -0.064
$^{208}\text{Pb}$	5.503(2)	5.442(2)	5.653	+0.026 -0.029	+0.054 -0.063

Table 5.2: Obtained values of  $r_n$ ,  $r_p$  and  $\Delta r_{np}$  for  $^{208}\text{Pb}$  compared with the previous results deduced from several experiments using various hadronic probes (all in fm). Except for this work and X-ray cascade from  $\bar{p}$ -atom (2), the errors are experimental only. The errors of this work stand for the total errors including the model uncertainties  $\delta r_n^{\text{mdl}}$  determined by Eq. (4.11).

Experiment	$r_p$	$r_n$	$\Delta r_{np}$
This work from Table. 5.1	5.442(2)	$5.653^{+0.054}_{-0.063}$	$0.211^{+0.054}_{-0.063}$
$^{208}\text{Pb}(p, p)$ at 800 MeV [58]*	5.45	5.59(4)	0.14(4)
$^{208}\text{Pb}(p, p)$ at 650 MeV [62]†	5.46	5.66(4)	0.20(4)
Isospin diffusion data in Sn + Sn at 50 MeV/u [51]‡	-	-	0.22(4)
GDR from $(\alpha, \alpha')$ at 120 MeV[61]	-	-	0.19(9)
PDR from $^{129-132}\text{Sn}(\gamma, \gamma')$ [68]¶	-	-	0.18(4)
PDR in $^{68}\text{Ni}$ and $^{132}\text{Sn}$ [72]	-	-	0.194(24)
X-ray cascade from $\bar{p}$ -atom (1)[67]**	5.44	5.60	$0.16(2)_{\text{stat}}(4)_{\text{syst}}$
X-ray cascade from $\bar{p}$ -atom (2)[73]††	5.45	$5.65(5)_{\text{mdl}}$	$0.20(4)_{\text{exp}}(5)_{\text{mdl}}$

\*2nd-order KMT potential assuming 3pG neutron density.

†Density-dependent  $t$ -matrix using model-independent FB neutron density.

‡21 sets of the Skyrme interaction parameters.

¶PDR strengths analyzed by RHB+RQRPA calculations with DD-ME parameterization.

||Energy weighted sum rule by PDR data globally fitted with various mean field models

\*\*antiproton-nucleus optical potentials assuming 2pF proton and neutron density.

††newly developed Skyrme parameterization Skxsxx constrained by antiproton data of Ref. [67].

## 5.2 Neutron skin thicknesses

“**Systematic change of  $\Delta r_{np}$** ” The systematic behavior of the extracted neutron skin thicknesses  $\Delta r_{np}$  for lead isotopes with the two types of error bars due to  $\delta r_n^{\text{std}}$  (red) and  $\delta r_n^{\text{mdl}}$  (blue) is shown with previous experimental and theoretical results [9–11, 19, 22, 23, 62, 67, 68, 73, 117] in Fig. 5.1. The errors due to  $\delta r_n^{\text{std}}$  (red) are the experimental only and thus, should be compared with other experimental results. The present result shows a slight increase of the neutron skin thickness at  $^{208}\text{Pb}$ .

As seen in Fig. 5.1, the resulting values of the neutron skin thicknesses have similar values and tendency to other results except for the case of NL3 parameterization [19] within the error bars. The recently developed parameterizations of DD-ME2, DD-PC1, FSUGold, and Skxs20 are particularly consistent with our result. The neutron skin thickness and density of  $^{204}\text{Pb}$  was firstly extracted by our measurements and will be useful to constrain the various theoretical models.

“ $\Delta r_{np}$  for  $^{208}\text{Pb}$ ” The obtained neutron skin thickness  $\Delta r_{np}$  for  $^{208}\text{Pb}$  is compared with those obtained from previous experiments in Table 5.2. The listed experimental results including this work are not very different within the error bars. However, none of the previous results considers the model ambiguities used in their analyses. In addition, except for the proton elastic scattering approaches, other analysis methods assumed the model-dependent shape of the neutron density, and thus it is inherently difficult to extract the precise values of the neutron skin thicknesses and the density distributions as well as to estimate the model uncertainties due to many theoretical assumptions.

In Table 5.3 we list the typical relativistic and non-relativistic mean field models with various parameter sets. Non-relativistic mean field models with D1S [118], D1N [118], SIII [116], SkM\* [9], SkI3 [119], SkI4 [119], SkP [10], SkX [12], Sly4 [11], SSk [120], GSkI [120], GSkII [120], BSk14 [121], BSk17 [122], and BSk20 [123] parameterization are shown. Since the relativistic mean field (RMF) model was originally proposed by Walecka in Ref. [124], the effective Lagrangian has been adjusted to the well-known many nuclear properties and developed from many theoretical researches. They are classified into several types of the RMF parameterizations such as NL1 [125], NL3 [19], NL-SH [126], TM1 [18], G2 [127], PK1 [114], FSUGold [23], FSUGZ03 [24], BKA20 [25], BKA22 [25], BKA24 [25], and IU-FSU [128] for the nonlinear meson-meson coupling model, PKDD [114], DD-ME1 [129], DD-ME2 [22], and DD-PC1 [117] for the density-dependent meson-nucleon coupling model, PC-F1 [21], PC-LA [130], PC-PK1 [131], and FKVW [132] for the point-coupling model, SL1 [26], SLC [26] for the Brown-Rho scaling model, QMC-I and QMC-II [133] for the quark-meson coupling model. These parameterizations are tuned to reproduce the properties of various finite nuclei. Previously, predictions of the neutron skin thicknesses widely differed between the non-relativistic and relativistic mean field models, but recent studies using newly developed relativistic parameterizations such as DD-ME and FSUGold have reported  $\Delta r_{np}$  results closer to those of non-relativistic models than the relativistic model with NL1, NL3, NL-SH, and TM1 parameterization.

In the case of FSUGold parameterization, for example, two additional coupling constants which represent non-linear vector and isoscalar–isovector couplings, were introduced based on relativistic effective field theory [16]. The new relativistic parameterization has been calibrated to explain the measurements of the giant monopole resonance in  $^{90}\text{Zr}$  and  $^{208}\text{Pb}$  and the isovector giant dipole resonance in  $^{208}\text{Pb}$ , without compromising the quality of the other ground state properties such as the binding energy per nucleon and the charge radii. The predicted value of  $\Delta r_{np} = 0.21$  fm for  $^{208}\text{Pb}$  by FSUGold parameterization is in close agreement with our result.

The most recent theoretical studies [51, 72, 73] as listed in Table 5.2 which are constrained by the most recent experimental data, namely, the X-ray cascade of antiprotonic atoms [67], isospin diffusion in heavy-ion collisions [134], and pigmy dipole resonance (PDR) data [68], have reported neutron skin thicknesses of  $^{208}\text{Pb}$  of 0.20(4) fm [73], 0.22(4) fm [51], and 0.194(24) fm [72], respectively. These obtained values are in remarkable agreement with ours of  $\Delta r_{np} = 0.211_{-0.063}^{+0.054}$  fm.

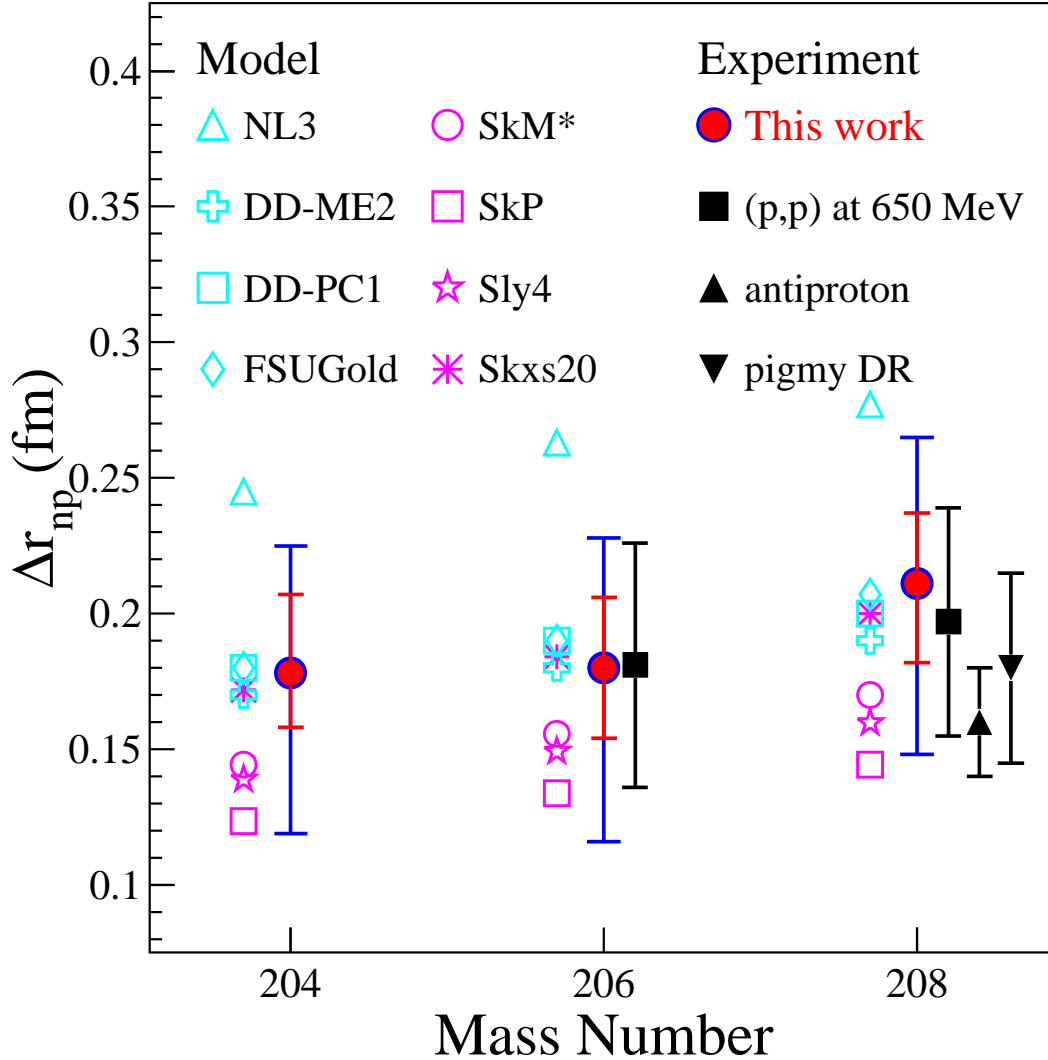


Figure 5.1: Systematic behavior of the neutron skin thicknesses for  $^{204,206,208}\text{Pb}$ . The filled circles are the results of this work with the two types of error bars. The red and blue lines represent the errors due to the experimental only  $\delta r_n^{\text{std}}$  and including the model uncertainties  $\delta r_n^{\text{mdl}}$ , respectively. The filled squares, triangle, and inverted triangle are from the analysis of proton elastic scattering at 650 MeV [62], X-ray cascade from antiprotonic atoms [67], and PDR strengths from  $^{129-132}\text{Sn}(\gamma, \gamma')$  [68], respectively, with their statistical errors only. The open triangles, crosses, squares and diamonds show the calculations of relativistic mean field models (pale blue marks) with NL3 [19], DD-ME2 [22], DD-PC1 [117], and FSUGold [23] parameterization while the open circles, squares, stars and asterisks are from non-relativistic mean field models (pink marks) with SkM\* [9], SkP [10], Sly4 [11], and Skxs20 [73] parameterization. DD-ME2, FSUGold, and Skxs20 parameterizations have been recently developed and conform closely to all the extracted neutron skin thicknesses.

**“Symmetry energy coefficients”** Correlations between the neutron skin for  $^{208}\text{Pb}$  and the symmetry energy coefficients of nuclear matter have also been reported by various recent theoretical studies [44–48, 51] as mentioned in Chap. 1 (the correlation factor is almost 1 for  $^{208}\text{Pb}$ ). In Table 5.3, the nuclear matter incompressibility  $K_0$ , the symmetry energy  $\mathcal{S}(\rho_{\text{sat}})$  and its slope  $L$  and curvature  $K_{\text{sym}}$  at saturation density  $\rho_{\text{sat}}$  as defined by Eqs. (1.2)–(1.6), are listed compared with the neutron skin thicknesses for  $^{208}\text{Pb}$ . The incompressibility  $K_0$  is now expected to be about 210–250 MeV [22–25, 38, 39, 135, 136] constrained by many measurements of isoscalar giant resonances for various nuclei [36, 37, 40]. The symmetry energy  $\mathcal{S}(\rho_{\text{sat}})$  at saturation is also known to be  $\sim 32$  MeV, but  $L$  and  $K_{\text{sym}}$  are still less certain and their predicted values vary widely among many theoretical models. Particularly the slope coefficient  $L$  of the symmetry energy at saturation density is strongly correlated with  $\Delta r_{np}$  for  $^{208}\text{Pb}$  [35, 51].

Then we tried to extract  $L$  by examining the global correlation between  $\Delta r_{np}$  for  $^{208}\text{Pb}$  and  $L$  of typical theoretical predictions as listed in Table 5.3. First, the correlations between neutron skin thickness for  $^{208}\text{Pb}$  and several EOS coefficients such as  $K_0$ ,  $\mathcal{S}(\rho_{\text{sat}})$ ,  $L$ , and  $K_{\text{sym}}$  calculated with the listed parameterizations, are shown in Figs. 5.2, 5.3, 5.4, and 5.5, respectively. The incompressibility  $K_0$  is not correlated with the neutron skin. The hatched areas in Fig. 5.2 represent the two range of  $K_0$ , namely, 205–240 MeV and 230–250 MeV constrained by Itoh *et al.* [36] and Li *et al.* [40], respectively.

On the other hand, the symmetry energy  $\mathcal{S}(\rho_{\text{sat}})$  and slope  $L$  coefficients predicted by those parameterizations, whether relativistic or non-relativistic, show strong linear correlations with  $\Delta r_{np}$ . Assuming that these linearity were valid as reported in many articles, linear fittings were performed. The solid straight lines in Figs. 5.4 and 5.5 show the linear fittings. Since fitting errors are almost negligible with respect to the errors of the neutron skin thickness, we deduced the range of acceptable values for  $\mathcal{S}(\rho_{\text{sat}})$  and  $L$  corresponding to the errors of  $\Delta r_{np}$ . Our results are  $\mathcal{S}(\rho_{\text{sat}}) = 33.7^{+4.0}_{-4.6}$  MeV and  $L = 74.3^{+37.9}_{-20.3}$  MeV by using the extracted  $\Delta r_{np}$  for  $^{208}\text{Pb}$ . The red and blue thick lines on the  $y$ -axis in all the Figures represent the two types of the errors of  $\Delta r_{np}$  for  $^{208}\text{Pb}$  due to the experimental errors only (red) and the total errors including the model uncertainties (blue), respectively. Those on the  $x$ -axis in Figs. 5.4 and 5.5 are the resulted range of  $\mathcal{S}(\rho_{\text{sat}})$  and  $L$ . The red and blue boxes in Fig. 5.6 are the constraint regions on  $\mathcal{S}(\rho_{\text{sat}})$  -  $L$  plane by the extracted  $\Delta r_{np}$  for  $^{208}\text{Pb}$ .

For  $^{204,206}\text{Pb}$ , similar correlations can be seen whereas there are small number of theoretical models we can use. Thus, the same fittings as in the case of  $^{208}\text{Pb}$  were carried out. Figures 5.7, 5.8, 5.9, and 5.10 show the obtained ranges of  $\mathcal{S}(\rho_{\text{sat}})$  and  $L$  for  $^{204,206}\text{Pb}$ , respectively.

Figure 5.11 and 5.12 show all the obtained regions  $\mathcal{S}(\rho_{\text{sat}})$  -  $L$  plane for  $^{204,206,208}\text{Pb}$  due to the experimental errors and the total errors, respectively. Since the model uncertainties are not independently determined for each isotopes, the weighted average of three ranges due to the total errors in Fig. 5.12 must not be performed. On the other hand, the experimental errors are independent among three isotopes. Therefore, we deduced the weighted average of three ranges due to the experimental errors as shown in Fig. 5.11. The combined ranges of  $\mathcal{S}(\rho_{\text{sat}})$  and  $L$  resulted in  $\mathcal{S}(\rho_{\text{sat}}) = 33.0 \pm 1.1$  MeV and  $L = 67.0 \pm 12.1$  MeV, respectively, which is

consistent with  $L = 88 \pm 25$  MeV obtained from the recent analysis of isospin diffusion data [51] and  $L = 65 \pm 16$  MeV determined by the energy-weighted sum rule of PDR data [72].

However, the errors of  $\Delta r_{np}$  including model uncertainties is still so large that the constraint on the slope coefficient  $L$  is wide with the range of 30–90 MeV by such a rough estimation as the global correlation approach mentioned above. Therefore we need to develop our analysis and experimental data for a more precise measurement of the neutron skin thickness. Extending our analysis to other nuclei is also important to improve the constraint on the value of the slope  $L$ .

Table 5.3: Neutron skin thickness for  $^{208}\text{Pb}$  and the nuclear matter properties at saturation density, such as the incompressibility coefficient  $K_0$ , the symmetry energy  $\mathcal{S}(\rho_{\text{sat}})$ , its slope  $L$ , and the curvature  $K_{\text{sym}}$  in various relativistic and non-relativistic theoretical models.

Model	$\Delta r_{np}$ (fm)	$\mathcal{E}_0(\rho)$		$\mathcal{S}(\rho)$	
		$K_0$ (MeV)	$\mathcal{S}(\rho_{\text{sat}})$ (MeV)	$L$ (MeV)	$K_{\text{sym}}$ (MeV)
<i>Relativistic</i>					
<i>nonlinear coupling</i>					
NL1 [125]	0.321	212	43.5	140.1	143
NL3 [19]	0.280	271.8	37.4	118.6	100
NL-Z [137]	0.307	173	41.7	133.3	
NL-SH [126]	0.266	355	36.1	113.6	80
TM1 [18]	0.271	281	36.9	110.8	34
G2 [127]	0.257	215	36.4	100.7	-7
PK1 [114]	0.260	282.6	37.6	116	55
FSUGold [23]	0.207	230	32.6	60.6	-52
FSUGZ03 [24]	0.190	233	31.6	64	-11
BKA20 [25]	0.200	240	32.3	76	-15
BKA22 [25]	0.220	227	33.3	79	-9
BKA24 [25]	0.240	228	34.3	85	-15
IU-FSU [128]	0.160	231.2	31.3	47.2	
<i>density dependent</i>					

*Continued.*

Model	$\Delta r_{np}$ (fm)	$K_0$ (MeV)	$S(\rho_{\text{sat}})$ (MeV)	$L$ (MeV)	$K_{\text{sym}}$ (MeV)
PKDD [114]	0.240	262.2	36.8	90	-80
DD-ME1 [129]	0.200	245	33.1	55	-101
DD-ME2 [22]	0.193	251	32.3	51	-87
DD-PC1 [117]	0.200	230	33	70	-108
<i>point coupling</i>					
PC-F1 [21]	0.270	255	37.8	117	75
PC-LA [130]	0.250	264	37.2	108	-61
PC-PK1 [131]	0.260	238	35.6	113	95
FKVW [132]	0.200	250	33.1	80	11
<i>Brown-Rho scaling</i>					
SLC [26]	0.210	230	31.6		
<i>quark-meson coupling</i>					
QMC-I [133]	0.26	280	35		
QMC-II [133]	0.27	382	35		
<hr/> Non-relativistic <hr/>					
<i>Gogny</i>					
D1S [118]	0.135	210	32.0	22.4	-252
D1N [118]	0.142	230	29.3	31.9	
<i>Skyrme</i>					
SIII [116]	0.13	355	28.2	9.9	-394
SkM* [9]	0.17	216	30.0	45.8	-156
SkI3 [119]	0.22	258	34.8	100.5	73
SkI4 [119]	0.18	248	29.5	60.4	-41
SkP [10]	0.145	201	30.0	19.7	-267
SkX [12]	0.16	271	31.1	33.2	-252
Skxs20 [73]	0.200	200			
Sly4 [11]	0.16	229.9	32.0	46.0	-120
Sk255 [136]	0.250	255.0	37.4	95.0	-58.3
Sk272 [136]	0.243	271.6	37.4	91.7	-67.8
SSk [120]	0.17	229.2	33.5	52.8	
GSKI [120]	0.19	230.2	32.0	63.5	

Continued.

Model	$\Delta r_{np}$ (fm)	$K_0$ (MeV)	$S(\rho_{\text{sat}})$ (MeV)	$L$ (MeV)	$K_{\text{sym}}$ (MeV)
GSkII [120]	0.20	233.6	34.2	66.8	
BSk14 [121]	0.16	239.3	30.0	43.9	
BSk17 [122]	0.15	241.7	30.0	36.3	
BSk20 [123]	0.14	241.4	30.0	37.4	-137
<b>This work</b>	$0.211^{+0.054}_{-0.063}$	-	-	-	-

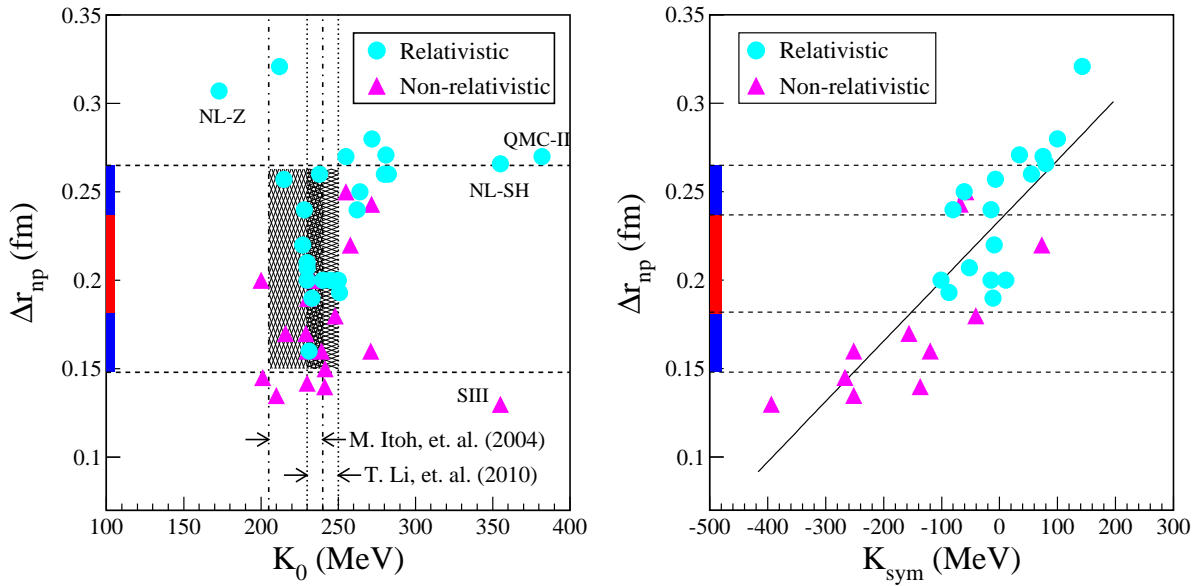


Figure 5.2:  $\Delta r_{np}$  for  $^{208}\text{Pb}$  (fm) vs  $K_0$  (MeV). Figure 5.3:  $\Delta r_{np}$  for  $^{208}\text{Pb}$  (fm) vs  $K_{\text{sym}}$  (MeV).

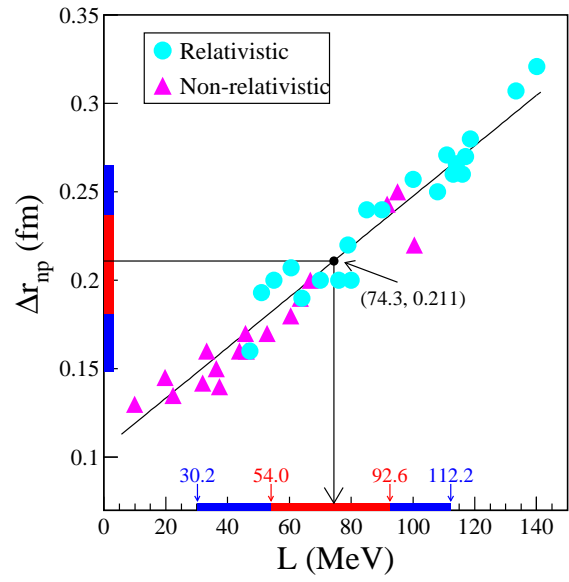
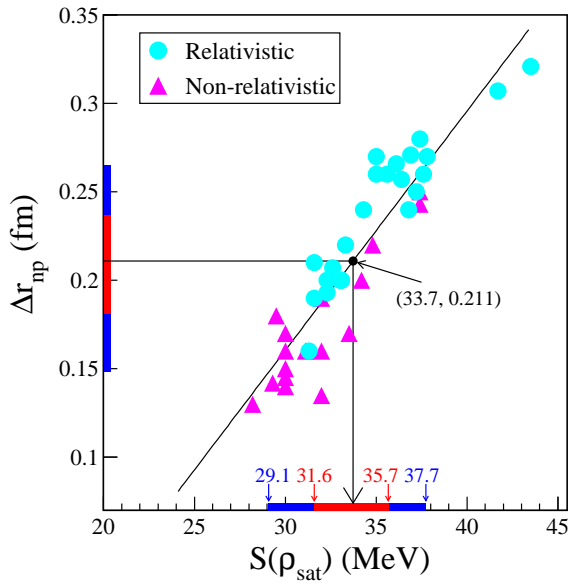


Figure 5.4:  $\Delta r_{np}$  for  $^{208}\text{Pb}$  (fm) vs  $S(\rho_{\text{sat}})$  (MeV). Figure 5.5:  $\Delta r_{np}$  for  $^{208}\text{Pb}$  (fm) vs the slope coefficient  $L$  (MeV).

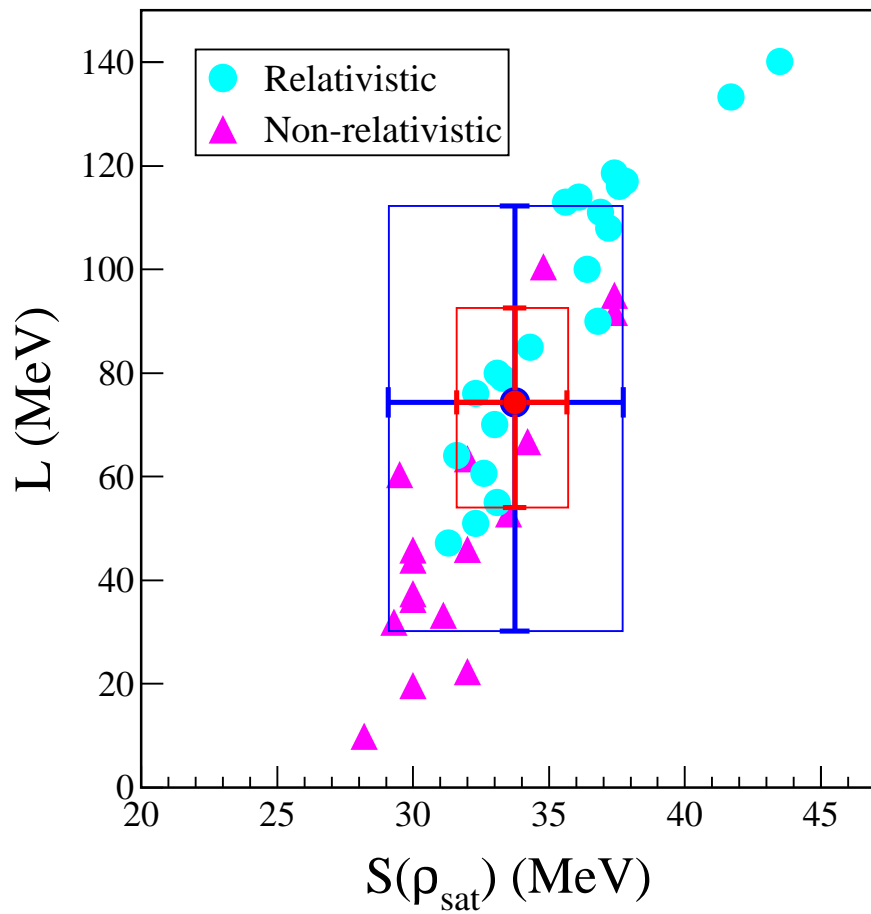


Figure 5.6:  $L$  (MeV) vs  $S(\rho_{\text{sat}})$  (MeV). Surrounded areas are the extracted ranges of  $S(\rho_{\text{sat}})$  and  $L$  from  $\Delta r_{np}$  for  $^{208}\text{Pb}$  as shown in Figs. 5.4 and 5.5

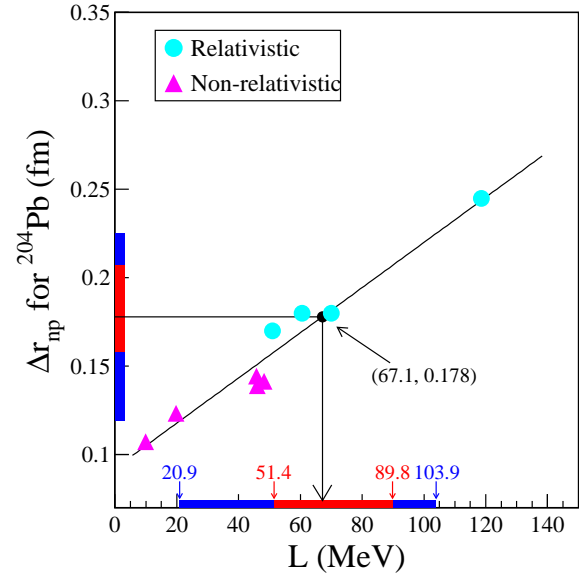
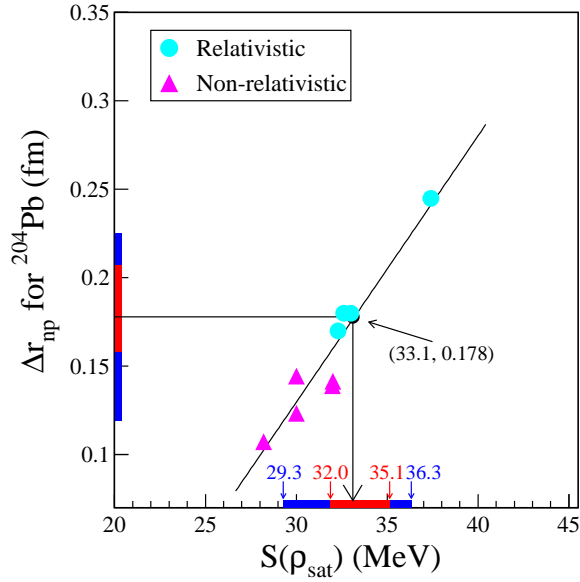


Figure 5.7:  $\Delta r_{np}$  for  $^{204}\text{Pb}$  (fm) vs  $S(\rho_{\text{sat}})$  (MeV). Figure 5.8:  $\Delta r_{np}$  for  $^{204}\text{Pb}$  (fm) vs the slope coefficient  $L$  (MeV).

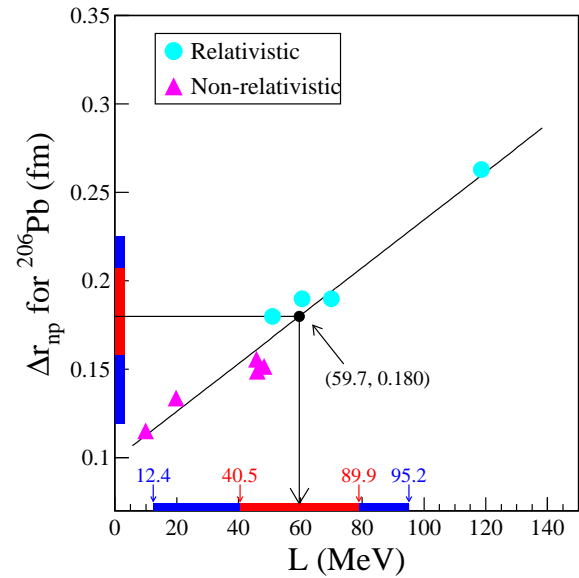
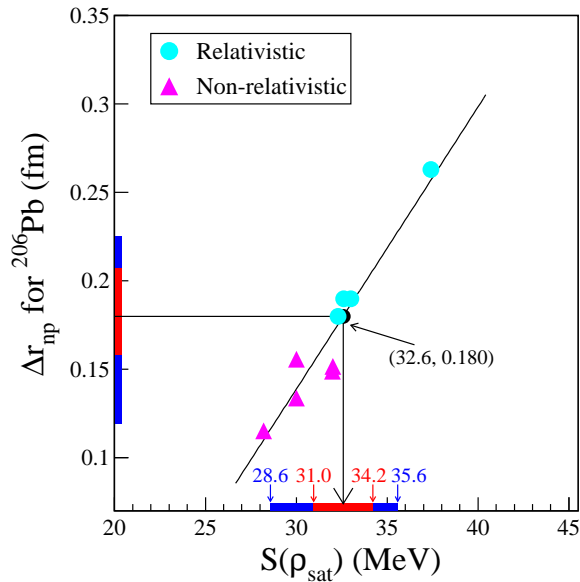


Figure 5.9:  $\Delta r_{np}$  for  $^{206}\text{Pb}$  (fm) vs  $S(\rho_{\text{sat}})$  (MeV). Figure 5.10:  $\Delta r_{np}$  for  $^{206}\text{Pb}$  (fm) vs the slope coefficient  $L$  (MeV).

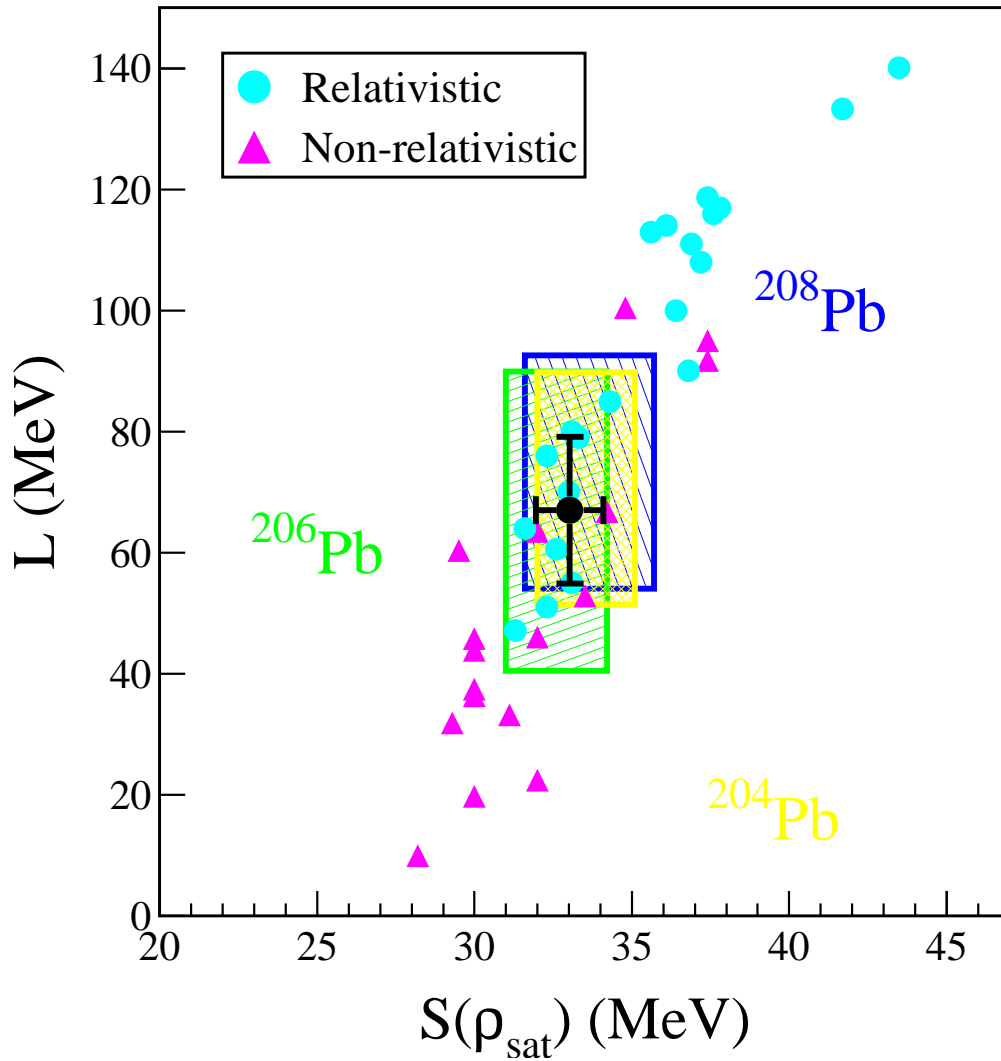


Figure 5.11: All the extracted regions of  $L$  vs  $S(\rho_{\text{sat}})$  for  $^{204,206,208}\text{Pb}$  correspond to the red lines in Figs. 5.4, 5.5, 5.7, 5.8 5.9, and 5.10 due to the experimental errors of the extracted  $\Delta r_{np}$  only. Black filled circle and solid error bars are the weighted average of these three regions.

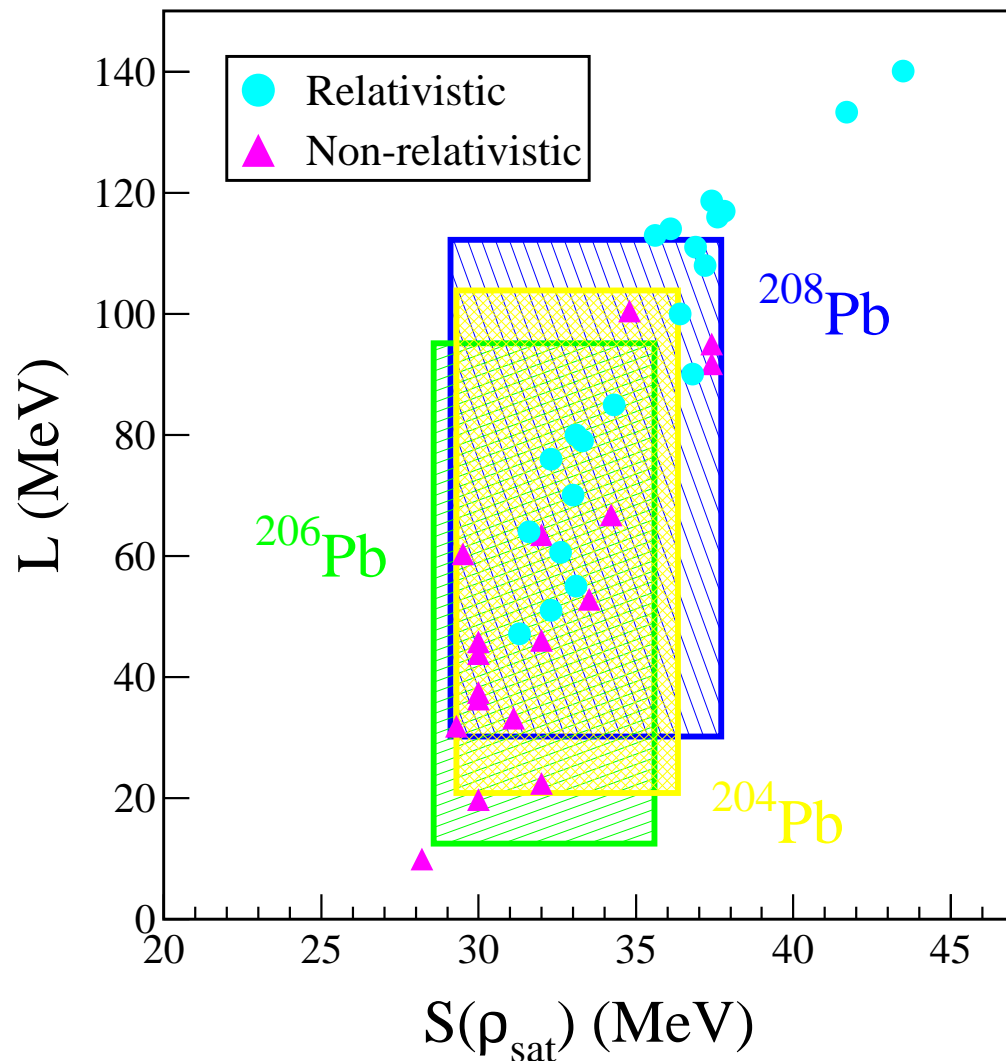


Figure 5.12: Similar to Fig. 5.11, but the extracted regions correspond to the blue lines in Figs. 5.4, 5.5, 5.7, 5.8 5.9, and 5.10 due to the total errors of the extracted  $\Delta r_{np}$  including the model uncertainties.

**“Isobaric incompressibility”** We also examined a more advanced topic of the EOS briefly. It has been found that the contributions of the higher order terms in Eqs. (1.2) and (1.4) are not necessarily negligible especially for the incompressibility of the asymmetric nuclear matter as discussed in Ref. [138, 139]. The EOS of the symmetric nuclear matter  $\mathcal{E}_0(\rho)$  is expanded to one-order higher than Eq. (1.2). The coefficient of third-order derivative  $J_0$  in the expansion of  $\mathcal{E}_0(\rho)$  is expressed as

$$\mathcal{E}_0(\rho) = \mathcal{E}_0 + \frac{K_0}{2!}\epsilon^2 + \frac{J_0}{3!}\epsilon^3 + \mathcal{O}(\epsilon^4), \quad (5.1)$$

$$J_0 = 27\rho_{\text{sat}}^3 \left. \frac{d^3\mathcal{E}_0(\rho)}{d\rho^3} \right|_{\rho=\rho_{\text{sat}}}. \quad (5.2)$$

Recently the isospin dependence of incompressibility has been studied by the high-quality data of isoscalar giant monopole resonances (ISGMR) in Sn isotopes measured from  $(\alpha, \alpha')$  reaction at RCNP [39, 40, 139, 140]. The extended, so-called, isobaric incompressibility  $K(\delta)$  with isospin asymmetry  $\delta$  can be expressed as

$$K(\delta) = K_0 + K_\tau\delta^2 + \mathcal{O}(\delta^4) \quad (5.3)$$

$$K_\tau \approx K_{\text{sym}} - 6L - \frac{J_0}{K_0}L, \quad (5.4)$$

where the third term of the right hand in Eq. (5.4) is derived from the higher-order coefficient  $J_0$  in Eq. (5.1). The asymmetry term  $K_\tau$  characterizes the isospin dependence of the incompressibility  $K(\delta)$  and also very important to understand the properties of the asymmetric nuclear or neutron matter such as neutron stars. Chen *et al.* in Ref. [138] obtained a value of  $K_\tau = -370 \pm 120$  MeV from the analysis of isospin diffusion data considering the higher-order terms of the EOS and the incompressibility at saturation. However, Li *et al.* in Ref. [40] resulted in  $K_\tau = -550 \pm 100$  MeV much different from that of Chen *et al.* The result of Li *et al.* were obtained from the ISGMR strength distributions in Sn isotopes by using the empirical expression of the finite nucleus incompressibility  $K_A$  with the lowest order terms only [141]:

$$K_A \approx K_0 + K_{\text{surf}}A^{-1/3} + K_\tau\alpha^2 + K_{\text{Coul}}\frac{Z^2}{Z^{4/3}}, \quad (5.5)$$

where  $A$ ,  $Z$ ,  $K_{\text{surf}}$ , and  $K_{\text{Coul}}$  are the mass and atomic number, the surface, and Coulomb terms with  $\alpha = (N - Z)/A$ . The higher-order terms of this expansion, which was neglected in their analysis, are not negligible as pointed out in Ref. [142]. That is the reason of the discrepancy between the results of Chen and Li. Thus, since the analysis method of Ref. [40] are still ambiguous to extract the  $K_\tau$  only, we used the result of Chen *et al.* [138] as shown in the hatched area in Fig. 5.13. While the effect of  $L$  on  $K_\tau$  accounts for about 75%, no correlation is found between  $K_\tau$  and  $\Delta r_{np}$  (or  $L$ ) in Fig. 5.13. However, combined with the range of  $K_\tau = -370 \pm 120$  MeV, our result of  $\Delta r_{np}$  for  $^{208}\text{Pb}$  put some constraints on the theoretical models.

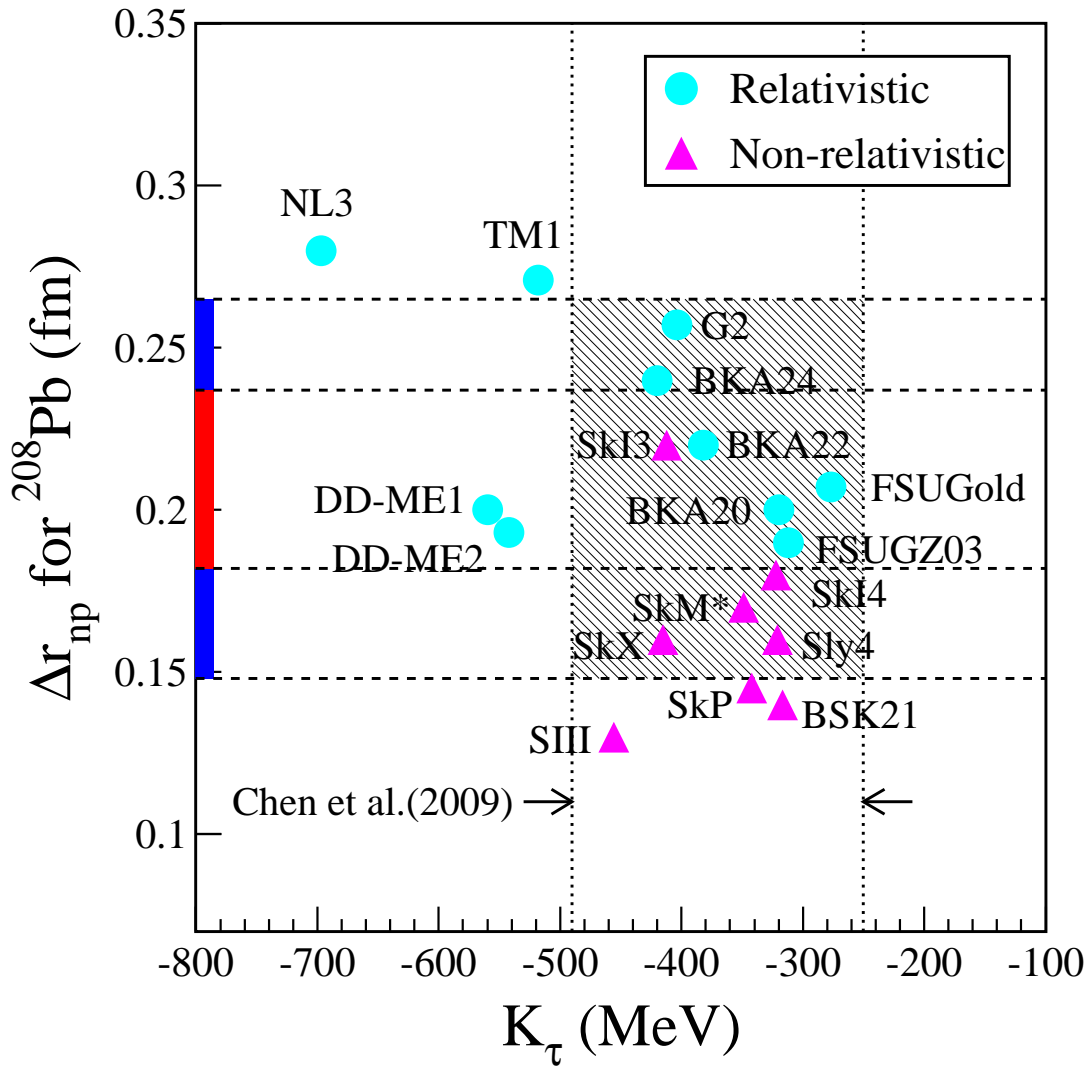


Figure 5.13: Hatched area is the constraint region on the  $K_\tau$  and  $\Delta r_{np}$  for  $^{208}\text{Pb}$  plane with several non-relativistic (triangles) and relativistic (circles) mean-field models. The constraint on  $\Delta r_{np}$  is our extracted value (blue and red lines on the y-axis), whereas on  $K_\tau$  is taken from Ref. [138].

**“Future perspectives”** Since unknown systematic errors are also included in the model uncertainties, further progress from both experiment and theory are necessary. To achieve more precise extraction of the neutron density distributions with an accuracy of less than 1% of neutron radius  $r_n$ , we need to reveal such a systematic ambiguity. Then, we need to develop both the experimental and theoretical improvements. Some clues for the improvements were also obtained from this work for lead isotopes.

- To reduce the systematic uncertainties due to the instabilities of the beam conditions just while the data is been taking, the check of the beam-line viewers is not enough. Therefore we plan to install beam position monitors (BPM), especially, cavity-BPM for on-line non-destructive monitoring. The high-quality beam is also needed.
- In the relativistic framework, Scalar density is also necessary. Since the Scalar-to-Vector ratio is changing depending on the change of the effective mass around surface region of a nucleus, we need more careful treatment of Scalar density than that of the present as the use of the constant value of  $\rho^S/\rho^V = 0.96$ .
- Coulomb potentials are now assumed to be the rigid sphere, but its effect on the scattering observables is found to be not so small. we need to modify the calculation of Coulomb potentials with the folding form of proton density distributions.
- For unstable nuclei, charge and proton density distributions are also unknown parameters, thus we need to investigate the simultaneous extraction method of proton and neutron density distributions, otherwise, to wait for other experiments such as electron scattering, isotope shift measurements. Since the sensitivity of Coulomb potentials to the scattering observables was recognized, we are examining the simultaneous extraction by using proton elastic scatterings of different incident energies, that is, different  $NN$  amplitudes.
- We will proceed the reanalyses of the obtained experimental data for lighter nuclei such as  $^{40,42,44,48}\text{Ca}$ ,  $^{16,18}\text{O}$  with several improvements to reduce systematic uncertainties as listed above. We will verify how applicable our analysis method is to extract the neutron densities of light nuclei. Particularly,  $^{48}\text{Ca}$  is expected to have a neutron skin structure. The neutron skin thickness of  $^{48}\text{Ca}$  is also important to determine the EOS parameters.

These improvements listed above are the next steps towards the precise extraction of the nucleon density distributions of various nuclei, and are now in progress.

# Chapter 6

## SUMMARY

We measured the angular distributions of cross sections and analyzing powers for polarized proton elastic scattering from  $^{58}\text{Ni}$  and  $^{204,206,208}\text{Pb}$  at  $E_p = 295$  MeV. Using the experimental data, we have extracted the neutron density distributions of  $^{204,206,208}\text{Pb}$ . In order to explain the proton elastic scattering at intermediate energies, phenomenological medium modifications were introduced into the free  $NN$  interaction with density-dependent parameters. The medium-effect parameters were determined from the experimental observables for  $^{58}\text{Ni}$ , whose nucleon density is well known. After the calibration of the effective  $NN$  interaction, we deduced the neutron density distributions of  $^{204,206,208}\text{Pb}$  in the form of a model-independent SOG distribution.

Furthermore, we have evaluated the error-envelopes of the neutron densities due to both experimental uncertainties and uncertainties associated with the various model assumptions in the medium-modified RIA by means of a new  $\chi^2$  criterion. The model ambiguity due to the theoretical assumptions, especially in use of hadronic probes, is very important to extract physical quantities. However it is very difficult to estimate such an ambiguity and hence it is usually not mentioned in many cases.

The extracted rms radius of the neutron density for  $^{208}\text{Pb}$  is consistent with past results and recent theoretical predictions such as FSUGold or BKA20 parameterization. The experimental standard errors of the neutron rms radii ( $\delta r_n^{\text{std}} \simeq 0.03$  fm) are slightly smaller than the value of Ref. [62]. Even including the model ambiguity, the estimated errors of the neutron rms radii ( $\delta r_n^{\text{mdl}} \simeq 0.06$  fm) were found to be relatively small with an accuracy of about 1 %, which is comparable or better than the estimated accuracy of the PREX experiment using parity-violating electron scattering at its present status.

We also deduced the constraint range of the symmetry energy at saturation  $\mathcal{S}(\rho_{\text{sat}})$  and the slope coefficient  $L$  of the symmetry energy corresponding to the results of the extracted neutron skin thicknesses  $\Delta r_{np}$  for  $^{204,206,208}\text{Pb}$  by using the global correlations between  $\mathcal{S}(\rho_{\text{sat}})$ ,  $L$ , and  $\Delta r_{np}$ . Since the errors including the model uncertainties are not independent among  $^{204,206,208}\text{Pb}$ , the method of the weighted average was not able to be applied to combining the three constraint ranges due to the total errors including the model uncertainties. Therefore, we obtained the combined range of  $\mathcal{S}(\rho_{\text{sat}}) = 33.0 \pm 1.1$  MeV and  $L = 67.0 \pm 12.1$  MeV, which

reflect the experimental errors of  $\Delta r_{np}$  only. The obtained ranges are very consistent with and much smaller than the previous results. However, the errors of  $S(\rho_{\text{sat}})$  and  $L$  due to the model uncertainties ( $\sim 3$  MeV and 40 MeV) are much larger than the ones due to the experimental uncertainties (1.1 MeV and 12.1 MeV). Further progress from both the experiment and theory are necessary.

# ACKNOWLEDGEMENTS

First of all, I would like to express my sincere gratitude to Prof. Harutaka Sakaguchi. He is my supervisor and has guided me from the beginning of my research career. He has continuously advised, supported, and encouraged me at every stage of this work. Discussions and talks with him have always taught me the pleasure and attitude toward physics as well as very skillful experimental technique.

I would like to thank Prof. K. Hatanaka, Prof. A. Tamii, Prof. T. Kawabata, Prof. M. Yosoi, Prof. T. Murakami, Prof. I. Tanihata, Prof. H. J. Ong, Prof. Y. Maeda, Dr. S. Terashima, Dr. Y. Matsuda, and the late Prof. H. Okamura for their support and helpful discussion regarding the present work during my research days at RCNP.

I would address my thanks to all the members of RCNP-E248 collaboration: Prof. H. Sakaguchi, Prof. T. Murakami, Prof. M. Yosoi, Dr. Y. Yasuda, Dr. S. Terashima, Mr. Y. Iwao, Dr. H. Takeda, Dr. M. Itoh, Dr. H. P. Yoshida, and Dr. M. Uchida for their grate contributions to perform this experiment successfully.

I gratefully acknowledge the continuing support of the RCNP cyclotron staff for providing the clean and stable beam.

I would like to thank Prof. K. Imai and Prof. T. Nagae for their thoughtful suggestions and encouragements.

I have spent five years as a graduate student of the experimental nuclear and hadron physics group at Kyoto University and the last three years as a researcher at the Research Center for Nuclear Physics, Osaka University. I enjoyed research activities, discussions, drinkings, recreations, and other things in the pleasant and comfortable atmosphere. I am grateful to all my colleagues and friends.

Finally, I would like to express my great thanks to my parents, brother, and grand mother for their continuous encouragement, patience, and generous affection and support.



# Appendix A

## Data table

Table A.1: Differential cross sections and analyzing powers for  $^{58}\text{Ni}(p, p)$  at  $E_p = 295$  MeV.

$\theta_{\text{c.m.}}$ (degree)	$d\sigma/d\Omega$ (mb/sr)	$\Delta(d\sigma/d\Omega)$ (mb/sr)	$A_y$	$\Delta A_y$
7.67	$1.867 \times 10^3$	$0.062 \times 10^3$	0.508	0.045
9.20	$6.474 \times 10^2$	$0.224 \times 10^2$	0.630	0.048
10.74	$1.952 \times 10^2$	$0.067 \times 10^2$	0.590	0.046
12.27	$2.194 \times 10^1$	$0.067 \times 10^1$	0.174	0.041
13.80	$1.562 \times 10^1$	$0.051 \times 10^1$	0.467	0.044
14.83	$3.263 \times 10^1$	$0.124 \times 10^1$	0.862	0.054
15.34	$3.658 \times 10^1$	$0.140 \times 10^1$	0.886	0.055
16.87	$4.174 \times 10^1$	$0.163 \times 10^1$	0.922	0.056
18.40	$3.159 \times 10^1$	$0.121 \times 10^1$	0.869	0.055
19.93	$1.652 \times 10^1$	$0.057 \times 10^1$	0.644	0.048
21.47	7.064	0.216	0.234	0.041
23.00	2.042	0.070	-0.607	0.047
24.53	1.319	0.040	-0.047	0.041
26.06	1.797	0.066	0.789	0.052
27.59	2.006	0.077	0.898	0.056
29.12	1.703	0.061	0.777	0.051

*Continued.*

$\theta_{\text{c.m.}}$ (degree)	$d\sigma/d\Omega$ (mb/sr)	$\Delta(d\sigma/d\Omega)$ (mb/sr)	$A_y$	$\Delta A_y$
30.65	1.031	0.034	0.528	0.045
32.18	$4.881 \times 10^{-1}$	$0.149 \times 10^{-1}$	0.116	0.041
33.71	$1.781 \times 10^{-1}$	$0.059 \times 10^{-1}$	-0.540	0.045
35.24	$8.786 \times 10^{-2}$	$0.289 \times 10^{-2}$	-0.492	0.045
36.77	$1.004 \times 10^{-1}$	$0.033 \times 10^{-1}$	0.470	0.044
38.29	$1.158 \times 10^{-1}$	$0.042 \times 10^{-1}$	0.763	0.051
39.82	$1.007 \times 10^{-1}$	$0.036 \times 10^{-1}$	0.749	0.051
41.35	$6.607 \times 10^{-2}$	$0.229 \times 10^{-2}$	0.652	0.048
42.87	$3.169 \times 10^{-2}$	$0.102 \times 10^{-2}$	0.428	0.043
44.40	$1.113 \times 10^{-2}$	$0.034 \times 10^{-2}$	0.012	0.041
45.92	$3.274 \times 10^{-3}$	$0.118 \times 10^{-3}$	-0.649	0.050
47.44	$3.275 \times 10^{-3}$	$0.137 \times 10^{-3}$	0.365	0.044
48.97	$4.929 \times 10^{-3}$	$0.226 \times 10^{-3}$	0.786	0.052

Table A.2: Differential cross sections and analyzing powers for  $^{204}\text{Pb}(p, p)$  at  $E_p = 295$  MeV.

$\theta_{\text{c.m.}}$ (degree)	$d\sigma/d\Omega$ (mb/sr)	$\Delta(d\sigma/d\Omega)$ (mb/sr)	$A_y$	$\Delta A_y$
7.55	$1.540 \times 10^3$	$0.063 \times 10^3$	0.325	0.042
9.06	$5.709 \times 10^2$	$0.255 \times 10^2$	0.666	0.049
10.57	$6.785 \times 10^2$	$0.240 \times 10^2$	0.680	0.048
12.08	$3.526 \times 10^2$	$0.130 \times 10^2$	0.793	0.052
13.59	$9.619 \times 10^1$	$0.349 \times 10^1$	0.757	0.050
14.59	$1.991 \times 10^1$	$0.071 \times 10^1$	0.672	0.048
15.10	$1.919 \times 10^1$	$0.069 \times 10^1$	0.705	0.049
16.61	$4.882 \times 10^1$	$0.192 \times 10^1$	0.937	0.057
18.11	$4.339 \times 10^1$	$0.171 \times 10^1$	0.936	0.057
19.62	$1.575 \times 10^1$	$0.055 \times 10^1$	0.646	0.048
21.13	4.166	0.128	-0.159	0.041
22.64	5.049	0.178	0.671	0.048
24.15	6.383	0.244	0.874	0.055
25.66	4.131	0.150	0.645	0.048
27.17	1.463	0.044	-0.035	0.040
28.68	$6.671 \times 10^{-1}$	$0.210 \times 10^{-1}$	-0.227	0.042
30.19	$9.571 \times 10^{-1}$	$0.338 \times 10^{-1}$	0.698	0.049
31.69	$8.870 \times 10^{-1}$	$0.351 \times 10^{-1}$	0.690	0.056
33.20	$4.427 \times 10^{-1}$	$0.139 \times 10^{-1}$	0.322	0.042
34.71	$1.355 \times 10^{-1}$	$0.044 \times 10^{-1}$	-0.455	0.044
36.22	$1.187 \times 10^{-1}$	$0.037 \times 10^{-1}$	0.284	0.042
37.73	$1.551 \times 10^{-1}$	$0.060 \times 10^{-1}$	0.660	0.053
39.23	$1.089 \times 10^{-1}$	$0.037 \times 10^{-1}$	0.583	0.046
40.74	$3.929 \times 10^{-2}$	$0.121 \times 10^{-1}$	0.109	0.041
42.25	$1.234 \times 10^{-2}$	$0.040 \times 10^{-2}$	-0.337	0.043

*Continued.*

*Continued.*

$\theta_{c.m.}$ (degree)	$d\sigma/d\Omega$ (mb/sr)	$\Delta(d\sigma/d\Omega)$ (mb/sr)	$A_y$	$\Delta A_y$
43.76	$1.767 \times 10^{-2}$	$0.061 \times 10^{-2}$	0.600	0.047
45.26	$1.993 \times 10^{-2}$	$0.072 \times 10^{-2}$	0.741	0.051
46.77	$1.104 \times 10^{-2}$	$0.038 \times 10^{-2}$	0.573	0.047
48.28	$2.959 \times 10^{-3}$	$0.104 \times 10^{-3}$	0.034	0.047

Table A.3: Differential cross sections and analyzing powers for  $^{206}\text{Pb}(p, p)$  at  $E_p = 295$  MeV.

$\theta_{\text{c.m.}}$ (degree)	$d\sigma/d\Omega$ (mb/sr)	$\Delta(d\sigma/d\Omega)$ (mb/sr)	$A_y$	$\Delta A_y$
7.55	$1.537 \times 10^3$	$0.063 \times 10^3$	0.326	0.042
9.06	$5.931 \times 10^2$	$0.265 \times 10^2$	0.640	0.049
10.57	$6.977 \times 10^2$	$0.247 \times 10^2$	0.675	0.048
12.08	$3.507 \times 10^2$	$0.129 \times 10^2$	0.796	0.052
13.59	$9.188 \times 10^1$	$0.334 \times 10^1$	0.754	0.050
14.59	$1.987 \times 10^1$	$0.071 \times 10^1$	0.668	0.048
15.10	$2.002 \times 10^1$	$0.073 \times 10^1$	0.726	0.050
16.60	$5.120 \times 10^1$	$0.201 \times 10^1$	0.936	0.057
18.11	$4.439 \times 10^1$	$0.175 \times 10^1$	0.935	0.057
19.62	$1.523 \times 10^1$	$0.053 \times 10^1$	0.635	0.048
21.13	4.045	0.125	-0.194	0.041
22.64	5.461	0.195	0.696	0.049
24.15	6.504	0.250	0.877	0.055
25.66	4.052	0.145	0.624	0.048
27.17	1.398	0.042	-0.093	0.041
28.68	$6.926 \times 10^{-1}$	$0.214 \times 10^{-1}$	-0.143	0.050
30.18	$9.901 \times 10^{-1}$	$0.353 \times 10^{-1}$	0.721	0.050
31.69	$8.747 \times 10^{-1}$	$0.343 \times 10^{-1}$	0.671	0.055
33.20	$4.154 \times 10^{-1}$	$0.129 \times 10^{-1}$	0.271	0.041
34.71	$1.279 \times 10^{-1}$	$0.043 \times 10^{-1}$	-0.494	0.045
36.22	$1.267 \times 10^{-1}$	$0.040 \times 10^{-1}$	0.365	0.043
37.72	$1.577 \times 10^{-1}$	$0.059 \times 10^{-1}$	0.702	0.052
39.23	$1.047 \times 10^{-1}$	$0.035 \times 10^{-1}$	0.544	0.046
40.74	$3.580 \times 10^{-2}$	$0.111 \times 10^{-2}$	0.026	0.041
42.25	$1.277 \times 10^{-2}$	$0.041 \times 10^{-2}$	-0.263	0.043

*Continued.*

*Continued.*

$\theta_{\text{c.m.}}$ (degree)	$d\sigma/d\Omega$ (mb/sr)	$\Delta(d\sigma/d\Omega)$ (mb/sr)	$A_y$	$\Delta A_y$
43.75	$1.947 \times 10^{-2}$	$0.069 \times 10^{-2}$	0.634	0.048
45.26	$2.037 \times 10^{-2}$	$0.074 \times 10^{-2}$	0.727	0.051
46.77	$1.041 \times 10^{-2}$	$0.035 \times 10^{-2}$	0.520	0.046
48.27	$2.449 \times 10^{-3}$	$0.095 \times 10^{-3}$	-0.070	0.052

Table A.4: Differential cross sections and analyzing powers for  $^{208}\text{Pb}(p, p)$  at  $E_p = 295$  MeV.

$\theta_{\text{c.m.}}$ (degree)	$d\sigma/d\Omega$ (mb/sr)	$\Delta(d\sigma/d\Omega)$ (mb/sr)	$A_y$	$\Delta A_y$
7.55	$1.580 \times 10^3$	$0.065 \times 10^3$	0.326	0.042
9.06	$5.958 \times 10^2$	$0.262 \times 10^2$	0.626	0.048
10.57	$7.352 \times 10^2$	$0.260 \times 10^2$	0.683	0.048
12.08	$3.521 \times 10^2$	$0.130 \times 10^2$	0.797	0.052
13.59	$9.086 \times 10^1$	$0.329 \times 10^1$	0.752	0.050
14.59	$2.002 \times 10^1$	$0.071 \times 10^1$	0.692	0.049
15.09	$2.148 \times 10^1$	$0.078 \times 10^1$	0.741	0.050
16.60	$5.260 \times 10^1$	$0.206 \times 10^1$	0.935	0.057
18.11	$4.444 \times 10^1$	$0.175 \times 10^1$	0.933	0.057
19.62	$1.467 \times 10^1$	$0.050 \times 10^1$	0.606	0.047
21.13	4.045	0.125	-0.181	0.041
22.64	5.610	0.202	0.730	0.050
24.15	6.541	0.250	0.868	0.055
25.66	3.861	0.135	0.593	0.047
27.17	1.329	0.040	-0.138	0.041
28.67	$7.050 \times 10^{-1}$	$0.215 \times 10^{-1}$	-0.056	0.047
30.18	$9.840 \times 10^{-1}$	$0.352 \times 10^{-1}$	0.736	0.050
31.69	$8.396 \times 10^{-1}$	$0.326 \times 10^{-1}$	0.653	0.054
33.20	$3.825 \times 10^{-1}$	$0.118 \times 10^{-1}$	0.220	0.041
34.71	$1.196 \times 10^{-1}$	$0.039 \times 10^{-1}$	-0.481	0.045
36.21	$1.279 \times 10^{-1}$	$0.041 \times 10^{-1}$	0.432	0.044
37.72	$1.512 \times 10^{-1}$	$0.058 \times 10^{-1}$	0.695	0.052
39.23	$9.577 \times 10^{-2}$	$0.319 \times 10^{-2}$	0.511	0.045
40.74	$3.064 \times 10^{-2}$	$0.094 \times 10^{-2}$	-0.013	0.041
42.24	$1.287 \times 10^{-2}$	$0.040 \times 10^{-2}$	-0.097	0.042

*Continued.*

*Continued.*

$\theta_{c.m.}$ (degree)	$d\sigma/d\Omega$ (mb/sr)	$\Delta(d\sigma/d\Omega)$ (mb/sr)	$A_y$	$\Delta A_y$
43.75	$2.019 \times 10^{-2}$	$0.071 \times 10^{-2}$	0.651	0.048
45.26	$1.974 \times 10^{-2}$	$0.071 \times 10^{-2}$	0.711	0.050
46.76	$9.180 \times 10^{-3}$	$0.306 \times 10^{-3}$	0.470	0.045
48.27	$2.053 \times 10^{-3}$	$0.078 \times 10^{-3}$	-0.141	0.051

# Appendix B

## Relativistic impulse approximation

The analysis method to describe the reaction is essentially based on the framework of the relativistic impulse approximation (RIA) with the relativistic Love-Franey (RLF) interaction developed by Murdock and Horowitz (MH model) [88–90]. In this appendix, we review the framework and formalism used in the MH model.

Since 1980s, after the success of Dirac phenomenology to explain the scattering observables, especially, polarization observables, the original RIA approach has been developed with the microscopic description by McNeil, Ray, and Wallace [143] (MRW model). In the original RIA, the experimental  $NN$  scattering amplitude is represented by a particular set of five Lorentz covariant functions (Eq. (4.1)), as mentioned in Chap. 4.1.1. The functions are then folded with the target nucleus densities to produce a first-order  $t\rho$  optical potentials. This expression  $\mathcal{F}$  of five Lorentz covariant functions is an approximated form by using an analogy from the empirical amplitude, which is conventionally expressed in terms of the nonrelativistic Wolfenstein amplitudes with the Pauli matrices [143].

However, the general expression of  $\mathcal{F}$  in the two-particle Dirac space involves 44 components of Lorentz covariants under the isospin and CPT invariance. Thus the only five functions described in Eq. (4.1) is not sufficient to specify  $\mathcal{F}$ , i.e., to determine the negative energy matrix elements uniquely. Thus there are nontrivial assumptions involved in using Eq. (4.1) to calculate the optical potential. In addition, the original RIA procedure does not separate the direct and exchange contributions to the amplitudes. These contributions have different characteristic dependence on the momentum transfer and energy, especially at low energies. The original RIA model assumes that the  $NN$  interaction is unmodified by the surrounding nuclear medium such as inside a nucleus. While this assumption is valid at high energies, the modifications from nuclear medium such as Pauli blocking are not negligible at lower intermediate energy regions.

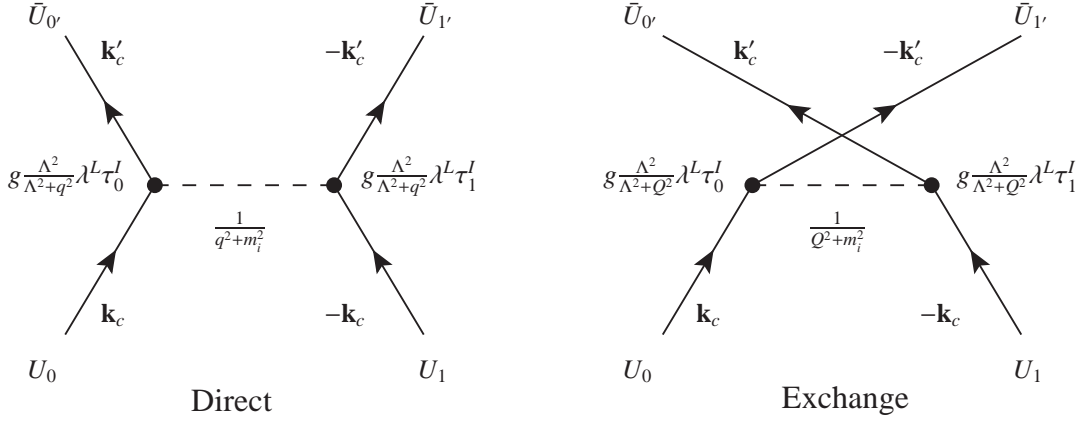


Figure B.1: Meson exchange diagrams for the relativistic Love-Franey model.

**“Relativistic Love-Franey  $NN$  interaction”** On the basis of this original form of the  $NN$  amplitude, the RLF  $NN$  interaction was further developed by Horowitz [88] to improve the problems listed above.

The  $NN$  amplitude is modeled as arising from the first Born approximation for the exchange of a set of mesons. The parameters of the mesons were fitted to reproduce  $NN$  scattering data at several energies. From direct and exchange Feynman diagrams in Fig. B.1, the  $NN$  amplitude for each meson is calculated straightforward. The  $NN$ -meson vertex factor from the Feynman rules is assumed to be

$$g_i \left( \frac{\Lambda_i^2}{\mathbf{q}^2 + \Lambda_i^2} \right) \lambda^{L(i)}(\boldsymbol{\tau})^{I_i}, \quad (\text{B.1})$$

where  $L(i)$  denotes the Lorentz type of the  $i$ th meson listed in Table. B.1 and  $I_i$  is its isospin (0 or 1). Then, each Lorentz invariant  $\mathcal{F}^L$  ( $L = S, V, PS, T$ , or  $A$ ) can be written as

$$\mathcal{F}^L(q, E_c) = i \frac{M^2}{2E_c k_c} [F_D^L(q) + F_X^L(Q)], \quad (\text{B.2})$$

$$F_D^L(q) \equiv \sum_i \delta_{L,L(i)} \{\boldsymbol{\tau}_0 \cdot \boldsymbol{\tau}_1\}^{I_i} f^i(q), \quad (\text{B.3})$$

$$F_X^L(Q) \equiv (-1)^T \sum_i B_{L(i),L} \{\boldsymbol{\tau}_0 \cdot \boldsymbol{\tau}_1\}^{I_i} f^i(Q), \quad (\text{B.4})$$

$$f^i(q) \equiv \frac{g_i^2}{\mathbf{q}^2 + m_i^2} \left( \frac{\Lambda_i^2}{\Lambda_i^2 + \mathbf{q}^2} \right)^2 - i \frac{\bar{g}_i^2}{\mathbf{q}^2 + \bar{m}_i^2} \left( \frac{\bar{\Lambda}_i^2}{\bar{\Lambda}_i^2 + \mathbf{q}^2} \right)^2, \quad (\text{B.5})$$

where  $D$  and  $X$  denote the direct and exchange terms as shown in Fig. B.1,  $q$  and  $Q$  are direct and exchange three-momentum transfers.  $E_c$  and  $k_c$  are the total energy and relative momentum in the nucleon-nucleon cm system.  $B_{L(i),L}$  is the  $(L(i), L)$  component of the Fierz

Table B.1: Dirac matrix types

$L$	$\lambda^L$
$S$ (scalar)	1
$V$ (vector)	$\gamma_\mu$
$PS$ (pseudoscalar)	$\gamma_5$
$A$ (axial-vector)	$\gamma_5\gamma_\mu$
$T$ (tensor)	$\sigma_{\mu\nu}$

transformation matrix:

$$B_{L,L'} = \frac{\text{Tr}(\lambda^L \lambda^{L'} \lambda^L \lambda^{L'})}{[\text{Tr}(\lambda^{L'} \lambda^L)]^2}, \quad (\text{B.6})$$

$$= \frac{1}{8} \begin{pmatrix} 2 & 2 & 1 & -2 & 2 \\ 8 & -4 & 0 & -4 & -8 \\ 24 & 0 & -4 & 0 & 24 \\ -8 & -4 & 0 & -4 & 8 \\ 2 & -2 & 1 & 2 & 2 \end{pmatrix} \begin{pmatrix} S \\ V \\ T \\ A \\ PS \end{pmatrix}. \quad (\text{B.7})$$

The coupling constant, mass and cut-off parameter for  $i$ -th meson denoted by  $g_i$ ,  $m_i$ , and  $\Lambda_i$  are fitted to the free  $NN$  amplitudes at several different laboratory energies [88]. The full set of parameters can be found in Ref. [88, 89].  $T$  is the total isospin of the two-nucleon system, thus

$$F^L(pp) = F^L(T = 1), \quad (\text{B.8})$$

$$F^L(pn) = \frac{1}{2} [F^L(T = 0) + F^L(T = 1)], \quad (\text{B.9})$$

are used to get  $pp$  and  $pn$  scattering amplitudes, respectively.

The form of  $NN$  amplitudes in Eq. (4.1) is completely local. No factors of a momentum dotted into a gamma matrix appear explicitly. However, as the energy is decreased, the  $NN$  amplitudes cannot neglect the exchange nonlocalities implied by a pion with pseudovector coupling. It is known that the pseudoscalar term of Eq. (4.1) should be replaced by the pseudovector invariant

$$\mathcal{F}^{PS} \gamma_{(0)}^5 \gamma_{(1)}^5 \rightarrow -\mathcal{F}^{PV} \not{q} \gamma_{(0)}^5 \not{q} \gamma_{(1)}^5. \quad (\text{B.10})$$

to give meaningful results at lower energies. Note that this is not a exact medium modification different from such a Pauli blocking effect.

“ $t\rho$  optical potential in the MH model” The first-order Dirac optical potentials for the spherical nuclei are produced by folding  $NN$  amplitude with the target densities:

$$U^L(r; E) = U_D^L(r; E) + U_X^L(r; E), \quad (\text{B.11})$$

$$U_D^L(r; E) \equiv -\frac{4\pi ip}{M} \int d\mathbf{r}' \rho^L(\mathbf{r}') t_D^L(|\mathbf{r}' - \mathbf{r}|; E), \quad (\text{B.12})$$

$$U_X^L(r; E) \equiv -\frac{4\pi ip}{M} \int d\mathbf{r}' \rho^L(\mathbf{r}', \mathbf{r}) t_X^L(|\mathbf{r}' - \mathbf{r}|; E) j_0(p|\mathbf{r}' - \mathbf{r}|), \quad (\text{B.13})$$

where  $t_D^L(|\mathbf{r}|; E)$  are Fourier transforms of  $t_D^L(\mathbf{q}; E) \equiv (iM^2/2E_c k_c) F_D^L(\mathbf{q})$  and similarly for the exchange pieces  $t_X^L(\mathbf{Q}; E)$ . The nuclear densities  $\rho^L(\mathbf{r})$  are expressed as sums over the occupied nuclear levels:

$$\rho^L(\mathbf{r}', \mathbf{r}) \equiv \sum_{\alpha}^{\text{occ}} \bar{\mathcal{U}}_{\alpha}(\mathbf{r}') \lambda^L \mathcal{U}_{\alpha}(\mathbf{r}), \quad (\text{B.14})$$

where  $\mathcal{U}_{\alpha}$  is a single particle four-component wave function in state  $\alpha$ , and the relativistic Hartree approximation is applied to obtain  $\mathcal{U}_{\alpha}$ . For the exchange term, non-local densities  $\rho^L(\mathbf{r}', \mathbf{r})$  are approximated as

$$\rho^L(\mathbf{r}', \mathbf{r}) \approx \rho^L\left(\frac{1}{2}(\mathbf{r}' + \mathbf{r})\right) \left(\frac{3}{|\mathbf{r}' - \mathbf{r}| k_F}\right) j_1(|\mathbf{r}' - \mathbf{r}| k_F), \quad (\text{B.15})$$

where  $\rho^V((\mathbf{r}' - \mathbf{r}/2)) = 2k_F^3/3\pi^2$ .

For a spin-zero nucleus, the only nonzero densities are scalar, vector, and tensor densities with  $\lambda^T = \sigma^{0i}$  in Eq. (B.14). The optical potential takes the form

$$U_{\text{opt}} = U^S + \gamma^0 U^V - 2i\boldsymbol{\alpha} \cdot \hat{\mathbf{r}} U^T. \quad (\text{B.16})$$

The tensor contribution is found to be small and will be negligible. Thus the optical potential has only scalar and vector contributions.

For laboratory energy around 200 MeV, it is necessary to correct the optical potentials for medium modifications from Pauli blocking. These can be approximated by performing a Dirac-Brueckner calculation with a local-density approximation as follows:

$$U^L(r; E) \rightarrow \left[ 1 - a(E) \left( \frac{\rho^V(r)}{\rho_0} \right)^{2/3} \right] U^L(r; E). \quad (\text{B.17})$$

where  $\rho_0 = 0.1934 \text{ fm}^{-3}$ . In the present work, we have further modified the RLF  $NN$  interaction with the density-dependent terms described as Eqs. (4.4), (4.5) to explain the various medium effects. Since the Pauli blocking effect is also included to our modification, we have not used the correction of Eq. B.17 introduced by Horowitz.

The Dirac equation for the projectile is finally expressed as

$$\left\{ -i\boldsymbol{\alpha} \cdot \boldsymbol{\nabla} + U^V(r; E) + \beta \left[ M + U^S(r; E) \right] \right\} \mathcal{U}_0(\mathbf{r}) = E \mathcal{U}_0(\mathbf{r}), \quad (\text{B.18})$$

where  $E$  is the total nucleon-nucleus center-of-mass projectile energy,  $M$  is its rest mass, and  $\mathcal{U}_0$  is the incident projectile wave function. Note that the Coulomb potential is included in  $U^V$ . The Coulomb potential used in this model is assumed to be a uniform spherical charge distribution of radius  $R = r_0 A^{1/3}$ , where  $r_0 \approx 1.25$  fm.

To solve the Dirac equation of Eq. (B.18), in the calculations of the MH model the wave function is first separated into its upper and lower two-component wave functions and the Dirac equations rewritten as two coupled, first-order differential equations:

$$\begin{cases} (\boldsymbol{\sigma} \cdot \mathbf{p})v_0(\mathbf{r}) + (U^V + M + U^S)u_0(\mathbf{r}) = Eu_0(\mathbf{r}) \\ (\boldsymbol{\sigma} \cdot \mathbf{p})u_0(\mathbf{r}) + (U^V - M - U^S)v_0(\mathbf{r}) = Ev_0(\mathbf{r}) \end{cases}, \quad (\text{B.19})$$

$$\mathcal{U}_0(\mathbf{r}) = \begin{pmatrix} u_0(\mathbf{r}) \\ v_0(\mathbf{r}) \end{pmatrix}, \alpha^i = \gamma^0 \gamma^i \begin{pmatrix} 0 & \sigma^i \\ \sigma^i & 0 \end{pmatrix}, \beta = \gamma^0 \begin{pmatrix} 1 & 0 \\ 0 & -1 \end{pmatrix}. \quad (\text{B.20})$$

The lower component  $v_0$  is then eliminated, leading to a single second-order differential equation for the upper components. At this moment this equation contains local, spin-orbit, and nonlocal Darwin potentials, but the nonlocality can be removed by rewriting the upper wave function as

$$u_0(\mathbf{r}) \equiv \mathcal{A}^{1/2}(r; E)\chi_0(\mathbf{r}), \quad (\text{B.21})$$

$$\mathcal{A}(r; E) \equiv 1 + \frac{U^S(r; E) - U^V(r; E)}{E + M}. \quad (\text{B.22})$$

Then the equation for the new two-component function  $\chi_0(\mathbf{r})$ , that is, Schrödinger-like equation becomes

$$(-\nabla^2 + V_c + V_{\text{so}}\boldsymbol{\sigma} \cdot \mathbf{l} + V_{\text{Darwin}})\chi_0(\mathbf{r}) = (E^2 - M^2)\chi_0(\mathbf{r}), \quad (\text{B.23})$$

where the nonrelativistic energy-dependent optical potentials are

$$V_c(r; E) \equiv 2MU^S + 2EU^V + (U^S)^2 - (U^V)^2, \quad (\text{B.24})$$

$$V_{\text{so}}(r; E) \equiv -\frac{1}{r\mathcal{A}} \frac{\partial \mathcal{A}}{\partial r}, \quad (\text{B.25})$$

$$V_{\text{Darwin}}(r; E) \equiv -\frac{1}{2r^2\mathcal{A}} \frac{\partial}{\partial r} \left( r^2 \frac{\partial \mathcal{A}}{\partial r} \right) + \frac{3}{4\mathcal{A}^2} \left( \frac{\partial \mathcal{A}}{\partial r} \right)^2. \quad (\text{B.26})$$



# Appendix C

## Equation of state of nuclear matter

**Liquid drop model** The study to understand the many-body properties of nuclei or nuclear matter has started since 1930s by Bethe and von-Weizsäcker [144, 145] who developed the macroscopic semi-empirical mass formula of nuclei using the liquid-drop model (LDM):

$$E(N, Z) = -a_V A + a_S A^{2/3} B_{\text{surf}} + a_C \frac{Z^2}{A^{1/3}} B_{\text{Coul}}, \quad (\text{C.1})$$

$$a_V = a_1(1 - \kappa_V I^2), \quad (\text{C.2})$$

$$a_S = a_2(1 - \kappa_S I^2), \quad (\text{C.3})$$

where  $A = N + Z$ , the assumptions has been made that the nuclear matter in the interior is uniform and incompressible so that the radius of a spherical nucleus is proportional to  $A^{1/3}$ .  $a_1$  is the binding energy of symmetric nuclear matter and  $I = (N - Z)/A$ . The term  $\kappa_V$  proportional to  $I^2$  is included in order to describe the dependence of the bulk binding energy on the neutron excess, but Eq. (C.2) in the simple form has no shape dependence. Eq. (C.3) is the surface energy term, which is analogy to Eq. (C.2).  $B_{\text{surf}}$  and  $B_{\text{Coul}}$  are the factors related to the nuclear deformation.

**Droplet model** One specific approach to extending the LDM is called the droplet model (DM). Myers and Swiatecki [146–148] developed the LDM model, which is extended to one higher order in the expansion parameters  $A^{-1/3}$  and  $I^2$ . Different from LDM, the extensions includes the general expression of nuclear incompressibility and density distributions. The energy by DM is expressed as

$$\begin{aligned} E(N, Z; \text{shape}) = & \left[ -a_1 + J\bar{\delta}^2 - \frac{1}{2}K\bar{\epsilon}^2 + \frac{1}{2}M\bar{\delta}^4 \right] A + \left[ a_2 + \frac{9}{4}\frac{J^2}{Q}\bar{\delta}^2 \right] A^{2/3} B_{\text{surf}} \\ & + a_3 A^{1/3} B_{\text{curv}} + c_1 Z^2 A^{-1/3} B_{\text{Coul}} - c_2 Z^2 A^{1/3} B_{\text{red}} \\ & - c_5 Z^2 B_{\text{W}} - c_3 Z^2 A^{-1} - c_4 Z^{4/3} A^{-1/3}, \end{aligned} \quad (\text{C.4})$$

where

$$\bar{\delta} = \frac{I + \frac{3}{16} \frac{c_1}{Q} Z A^{-2/3} B_V}{1 + \frac{9}{4} \frac{J}{Q} A^{-1/3} B_{\text{surf}}}, \quad (\text{C.5})$$

$$\bar{\epsilon} = [-2a_2 A^{-1/3} B_{\text{surf}} + L \bar{\delta}^2 + c_1 Z^2 A^{-4/3} B_{\text{Coul}}]/K, \quad (\text{C.6})$$

and the constants  $c_i$  ( $i = 1, 2, 3, 4, 5$ ) are

$$\begin{aligned} c_1 &= \frac{3}{5} \frac{e^2}{r_0}, \quad c_2 = \frac{c_1^2}{336} \left( \frac{1}{J} + \frac{18}{K} \right), \\ c_3 &= \frac{5}{2} c_1 \left( \frac{b}{r_0} \right)^2, \quad c_4 = \frac{5}{4} c_1 \left( \frac{3}{2\pi} \right)^{2/3}, \\ c_5 &= \frac{1}{64} \frac{c_1^2}{Q}. \end{aligned} \quad (\text{C.7})$$

The quantities  $B_{\text{curv}}$ ,  $B_{\text{red}}$ ,  $B_V$  and  $B_W$  are the curvature correction to the surface energy, the interior and surface corrections due to the Coulomb forces, respectively. The coefficients  $J$ ,  $Q$ , and  $r_0$  in Eq. (C.4) are analogous to the LDM coefficients  $\kappa_V$ ,  $\kappa_S$ , and  $a_C$  of Eq. (C.1). Three new coefficients  $K$ ,  $L$ , and  $M$  are the incompressibility, the dependence of the incompressibility on neutron excess, and the higher order coefficient in asymmetry  $I$ , respectively.

**Mean field approach** In the late 1960s, microscopic theoretical studies of the nuclear many-body system were pioneered by Brueckner *et al.* [149]. Since then, many theoretical models such as the microscopic many-body approach, the effective-field theory, and the phenomenological mean-field approach, have been developed by using various bare or effective, two-body or three-body interactions.

The phenomenological approach, in particular, the Skyrme-Hartree-Fock and the relativistic mean-field models are the most successful approaches to describe the macroscopic properties of finite nuclei and/or nuclear matter. In these theoretical approaches, the energy per nucleon of infinite nuclear matter is also described as a function of the density  $\rho$  and isospin asymmetry  $\delta$  in an analogous fashion to LDM or DM expression. It can be expanded in a series of  $\delta$  as

$$\frac{E}{A}(\rho, \delta) \equiv \mathcal{E}(\rho, \delta) = \mathcal{E}_0(\rho) + \mathcal{S}_2(\rho)\delta^2 + \mathcal{S}_4(\rho)\delta^4 + \mathcal{O}(\delta^6) \quad (\text{C.8})$$

$$\mathcal{E}_0(\rho) = \mathcal{E}(\rho, 0) \quad (\text{C.9})$$

$$\mathcal{S}_2(\rho) = \frac{1}{2!} \left. \frac{\partial^2 \mathcal{E}(\rho, \delta)}{\partial \delta^2} \right|_{\delta=0} \quad (\text{C.10})$$

$$\mathcal{S}_4(\rho) = \frac{1}{4!} \left. \frac{\partial^4 \mathcal{E}(\rho, \delta)}{\partial \delta^4} \right|_{\delta=0}. \quad (\text{C.11})$$

where  $\mathcal{E}_0(\rho)$  is the energy per nucleon of symmetric nuclear matter. The second-order term  $\mathcal{S}_2(\rho) \equiv \mathcal{S}(\rho)$  is known as the so-called nuclear symmetry energy. The higher-order  $\mathcal{O}(\delta^4)$

terms are very small and often neglected. Therefore, the energy per nucleon of pure neutron matter ( $\delta = 1$ ) is approximately written as

$$\mathcal{E}(\rho, 1) \approx \mathcal{E}(\rho, 0) + \mathcal{S}(\rho). \quad (\text{C.12})$$

In order to understand the properties of the pure neutron matter such as a neutron star, we first need to know the EOS of symmetric nuclear matter and the symmetry energy.

The symmetric EOS  $\mathcal{E}_0(\rho)$  around the saturation can be characterized by an equilibrium density of  $\rho_{\text{sat}} \simeq 0.15 \text{ fm}^{-3}$ , an energy per nucleon of  $\mathcal{E}_0 \equiv \mathcal{E}_0(\rho_{\text{sat}}) \simeq -16 \text{ MeV}$ , and a pressure of  $P = \rho^2 d\mathcal{E}_0/d\rho = 0$ . Thus, the symmetric EOS  $\mathcal{E}_0(\rho)$  around the saturation density is expanded up to the fourth-order in density as

$$\mathcal{E}_0(\rho) = \mathcal{E}_0 + \frac{K_0}{2!}\epsilon^2 + \frac{J_0}{3!}\epsilon^3 + \frac{I_0}{4!}\epsilon^4 + \mathcal{O}(\epsilon^5), \quad (\text{C.13})$$

where  $\epsilon = (\rho - \rho_{\text{sat}}/3\rho_{\text{sat}})$  and the first-order coefficient of  $\epsilon$  vanishes at saturation defined by  $P = 0$ . The coefficient  $K_0$  is the so-called incompressibility of symmetric nuclear matter.

The symmetry energy  $\mathcal{S}(\rho)$  and the fourth-order coefficient  $\mathcal{S}_4(\rho)$  in Eq. (C.8) are similarly expanded around the saturation density as

$$\mathcal{S}(\rho) = \mathcal{S}(\rho_{\text{sat}}) + L_{\text{sym}}\epsilon + \frac{K_{\text{sym}}}{2!}\epsilon^2 + \frac{J_{\text{sym}}}{3!}\epsilon^3 + \frac{I_{\text{sym}}}{4!}\epsilon^4 + \mathcal{O}(\epsilon^5) \quad (\text{C.14})$$

$$\mathcal{S}_4(\rho) = \mathcal{S}_4(\rho_{\text{sat}}) + L_{\text{sym},4}\epsilon + \frac{K_{\text{sym},4}}{2!}\epsilon^2 + \frac{J_{\text{sym},4}}{3!}\epsilon^3 + \frac{I_{\text{sym},4}}{4!}\epsilon^4 + \mathcal{O}(\epsilon^5), \quad (\text{C.15})$$

where  $L_{\text{sym}(,4)}$ ,  $K_{\text{sym}(,4)}$ ,  $J_{\text{sym}(,4)}$ , and  $I_{\text{sym}(,4)}$  are the slope, curvature, third-order, and fourth-order coefficient of symmetry energy  $\mathcal{S}(\rho)$  ( $\mathcal{S}_4(\rho)$ ). The pressure of symmetry energy  $L_{\text{sym}}$ , which is strongly correlated with the neutron skin thickness of heavy asymmetric nuclei, does not vanish unlike the symmetric EOS.

The coefficients in Eqs. (C.13), (C.14), and (C.15), namely,  $\mathcal{E}_0$ ,  $K_0$ ,  $J_0$ ,  $I_0$ ,  $\mathcal{S}(\rho_{\text{sat}})$ ,  $L_{\text{sym}}$ ,  $K_{\text{sym}}$ ,  $J_{\text{sym}}$ ,  $I_{\text{sym}}$ ,  $\mathcal{S}_4(\rho_{\text{sat}})$ ,  $L_{\text{sym},4}$ ,  $K_{\text{sym},4}$ ,  $J_{\text{sym},4}$ , and  $I_{\text{sym},4}$ , characterize the EOS of asymmetric nuclear matter, especially, its density dependence around the saturation density. Among these coefficients,  $\mathcal{E}_0$ ,  $K_0$ , and  $\mathcal{S}(\rho_{\text{sat}})$  have been well understood from recent theoretical and experimental studies. However, others are still less certain and their predictions widely differ among many mean-field models.

**Isospin dependence of saturation properties** By using these coefficients, the evolution of the saturation properties such as the saturation density, the binding energy per nucleon, and the incompressibility can be described as a function of the isospin asymmetry  $\delta$ . The saturation point is defined as

$$\left. \frac{\partial \mathcal{E}(\rho, \delta)}{\partial \rho} \right|_{\rho=\rho_{\text{sat}}(\delta)} = 0, \quad (\text{C.16})$$

where the saturation density  $\rho_{\text{sat}}(\delta)$  is derived from Eqs. (C.8), (C.13), (C.14), (C.15):

$$\rho_{\text{sat}}(\delta) = \left[ 1 - \frac{3L_{\text{sym}}}{K_0} \delta^2 + \left( \frac{3K_{\text{sym}}L_{\text{sym}}}{K_0^2} - \frac{3L_{\text{sym},4}}{K_0} - \frac{3J_0L_{\text{sym}}^2}{2K_0^3} \right) \delta^4 + \mathcal{O}(\delta^6) \right] \rho_{\text{sat},0}, \quad (\text{C.17})$$

where  $\rho_{\text{sat},0}$  is redefined as the saturation density of symmetric nuclear matter. The binding energy per nucleon at saturation density  $\mathcal{E}_{\text{sat}}(\delta) \equiv \mathcal{E}(\rho_{\text{sat}}(\delta), \delta)$  is also expressed up to fourth order in  $\delta$  as

$$\mathcal{E}_{\text{sat}}(\delta) = \mathcal{E}_0 + \mathcal{S}(\rho_{\text{sat},0})\delta^2 + \left( \mathcal{S}_4(\rho_{\text{sat},0}) - \frac{L_{\text{sym}}^2}{2K_0} \right) \delta^4 + \mathcal{O}(\delta^6). \quad (\text{C.18})$$

The incompressibility of asymmetric nuclear matter is generally defined as

$$\begin{aligned} K(\rho, \delta) &= 9 \frac{\partial P(\rho, \delta)}{\partial \rho} \\ &= 18\rho \frac{\partial \mathcal{E}(\rho, \delta)}{\partial \rho} + 9\rho^2 \frac{\partial^2 \mathcal{E}(\rho, \delta)}{\partial \delta^2} \\ &= 18 \frac{P(\rho, \delta)}{\rho} + 9\rho^2 \frac{\partial^2 \mathcal{E}(\rho, \delta)}{\partial \delta^2}, \end{aligned} \quad (\text{C.19})$$

where  $P(\rho, \delta)$  is the pressure of asymmetric nuclear matter and can be expressed as

$$P(\rho, \delta) = \rho^2 \frac{\partial \mathcal{E}(\rho, \delta)}{\partial \rho}. \quad (\text{C.20})$$

Therefore, the incompressibility of asymmetric nuclear matter at saturation  $K_{\text{sat}}(\delta) \equiv K(\rho_{\text{sat}}(\delta), \delta)$  where  $P(\rho_{\text{sat}}(\delta), \delta) = 0$ , is given by

$$\begin{aligned} K_{\text{sat}}(\delta) &= 9\rho_{\text{sat}}(\delta) \left. \frac{\partial^2 \mathcal{E}(\rho, \delta)}{\partial \rho^2} \right|_{\rho=\rho_{\text{sat}}(\delta)} \\ &= K_0 + \left( K_{\text{sym}} - 6L_{\text{sym}} - \frac{J_0}{K_0} L_{\text{sym}} \right) \delta^2 \\ &\quad + \left( K_{\text{sym},4} - 6L_{\text{sym},4} - \frac{J_0 L_{\text{sym},4}}{K_0} \right. \\ &\quad + \frac{9L_{\text{sym}}^2}{K_0} - \frac{J_{\text{sym}} L_{\text{sym}}}{K_0} + \frac{I_0 L_{\text{sym}}^2}{2K_0^2} \\ &\quad \left. + \frac{J_0 K_{\text{sym}} L_{\text{sym}}}{K_0^2} + \frac{3J_0 L_{\text{sym}}^2}{K_0^2} - \frac{J_0^2 L_{\text{sym}}^2}{2K_0^3} \right) \delta^4 + \mathcal{O}(\delta^6). \end{aligned} \quad (\text{C.22})$$

Figures C.1 and C.2 show several typical theoretical calculations for the EOS of asymmetric nuclear matter, namely, the non-relativistic SHF model using SIII, the RMF model using TM1, the non-relativistic BHF calculation using AV18 interaction with or without three-body force, and the relativistic DBHF calculation. It can be seen that the saturation point changes depending on the isospin asymmetry.

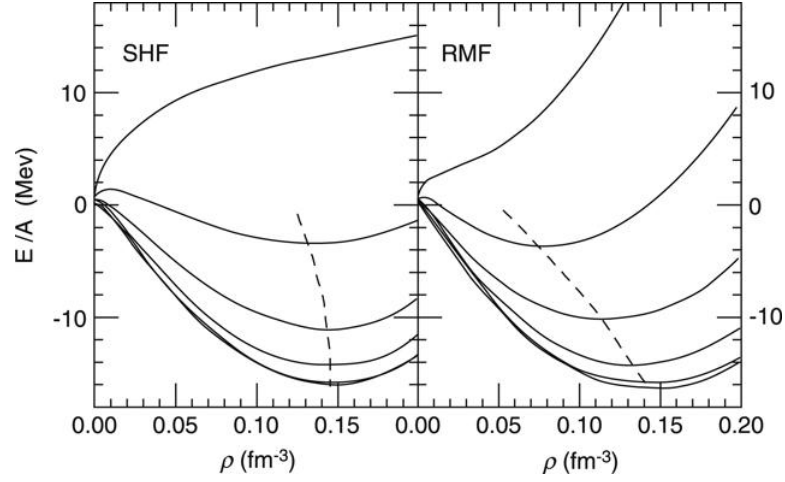


Figure C.1: The EOS of asymmetric nuclear matter from the Skyrme-Hartree-Fock (left panel) and relativistic mean-field (right panel) model calculations. The solid curves correspond to proton-to-neutron ratios of 0, 0.2, 0.4, 0.6, 0.8, and 1 (from top to bottom). Taken from [150].

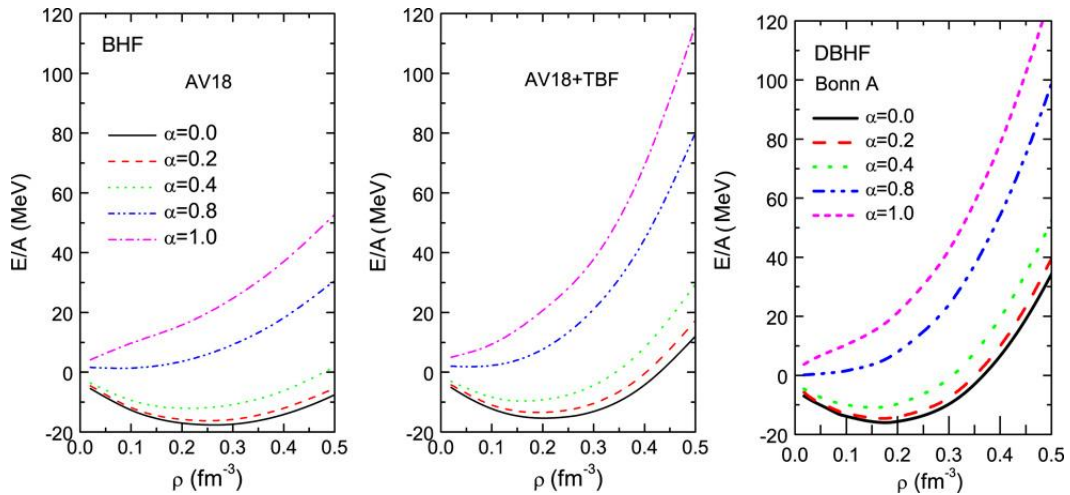


Figure C.2: Same as Fig. C.1 from non-relativistic Brueckner-Hartree-Fock calculations with or without three-body force (left and middle windows) and from the relativistic Dirac-Brueckner-Hartree-Fock calculations (right window). Taken from [150].



# REFERENCES

- [1] I. Tanihata, H. Hamagaki, O. Hashimoto, Y. Shida, N. Yoshikawa, K. Sugimoto, O. Yamakawa, T. Kobayashi, and N. Takahashi, *Phys. Rev. Lett.* **55**, 2676 (1985).
- [2] T. Ohnishi, T. Kubo, K. Kusaka, A. Yoshida, K. Yoshida, M. Ohtake, N. Fukuda, H. Takeda, D. Kameda, K. Tanaka, N. Inabe, Y. Yanagisawa, Y. Gono, H. Watanabe, H. Otsu, H. Baba, T. Ichihara, Y. Yamaguchi, M. Takechi, S. Nishimura, H. Ueno, A. Yoshimi, H. Sakurai, T. Motobayashi, T. Nakao, Y. Mizoi, M. Matsushita, K. Ieki, N. Kobayashi, K. Tanaka, Y. Kawada, N. Tanaka, S. Deguchi, Y. Satou, Y. Kondo, T. Nakamura, K. Yoshinaga, C. Ishii, H. Yoshii, Y. Miyashita, N. Uematsu, Y. Shiraki, T. Sumikama, J. Chiba, E. Ideguchi, A. Saito, T. Yamaguchi, I. Hachiuma, T. Suzuki, T. Moriguchi, A. Ozawa, T. Ohtsubo, M. A. Famiano, H. Geissel, A. S. Nettleton, O. B. Tarasov, D. P. Bazin, B. M. Sherrill, S. L. Manikonda, and J. A. Nolen, *Journal of the Physical Society of Japan* **79**, 073201 (2010).
- [3] I. Bombaci and U. Lombardo, *Phys. Rev. C* **44**, 1892 (1991).
- [4] M. Baldo and C. Maieron, *Journal of Physics G: Nuclear and Particle Physics* **34**, R243 (2007).
- [5] C. J. Horowitz and B. D. Serot, *Nuclear Physics A* **464**, 613 (1987).
- [6] R. Machleidt, K. Holinde, and C. Elster, *Physics Reports* **149**, 1 (1987).
- [7] R. Brockmann and R. Machleidt, *Phys. Rev. C* **42**, 1965 (1990).
- [8] F. Hofmann, C. M. Keil, and H. Lenske, *Phys. Rev. C* **64**, 034314 (2001).
- [9] J. Bartel, P. Quentin, M. Brack, C. Guet, and H. B. Hakansson, *Nuclear Physics A* **386**, 79 (1982).
- [10] J. Dobaczewski, H. Flocard, and J. Treiner, *Nuclear Physics A* **422**, 103 (1984).
- [11] E. Chabanat, P. Bonche, P. Haensel, J. Meyer, and R. Schaeffer, *Nuclear Physics A* **635**, 231 (1998).
- [12] B. Alex Brown, *Phys. Rev. C* **58**, 220 (1998).

- [13] A. N. Antonov, D. N. Kadrev, M. K. Gaidarov, E. M. d. Guerra, P. Sarriguren, J. M. Udias, V. K. Lukyanov, E. V. Zemlyanaya, and G. Z. Krumova, *Phys. Rev. C* **72**, 044307 (2005).
- [14] J. Stone and P.-G. Reinhard, *Progress in Particle and Nuclear Physics* **58**, 587 (2007).
- [15] M. Bender, P.-H. Heenen, and P.-G. Reinhard, *Rev. Mod. Phys.* **75**, 121 (2003).
- [16] H. Muller and B. D. Serot, *Nuclear Physics A* **606**, 508 (1996).
- [17] C. J. Horowitz and B. D. Serot, *Nuclear Physics A* **368**, 503 (1981).
- [18] Y. Sugahara and H. Toki, *Nuclear Physics A* **579**, 557 (1994).
- [19] G. A. Lalazissis, J. König, and P. Ring, *Phys. Rev. C* **55**, 540 (1997).
- [20] G. A. Lalazissis, S. Raman, and P. Ring, *Atomic Data and Nuclear Data Tables* **71**, 1 (1999).
- [21] T. Bürvenich, D. G. Madland, J. A. Maruhn, and P.-G. Reinhard, *Phys. Rev. C* **65**, 044308 (2002).
- [22] G. A. Lalazissis, T. Nikšić, D. Vretenar, and P. Ring, *Phys. Rev. C* **71**, 024312 (2005).
- [23] B. G. Todd-Rutel and J. Piekarewicz, *Phys. Rev. Lett.* **95**, 122501 (2005).
- [24] R. Kumar, B. K. Agrawal, and S. K. Dhiman, *Phys. Rev. C* **74**, 034323 (2006).
- [25] B. K. Agrawal, *Phys. Rev. C* **81**, 034323 (2010).
- [26] W.-Z. Jiang, B.-A. Li, and L.-W. Chen, *Phys. Rev. C* **76**, 054314 (2007).
- [27] D. Vretenar, A. Afanasjev, G. Lalazissis, and P. Ring, *Physics Reports* **409**, 101 (2005).
- [28] P. Danielewicz, R. Lacey, and W. G. Lynch, *Science* **298**, 1592 (2002).
- [29] A. Steiner, M. Prakash, J. Lattimer, and P. Ellis, *Physics Reports* **411**, 325 (2005).
- [30] J. M. Lattimer and M. Prakash, *Science* **304**, 536 (2004).
- [31] J. M. Lattimer and M. Prakash, *Physics Reports* **442**, 109 (2007), the Hans Bethe Centennial Volume 1906-2006.
- [32] J. Xu, L.-W. Chen, B.-A. Li, and H.-R. Ma, *Phys. Rev. C* **79**, 035802 (2009).
- [33] X. Roca-Maza and J. Piekarewicz, *Phys. Rev. C* **78**, 025807 (2008).
- [34] C. Fuchs, *Journal of Physics G: Nuclear and Particle Physics* **35**, 014049 (2008).

- [35] C.-H. Lee, T. T. S. Kuo, G. Q. Li, and G. E. Brown, *Phys. Rev. C* **57**, 3488 (1998).
- [36] M. Itoh, H. Sakaguchi, M. Uchida, T. Ishikawa, T. Kawabata, T. Murakami, H. Takeda, T. Taki, S. Terashima, N. Tsukahara, Y. Yasuda, M. Yosoi, U. Garg, M. Hedden, B. Kharraja, M. Koss, B. K. Nayak, S. Zhu, H. Fujimura, M. Fujiwara, K. Hara, H. P. Yoshida, H. Akimune, M. N. Harakeh, and M. Volkerts, *Phys. Rev. C* **68**, 064602 (2003).
- [37] M. Uchida, H. Sakaguchi, M. Itoh, M. Yosoi, T. Kawabata, Y. Yasuda, H. Takeda, T. Murakami, S. Terashima, S. Kishi, U. Garg, P. Boutachkov, M. Hedden, B. Kharraja, M. Koss, B. K. Nayak, S. Zhu, M. Fujiwara, H. Fujimura, H. P. Yoshida, K. Hara, H. Akimune, and M. N. Harakeh, *Phys. Rev. C* **69**, 051301 (2004).
- [38] J. Piekarewicz, *Phys. Rev. C* **76**, 031301 (2007).
- [39] U. Garg, T. Li, S. Okumura, H. Akimune, M. Fujiwara, M. Harakeh, H. Hashimoto, M. Itoh, Y. Iwao, T. Kawabata, K. Kawase, Y. Liu, R. Marks, T. Murakami, K. Nakanishi, B. Nayak, P. M. Rao, H. Sakaguchi, Y. Terashima, M. Uchida, Y. Yasuda, M. Yosoi, and J. Zenihiro, *Nuclear Physics A* **788**, 36 (2007), proceedings of the 2nd International Conference on Collective Motion in Nuclei under Extreme Conditions - COMEX 2.
- [40] T. Li, U. Garg, Y. Liu, R. Marks, B. K. Nayak, P. V. Madhusudhana Rao, M. Fujiwara, H. Hashimoto, K. Nakanishi, S. Okumura, M. Yosoi, M. Ichikawa, M. Itoh, R. Matsuo, T. Terazono, M. Uchida, Y. Iwao, T. Kawabata, T. Murakami, H. Sakaguchi, S. Terashima, Y. Yasuda, J. Zenihiro, H. Akimune, K. Kawase, and M. N. Harakeh, *Phys. Rev. C* **81**, 034309 (2010).
- [41] W. D. Myers, *Atomic Data and Nuclear Data Tables* **17**, 411 (1976).
- [42] P. Moller, W. D. Myers, W. J. Swiatecki, and J. Treiner, *Atomic Data and Nuclear Data Tables* **39**, 225 (1988).
- [43] P. E. Haustein, *Atomic Data and Nuclear Data Tables* **39**, 185 (1988).
- [44] B. Alex Brown, *Phys. Rev. Lett.* **85**, 5296 (2000).
- [45] R. J. Furnstahl, *Nuclear Physics A* **706**, 85 (2002).
- [46] S. Yoshida and H. Sagawa, *Phys. Rev. C* **73**, 044320 (2006).
- [47] M. Centelles, X. Roca-Maza, X. Viñas, and M. Warda, *Phys. Rev. Lett.* **102**, 122502 (2009).
- [48] M. Warda, X. Viñas, X. Roca-Maza, and M. Centelles, *Phys. Rev. C* **80**, 024316 (2009).
- [49] L.-W. Chen, C. M. Ko, B.-A. Li, and J. Xu, *Phys. Rev. C* **82**, 024321 (2010).

- [50] M. Centelles, X. Roca-Maza, X. Viñas, and M. Warda, *Phys. Rev. C* **82**, 054314 (2010).
- [51] L.-W. Chen, C. M. Ko, and B.-A. Li, *Phys. Rev. C* **72**, 064309 (2005).
- [52] C. J. Horowitz and J. Piekarewicz, *Phys. Rev. Lett.* **86**, 5647 (2001).
- [53] C. J. Horowitz and J. Piekarewicz, *Phys. Rev. C* **66**, 055803 (2002).
- [54] H. D. Vries, C. W. D. Jager, and C. D. Vries, *Atomic Data and Nuclear Data Tables* **36**, 495 (1987).
- [55] G. Fricke, C. Bernhardt, K. Heilig, L. A. Schaller, L. Schellenberg, E. B. Shera, and C. W. DeJager, *Atomic Data and Nuclear Data Tables* **60**, 177 (1995).
- [56] I. Angeli, *Atomic Data and Nuclear Data Tables* **87**, 185 (2004).
- [57] R. R. Johnson, T. Masterson, B. Bassalleck, W. Gyles, T. Marks, K. L. Erdman, A. W. Thomas, D. R. Gill, E. Rost, J. J. Kraushaar, J. Alster, C. Sabev, J. Arvieux, and M. Krell, *Phys. Rev. Lett.* **43**, 844 (1979).
- [58] G. W. Hoffmann, L. Ray, M. Barlett, J. McGill, G. S. Adams, G. J. Igo, F. Irom, A. T. M. Wang, C. A. Whitten, R. L. Boudrie, J. F. Amann, C. Glashauser, N. M. Hintz, G. S. Kyle, and G. S. Blanpied, *Phys. Rev. C* **21**, 1488 (1980).
- [59] H. J. Gils, H. Rebel, and E. Friedman, *Phys. Rev. C* **29**, 1295 (1984).
- [60] B. M. Barnett, W. Gyles, R. R. Johnson, R. Tacik, K. L. Erdman, H. W. Roser, D. R. Gill, E. W. Blackmore, S. Martin, C. A. Wiedner, R. J. Sobie, T. E. Drake, and J. Alster, *Physics Letters B* **156**, 172 (1985).
- [61] A. Krasznahorkay, A. Balanda, J. A. Bordewijk, S. Brandenburg, M. N. Harakeh, N. Kalantar-Nayestanaki, B. M. Nyak, J. Timr, and A. van der Woude, *Nuclear Physics A* **567**, 521 (1994).
- [62] V. E. Starodubsky and N. M. Hintz, *Phys. Rev. C* **49**, 2118 (1994).
- [63] S. Karataglidis, K. Amos, B. A. Brown, and P. K. Deb, *Phys. Rev. C* **65**, 044306 (2002).
- [64] B. C. Clark, L. J. Kerr, and S. Hama, *Phys. Rev. C* **67**, 054605 (2003).
- [65] A. Krasznahorkay, H. Akimune, A. van den Berg, N. Blasi, S. Brandenburg, M. Csatos, M. Fujiwara, J. Gulyas, M. Harakeh, M. Hunyadi, M. de Hoo, Z. Mate, D. Sohler, S. van der Werf, H. Wortche, and L. Zolnai, *Nuclear Physics A* **731**, 224 (2004).
- [66] A. Trzcińska, J. Jastrzębski, P. Lubiński, F. J. Hartmann, R. Schmidt, T. von Egidy, and B. Kłos, *Phys. Rev. Lett.* **87**, 082501 (2001).

- [67] B. Kłos, A. Trzcińska, J. Jastrzebski, T. Czosnyka, M. Kisieliński, P. Lubiński, P. Napiorowski, L. Pieńkowski, F. J. Hartmann, B. Ketzer, P. Ring, R. Schmidt, T. v. Egidy, R. Smolańczuk, S. Wycech, K. Gulda, W. Kurcewicz, E. Widmann, and B. A. Brown, *Phys. Rev. C* **76**, 014311 (2007).
- [68] A. Klimkiewicz, N. Paar, P. Adrich, M. Fallot, K. Boretzky, T. Aumann, D. Cortina-Gil, U. D. Pramanik, T. W. Elze, H. Emling, H. Geissel, M. Hellström, K. L. Jones, J. V. Kratz, R. Kulesa, C. Nociforo, R. Palit, H. Simon, G. Surówka, K. Sümmerer, D. Vretenar, and W. Waluś (LAND Collaboration), *Phys. Rev. C* **76**, 051603 (2007).
- [69] H. Sakaguchi, H. Takeda, S. Toyama, M. Itoh, A. Yamagoshi, A. Tamii, M. Yosoi, H. Akimune, I. Daito, T. Inomata, T. Noro, and Y. Hosono, *Phys. Rev. C* **57**, 1749 (1998).
- [70] S. Terashima, H. Sakaguchi, H. Takeda, T. Ishikawa, M. Itoh, T. Kawabata, T. Murakami, M. Uchida, Y. Yasuda, M. Yosoi, J. Zenihiro, H. P. Yoshida, T. Noro, T. Ishida, S. Asaji, and T. Yonemura, *Phys. Rev. C* **77**, 024317 (2008).
- [71] N. Fujita, H. Sakaguchi, Y. Maeda, A. Nonaka, H. Okamura, A. Tamii, J. Zenihiro, H. Matsubara, D. Ishikawa, S. Terashima, and Y. Yasuda, RCNP Annual Report, 2 (2008).
- [72] A. Carbone, G. Colò, A. Bracco, L.-G. Cao, P. F. Bortignon, F. Camera, and O. Wieland, *Phys. Rev. C* **81**, 041301 (2010).
- [73] B. A. Brown, G. Shen, G. C. Hillhouse, J. Meng, and A. Trzcińska, *Phys. Rev. C* **76**, 034305 (2007).
- [74] T. W. Donnelly, J. Dubach, and I. Sick, *Nuclear Physics A* **503**, 589 (1989).
- [75] C. J. Horowitz, S. J. Pollock, P. A. Souder, and R. Michaels, *Phys. Rev. C* **63**, 025501 (2001).
- [76] C. Xu, B.-A. Li, and L.-W. Chen, *Phys. Rev. C* **82**, 054607 (2010).
- [77] J. Zenihiro, H. Sakaguchi, T. Murakami, M. Yosoi, Y. Yasuda, S. Terashima, Y. Iwao, H. Takeda, M. Itoh, H. P. Yoshida, and M. Uchida, *Phys. Rev. C* **82**, 044611 (2010).
- [78] M. Fujiwara, H. Akimune, I. Daito, H. Fujimura, Y. Fujita, K. Hatanaka, H. Ikegami, I. Katayama, K. Nagayama, N. Matsuoka, S. Morinobu, T. Noro, M. Yoshimura, H. Sakaguchi, Y. Sakemi, A. Tamii, and M. Yosoi, *Nucl. Inst. & Meth. in Phys. Res. A* **422**, 484 (1999).
- [79] T. Noro, M. Fujiwara, O. Kamigaito, S. Hirata, Y. Fujita, A. Yamagoshi, T. Takahashi, H. Akimune, Y. Sakemi, M. Yosoi, H. Sakaguchi, and J. Tanaka, RCNP Annual Report, 177 (1991).

- [80] K. Hatanaka, K. Takahisa, H. Tamura, M. Sato, and I. Miura, *Nucl. Inst. & Meth. in Phys. Res.* **A384**, 575 (1997).
- [81] H. P. Yoshida, T. Baba, T. Noro, M. Kawabata, H. Akimune, H. Sakaguchi, A. Tamii, H. Takeda, and T. Kawabata, *RCNP Annual Report*, 164 (1996).
- [82] A. Tamii, H. Sakaguchi, H. Takeda, M. Yosoi, H. Akimune, M. Fujiwara, H. Ogata, M. Tanaka, and H. Togawa, *IEEE Trans. Nucl. Sci.* **43**, 2488 (1996).
- [83] A. Tamii, M. Itoh, T. Kawabata, H. Sakaguchi, H. Takeda, T. Taki, H. Torii, M. Yosoi, H. Akimune, T. Baba, M. Fujiwara, M. Kawabat, T. Noro, and H. Yoshida, in *Proceedings of the 2nd International Data Acquisition Workshop on Networked Data Acquisition System, Osaka, Japan, 1996*, edited by M. Nomachi and S. Ajimura (World Scientific, Singapore, 1997) p. 238.
- [84] T. Kawabata, H. Sakaguchi, A. Tamii, H. Takeda, T. Taki, and H. Yoshida, *RCNP Annual Report*, 161 (1996).
- [85] M. Ieiri, H. Sakaguchi, M. Nakamura, H. Sakamoto, H. Ogawa, M. Yosol, T. Ichihara, N. Isshiki, Y. Takeuchi, H. Togawa, T. Tsutsumi, S. Hirata, T. Nakano, S. Kobayashi, T. Noro, and H. Ikegami, *Nuclear Instruments and Methods in Physics Research Section A: Accelerators, Spectrometers, Detectors and Associated Equipment* **257**, 253 (1987).
- [86] S. Kato, K. Okada, M. Kondo, A. Shimizu, K. Hosono, T. Saito, N. Matsuoka, S. Nagamachi, K. Nisimura, N. Tamura, K. Imai, K. Egawa, M. Nakamura, T. Noro, H. Shimizu, K. Ogino, and Y. Kadota, *Nuclear Instruments and Methods* **169**, 589 (1980).
- [87] H. Takeda, *Memoirs of the Faculty of Science, Kyoto University, Series of Physics, Astrophysics, Geophysics and Chemistry* **44**, 1 (2003).
- [88] C. J. Horowitz, *Phys. Rev. C* **31**, 1340 (1985).
- [89] D. P. Murdock and C. J. Horowitz, *Phys. Rev. C* **35**, 1442 (1987).
- [90] C. J. Horowitz, D. P. Murdock, and B. D. Serot, “Computational nuclear physics 1,” (Springer-Verlag, Berlin, 1991) pp. 129–151.
- [91] E. D. Cooper, S. Hama, and B. C. Clark, *Phys. Rev. C* **80**, 034605 (2009).
- [92] I. Sick, *Nuclear Physics A* **218**, 509 (1974).
- [93] B. Frois, J. B. Bellicard, J. M. Cavedon, M. Huet, P. Leconte, P. Ludeau, A. Nakada, P. Z. Hô, and I. Sick, *Phys. Rev. Lett.* **38**, 152 (1977).

- [94] J. L. Friar and J. W. Negele, *Theoretical and experimental determination of nuclear charge distributions*, edited by M. Baranger and E. Vogt, *Advances in Nuclear Physics*, Vol. 8 (Plenum Press, New York, 1975) pp. 219–376, ISBN 0-306-41997-1.
- [95] W. Bertozzi, J. Friar, J. Heisenberg, and J. W. Negele, *Physics Letters B* **41**, 408 (1972).
- [96] J. Friar and J. Negele, *Nuclear Physics A* **212**, 93 (1973).
- [97] I. Sick, *Physics Letters B* **576**, 62 (2003).
- [98] P. G. Blunden and I. Sick, *Phys. Rev. C* **72**, 057601 (2005).
- [99] J. Arrington and I. Sick, *Phys. Rev. C* **76**, 035201 (2007).
- [100] P. J. Mohr, B. N. Taylor, and D. B. Newell, *Rev. Mod. Phys.* **80**, 633 (2008).
- [101] J. J. Kelly, *Phys. Rev. C* **70**, 068202 (2004).
- [102] K. Melnikov and T. van Ritbergen, *Phys. Rev. Lett.* **84**, 1673 (2000).
- [103] G. Simon, C. Schmitt, F. Borkowski, and V. Walther, *Nuclear Physics A* **333**, 381 (1980).
- [104] R. Rosenfelder, *Physics Letters B* **479**, 381 (2000).
- [105] J. J. Kelly, *Phys. Rev. C* **66**, 065203 (2002).
- [106] J. L. Friar, J. Martorell, and D. W. L. Sprung, *Phys. Rev. A* **56**, 4579 (1997).
- [107] R. Pohl, A. Antognini, F. Nez, F. D. Amaro, F. Biraben, J. M. R. Cardoso, D. S. Covita, A. Dax, S. Dhawan, L. M. P. Fernandes, A. Giesen, T. Graf, T. W. Hensch, P. Indelicato, L. Julien, C.-Y. Kao, P. Knowles, E.-O. Le Bigot, Y.-W. Liu, J. A. M. Lopes, L. Ludhova, C. M. B. Monteiro, F. Mulhauser, T. Nebel, P. Rabinowitz, J. M. F. dos Santos, L. A. Schaller, K. Schuhmann, C. Schwob, D. Taqqu, J. F. C. A. Veloso, and F. Kottmann, *Nature* **466**, 213 (2010).
- [108] B. D. Serot and J. D. Walecka, *The relativistic nuclear many-body problem*, edited by J. W. Negele and E. Vogt, *Advances in Nuclear Physics*, Vol. 16 (Plenum Press, New York, 1986) pp. 1–327, ISBN 0-306-41997-1.
- [109] C. J. Horowitz and B. D. Serot, *Physics Letters B* **140**, 181 (1984).
- [110] A. Haga, S. Tamenaga, H. Toki, and Y. Horikawa, *Phys. Rev. C* **70**, 064322 (2004).
- [111] S. Shim, B. C. Clark, S. Hama, E. D. Cooper, R. L. Mercer, L. Ray, and G. W. Hoffmann, *Phys. Rev. C* **38**, 1968 (1988).
- [112] T. Hatsuda and S. H. Lee, *Phys. Rev. C* **46**, R34 (1992).

- [113] T. Nagata, A. Kato, and T. Kohmura, *Nuclear Physics A* **601**, 333 (1996).
- [114] W. Long, J. Meng, N. V. Giai, and S.-G. Zhou, *Phys. Rev. C* **69**, 034319 (2004).
- [115] P. R. Bevington and D. K. Robinson, *Data Reduction and Error Analysis for the Physical Sciences*, 3rd ed. (McGraw-Hill, New York, 2003) ISBN 0-07-247227-8.
- [116] N. Tajima, S. Takahara, and N. Onishi, *Nuclear Physics A* **603**, 23 (1996).
- [117] T. Nikšić, D. Vretenar, and P. Ring, *Phys. Rev. C* **78**, 034318 (2008).
- [118] F. Chappert, M. Girod, and S. Hilaire, *Physics Letters B* **668**, 420 (2008).
- [119] P. G. Reinhard and H. Flocard, *Nuclear Physics A* **584**, 467 (1995).
- [120] B. K. Agrawal, S. K. Dhiman, and R. Kumar, *Phys. Rev. C* **73**, 034319 (2006).
- [121] S. Goriely and J. M. Pearson, *Phys. Rev. C* **77**, 031301 (2008).
- [122] S. Goriely, N. Chamel, and J. M. Pearson, *Phys. Rev. Lett.* **102**, 152503 (2009).
- [123] S. Goriely, N. Chamel, and J. M. Pearson, *Phys. Rev. C* **82**, 035804 (2010).
- [124] J. D. Walecka, *Annals of Physics* **83**, 491 (1974).
- [125] S.-J. Lee, J. Fink, A. B. Balantekin, M. R. Strayer, A. S. Umar, P. G. Reinhard, J. A. Maruhn, and W. Greiner, *Phys. Rev. Lett.* **57**, 2916 (1986).
- [126] M. M. Sharma, M. A. Nagarajan, and P. Ring, *Physics Letters B* **312**, 377 (1993).
- [127] R. J. Furnstahl, B. D. Serot, and H.-B. Tang, *Nuclear Physics A* **615**, 441 (1997).
- [128] F. J. Fattoyev, C. J. Horowitz, J. Piekarewicz, and G. Shen, *Phys. Rev. C* **82**, 055803 (2010).
- [129] T. Nikšić, D. Vretenar, P. Finelli, and P. Ring, *Phys. Rev. C* **66**, 024306 (2002).
- [130] B. A. Nikolaus, T. Hoch, and D. G. Madland, *Phys. Rev. C* **46**, 1757 (1992).
- [131] P. W. Zhao, Z. P. Li, J. M. Yao, and J. Meng, *Phys. Rev. C* **82**, 054319 (2010).
- [132] P. Finelli, N. Kaiser, D. Vretenar, and W. Weise, *Nuclear Physics A* **770**, 1 (2006).
- [133] K. Saito, K. Tsushima, and A. W. Thomas, *Phys. Rev. C* **55**, 2637 (1997).
- [134] M. B. Tsang, T. X. Liu, L. Shi, P. Danielewicz, C. K. Gelbke, X. D. Liu, W. G. Lynch, W. P. Tan, G. Verde, A. Wagner, H. S. Xu, W. A. Friedman, L. Beaulieu, B. Davin, R. T. de Souza, Y. Larochelle, T. Lefort, R. Yanez, V. E. Viola, R. J. Charity, and L. G. Sobotka, *Phys. Rev. Lett.* **92**, 062701 (2004).

- 
- [135] G. Colò, N. Van Giai, J. Meyer, K. Bennaceur, and P. Bonche, *Phys. Rev. C* **70**, 024307 (2004).
- [136] B. K. Agrawal, S. Shlomo, and V. Kim Au, *Phys. Rev. C* **68**, 031304 (2003).
- [137] M. Bender, K. Rutz, P.-G. Reinhard, J. A. Maruhn, and W. Greiner, *Phys. Rev. C* **60**, 034304 (1999).
- [138] L.-W. Chen, B.-J. Cai, C. M. Ko, B.-A. Li, C. Shen, and J. Xu, *Phys. Rev. C* **80**, 014322 (2009).
- [139] J. Piekarewicz and M. Centelles, *Phys. Rev. C* **79**, 054311 (2009).
- [140] H. Sagawa, S. Yoshida, G.-M. Zeng, J.-Z. Gu, and X.-Z. Zhang, *Phys. Rev. C* **76**, 034327 (2007).
- [141] J. P. Blaizot, *Physics Reports* **64**, 171 (1980).
- [142] J. M. Pearson, N. Chamel, and S. Goriely, *Phys. Rev. C* **82**, 037301 (2010).
- [143] J. A. McNeil, L. Ray, and S. J. Wallace, *Phys. Rev. C* **27**, 2123 (1983).
- [144] H. A. Bethe and R. F. Bacher, *Rev. Mod. Phys.* **8**, 82 (1936).
- [145] C. F. V. Weizsacker, *Z. Phys.* **96**, 431 (1935).
- [146] W. D. Myers and W. J. Swiatecki, *Annals. Phys.* **55**, 395 (1969).
- [147] W. D. Myers and W. J. Swiatecki, *Annals. Phys.* **84**, 186 (1974).
- [148] W. D. Myers and W. J. Swiatecki, *Nuclear Physics A* **336**, 267 (1980).
- [149] K. A. Brueckner, S. A. Coon, and J. Dabrowski, *Phys. Rev.* **168**, 1184 (1968).
- [150] B.-A. Li, L.-W. Chen, and C. M. Ko, *Physics Reports* **464**, 113 (2008).



# List of Tables

1.1	The previous results of $r_n$ , $r_p$ and $\Delta r_{np}$ for $^{208}\text{Pb}$ deduced from several experiments using various hadronic probes (all in fm). Except for X-ray cascade from $\bar{p}$ -atom (2), the errors are experimental only. . . . .	9
2.1	Target thicknesses and enrichments of Ni, and lead isotopes. . . . .	17
2.2	Design specifications of the GR spectrometer . . . . .	18
2.3	Specifications of the VDCs. . . . .	20
3.1	The relative ratio $R = R_{\text{Wall}}/R_{\text{SC}}$ of the beam collection efficiencies of SCFC and WallFC . . . . .	29
4.1	Best-fit medium-effect parameters $a_j$ and $b_j$ ( $j = \sigma, \omega$ ) in Eq. (4.4), (4.5). . .	47
4.2	Best-fit SOG parameters of the neutron density distributions for $^{204,206,208}\text{Pb}$ . The width $\gamma$ ( $= 1.70/\sqrt{3/2}$ ) and position $R_i$ of the $i$ th Gaussian in Eq. (4.7) are fixed to the values of the charge distribution [54]. The number in the parentheses are the $\chi^2_{\text{min}}$ over the degrees of freedom $\nu$ for each isotope. . . .	60
4.3	Fitted SOG parameters $Q_i$ of the upper and lower error-envelopes of the neutron density distribution for each lead isotope determined by Eq. (4.11). $\gamma$ , $N$ , and $R_i$ are the same as in Table 4.2, but the normalization condition is not satisfied in the case of the envelopes ( $\sum Q_i \neq 1$ ). . . . .	61
5.1	Root-mean-square radii of the charge $r_{ch}$ , proton $r_p^{\text{unfold}}$ , and neutron $r_n$ used in this work. The two types of errors for $r_n$ , namely, $\delta r_n^{\text{mdl}}$ determined by Eq. (4.11) and $\delta r_n^{\text{std}}$ by Eq. (4.8), are listed (all in fm). . . . .	63
5.2	Obtained values of $r_n$ , $r_p$ and $\Delta r_{np}$ for $^{208}\text{Pb}$ compared with the previous results deduced from several experiments using various hadronic probes (all in fm). Except for this work and X-ray cascade from $\bar{p}$ -atom (2), the errors are experimental only. The errors of this work stand for the total errors including the model uncertainties $\delta r_n^{\text{mdl}}$ determined by Eq. (4.11). . . . .	64
5.3	Neutron skin thickness for $^{208}\text{Pb}$ and the nuclear matter properties at saturation density, such as the incompressibility coefficient $K_0$ , the symmetry energy $S(\rho_{\text{sat}})$ , its slope $L$ , and the curvature $K_{\text{sym}}$ in various relativistic and non-relativistic theoretical models. . . . .	68

A.1	Differential cross sections and analyzing powers for $^{58}\text{Ni}(p, p)$ at $E_p = 295$ MeV.	83
A.2	Differential cross sections and analyzing powers for $^{204}\text{Pb}(p, p)$ at $E_p = 295$ MeV.	85
A.3	Differential cross sections and analyzing powers for $^{206}\text{Pb}(p, p)$ at $E_p = 295$ MeV.	87
A.4	Differential cross sections and analyzing powers for $^{208}\text{Pb}(p, p)$ at $E_p = 295$ MeV.	89
B.1	Dirac matrix types . . . . .	93

# List of Figures

1.1	Rendition of the assumed structure and phases of a neutron star. Taken from Ref. [33]. . . . .	2
1.2	Neutron star mass versus central density obtained from various types of the EOSs by relativistic hadronic field models, taken from Ref. [34] . . . . .	2
1.3	The EOS of symmetric nuclear matter and pure neutron matter calculated by the non-relativistic Brueckner-Hartree-Fock and variational approaches using AV18 interaction with three body force (dotted red), the Dirac-Brueckner-Hartree-Fock using Bonn A (solid red), chiral perturbation theory (dashed black), and several phenomenological mean field models (blue) taken from Ref. [34]. . . . .	3
1.4	Neutron skin thickness for $^{208}\text{Pb}$ as a function of (a) $L$ , (b) $K_{\text{sym}}$ , and (c) $E_{\text{sym}}(\rho_0) = \mathcal{S}(\rho_{\text{sat}})$ for 21 sets of Skyrme parameterizations. Taken from Ref. [51].	5
1.5	Correlation between neutron skin for $^{208}\text{Pb}$ and the symmetry energy $a_4 = \mathcal{S}(\rho_{\text{sat}})$ at saturation. Take from Ref. [45]. . . . .	5
1.6	Correlation between neutron skin for $^{208}\text{Pb}$ and the slope of the symmetry energy $p_0 = \rho_{\text{sat}}L/3$ . Take from Ref. [45]. . . . .	5
1.7	Neutron density distributions of $^{116,118,120,122,124}\text{Sn}$ in the model-independent form of SOG function extracted from polarized proton elastic scattering at $E_p = 295$ MeV [70]. . . . .	7
1.8	Constraint regions on the $\mathcal{S}(\rho_{\text{sat}})$ - $L$ plane by several recent analyses. Taken from Ref. [76]. . . . .	11
1.9	Constraint regions on the $L$ by several recent analyses. Taken from Ref. [72].	11
2.1	Overview of the RCNP ring cyclotron facility with the WS beam line. AVF and Ring cyclotron operate in a coupled mode and provide polarized proton beam at $E_p = 295$ MeV to the WS beam line in west experimental hall. . . .	14
2.2	Schematic view of WS beam line . . . . .	15
2.3	Setup of the BLP (top view) . . . . .	16
2.4	Schematic view of the magnetic spectrometer, “Grand Raiden” . . . . .	19
2.5	Structure of a X plane of the VDCs. . . . .	21
2.6	Wire configurations of the VDCs. The wire numbering orders are shown by the arrows . . . . .	22

2.7	Wire configurations of the VDCs. The wire numbering orders are shown by the arrows . . . . .	23
2.8	Schematic view of the data acquisition system . . . . .	24
3.1	Three types of beam polarization (a, b, c) and instrumental asymmetry (d) for each run. Red and blue circles mean $ p^{\uparrow(\downarrow)} $ (spin-up and -down mode). Beam polarizations (a) assuming asymmetry $\beta_{LR} = 1$ , (b) using each $\beta_{LR}$ , and (c) using the averaged $\beta_{LR}$ fitted by a Gaussian as shown in Fig. 3.2 are compared with each other. In this data reduction the type of (c) was used. . . . .	26
3.2	The projection of the instrumental asymmetries $\beta_{LR}$ in Fig. 3.1(d) was fitted with a Gaussian. . . . .	27
3.3	The spectrum of the geometrical mean $\bar{P}$ of PS1. proton and deuteron peaks are identified. . . . .	29
3.4	Colors plot of $\bar{P}$ of PS1 versus the position spectrum at the focal plane. It is found that $\bar{P}$ is independent of the focal plane position. . . . .	30
3.5	TOF spectrum between the trigger and the downscaled RF. . . . .	31
3.6	Colors plot of the X position at the focal plane versus TOF. Elastically scattered protons can be clearly identified as shown in the area surrounded by the solid circle. . . . .	32
3.7	Colors plot of $\bar{P}$ versus TOF of PS1 for PID. . . . .	32
3.8	(a) TDC spectrum on X1 plane obtained from LeCroy 3377. (b) Drift length (cm) converted from TDC spectrum (a) by using so-called $x-t$ relation. . . . .	33
3.9	$\theta$ versus X plot at the focal plane of the spectrometer reconstructed from the VDCs data in the case of $^{208}\text{Pb}$ at $\theta_{lab.} = 36.0^\circ$ . . . . .	34
3.10	Typical position spectra for proton elastic scattering from $^{204,206,208}\text{Pb}$ and $^{58}\text{Ni}$ at $\theta_{lab.} = 36.0^\circ$ . Elastic events (g. s. ( $0^+$ )) can be distinguished from other excited states in each spectrum. . . . .	35
4.1	Obtained data of differential cross sections and analyzing powers for elastic scattering from $^{58}\text{Ni}$ and $^{204,206,208}\text{Pb}$ at $E_p = 295$ MeV, whereas the lines are due to Murdock and Horowitz (solid) [89, 90] and the global Dirac optical potential (dashed) [91]. The dash-dotted lines show the MH model calculations for $^{58}\text{Ni}$ with the realistic nucleon density by an unfolding charge density. . . . .	42
4.2	Proton density distributions of $^{58}\text{Ni}$ and $^{204,206,208}\text{Pb}$ by unfolding charge distributions with the new parameter sets of nucleon charge form factor (solid lines). The blue dotted lines are due to the DH calculations for comparison, while the green long-dotted, short-dotted, dashed, and dash-dotted lines are due to Skyrme–Hartree–Fock–Bogolyubov calculations with SIII, SKM*, SKP, and SLY4 parametrizations, respectively. . . . .	45

4.3	The neutron skin thicknesses for even-Ni isotopes calculated by DBHF with the Groningen (triangles) and Bonn A (circles) interactions, and RMF with the NL3 [19] (crosses) parametrization. All of them shows that the neutron skin thickness of $^{58}\text{Ni}$ is almost zero. Taken from Ref. [8]. . . . .	48
4.4	The neutron skin thicknesses for even-Ni isotopes calculated by Hartree–Fock–Bogolyubov (HFB) plus pairing corrections using five types of Skyrme forces, that is, SIII [116] (filled circles), SkM* [9] (filled squares), SkP [10] (asterisks), Sly4 [11] (open circles), and SLy5 [11] (open squares) parameterizations. As is the case with relativistic models in Fig. 4.3 nonrelativistic models show that the neutron skin thickness of $^{58}\text{Ni}$ is almost zero. . . . .	48
4.5	Calibration of medium-effect parameters by fitting to the experimental data for $^{58}\text{Ni}$ . The solid line is the medium-modified RIA calculation with best-fit parameters. The dashed and dash-dotted lines are from the original MH model with DH and realistic nucleon densities. . . . .	49
4.6	Best fit results for neutron density distributions in $^{204,206,208}\text{Pb}$ , are shown as solid lines. The original MH and medium-modified RIA calculations with the DH nucleon density are also shown by dashed and dash-dotted lines. . . . .	51
4.7	Results of fitting to the experimental data and extracted neutron density of $^{208}\text{Pb}$ with its standard error-envelope (solid lines). The dashed and dash-dotted lines are medium-modified RIA calculations but using the DH nucleon densities and the 3pG neutron density by Ray [58] respectively. The dotted line in (c) is the realistic proton density. . . . .	53
4.8	Percent deviation between the experimental data and the medium-modified RIA calculations of differential cross section at each angle defined as Eq. (4.9). The marks are the same definitions as Fig. 4.7. The lines are just for the guide. . . . .	54
4.9	Results of fitting to the experimental data and extracted neutron density of $^{204}\text{Pb}$ with its standard error-envelope (solid lines). The dashed lines are medium-modified RIA calculations but using the DH nucleon densities. . . . .	55
4.10	Results of fitting to the experimental data and extracted neutron density of $^{206}\text{Pb}$ with its standard error-envelope (solid lines). The dashed lines are medium-modified RIA calculations but using the DH nucleon densities. . . . .	56
4.11	Extracted neutron densities for $^{204,206,208}\text{Pb}$ with two types of error-envelopes shown together with DH neutron densities (dotted lines) and point proton densities by unfolding charge densities (dash-dotted lines). The cross-hatched blue and hatched red error-envelopes were estimated by Eq. (4.11) and Eq. (4.8), respectively. . . . .	58
4.12	The radial distributions of neutron surface densities for $^{204,206,208}\text{Pb}$ ( $4\pi r^2 \rho(r) \text{ fm}^{-1}$ ) with two types of error-envelopes shown together with DH neutron surface densities (dotted lines) and proton surface densities by unfolding charge densities (dash-dotted lines). The cross-hatched blue and hatched red error-envelopes were the same as Fig. 4.11. . . . .	59

5.1	Systematic behavior of the neutron skin thicknesses for $^{204,206,208}\text{Pb}$ . The filled circles are the results of this work with the two types of error bars. The red and blue lines represent the errors due to the experimental only $\delta r_n^{\text{std}}$ and including the model uncertainties $\delta r_n^{\text{mdl}}$ , respectively. The filled squares, triangle, and inverted triangle are from the analysis of proton elastic scattering at 650 MeV [62], X-ray cascade from antiprotonic atoms [67], and PDR strengths from $^{129-132}\text{Sn}(\gamma, \gamma')$ [68], respectively, with their statistical errors only. The open triangles, crosses, squares and diamonds show the calculations of relativistic mean field models (pale blue marks) with NL3 [19], DD-ME2 [22], DD-PC1 [117], and FSUGold [23] parameterization while the open circles, squares, stars and asterisks are from non-relativistic mean field models (pink marks) with SkM* [9], SkP [10], Sly4 [11], and Skxs20 [73] parameterization. DD-ME2, FSUGold, and Skxs20 parameterizations have been recently developed and conform closely to all the extracted neutron skin thicknesses. . . . .	66
5.2	$\Delta r_{np}$ for $^{208}\text{Pb}$ (fm) vs $K_0$ (MeV). . . . .	70
5.3	$\Delta r_{np}$ for $^{208}\text{Pb}$ (fm) vs $K_{\text{sym}}$ (MeV). . . . .	70
5.4	$\Delta r_{np}$ for $^{208}\text{Pb}$ (fm) vs $\mathcal{S}(\rho_{\text{sat}})$ (MeV). . . . .	71
5.5	$\Delta r_{np}$ for $^{208}\text{Pb}$ (fm) vs the slope coefficient $L$ (MeV). . . . .	71
5.6	$L$ (MeV) vs $\mathcal{S}(\rho_{\text{sat}})$ (MeV). Surrounded areas are the extracted ranges of $\mathcal{S}(\rho_{\text{sat}})$ and $L$ from $\Delta r_{np}$ for $^{208}\text{Pb}$ as shown in Figs. 5.4 and 5.5 . . . . .	72
5.7	$\Delta r_{np}$ for $^{204}\text{Pb}$ (fm) vs $\mathcal{S}(\rho_{\text{sat}})$ (MeV). . . . .	73
5.8	$\Delta r_{np}$ for $^{204}\text{Pb}$ (fm) vs the slope coefficient $L$ (MeV). . . . .	73
5.9	$\Delta r_{np}$ for $^{206}\text{Pb}$ (fm) vs $\mathcal{S}(\rho_{\text{sat}})$ (MeV). . . . .	73
5.10	$\Delta r_{np}$ for $^{206}\text{Pb}$ (fm) vs the slope coefficient $L$ (MeV). . . . .	73
5.11	All the extracted regions of $L$ vs $\mathcal{S}(\rho_{\text{sat}})$ for $^{204,206,208}\text{Pb}$ correspond to the red lines in Figs. 5.4, 5.5, 5.7, 5.8 5.9, and 5.10 due to the experimental errors of the extracted $\Delta r_{np}$ only. Black filled circle and solid error bars are the weighted average of these three regions. . . . .	74
5.12	Similar to Fig. 5.11, but the extracted regions correspond to the blue lines in Figs. 5.4, 5.5, 5.7, 5.8 5.9, and 5.10 due to the total errors of the extracted $\Delta r_{np}$ including the model uncertainties. . . . .	75
5.13	Hatched area is the constraint region on the $K_\tau$ and $\Delta r_{np}$ for $^{208}\text{Pb}$ plane with several non-relativistic (triangles) and relativistic (circles) mean-field models. The constraint on $\Delta r_{np}$ is our extracted value (blue and red lines on the y-axis), whereas on $K_\tau$ is taken from Ref. [138]. . . . .	77
B.1	Meson exchange diagrams for the relativistic Love-Franey model. . . . .	92
C.1	The EOS of asymmetric nuclear matter from the Skyrme-Hartree-Fock (left panel) and relativistic mean-field (right panel) model calculations. The solid curves correspond to proton-to-neutron ratios of 0, 0.2, 0.4, 0.6, 0.8, and 1 (from top to bottom). Taken from [150]. . . . .	101

C.2 Same as Fig. C.1 from non-relativistic Brueckner-Hartree-Fock calculations with or without three-body force (left and middle windows) and from the relativistic Dirac-Brueckner-Hartree-Fock calculations (right window). Taken from [150]. . . . . 101